SURFACE CHEMISTRY OF HIERARCHICAL NANOSPRINGS FOR SENSING AND CATALYSIS

A Dissertation

Presented in Partial Fulfillment of the Requirements of the

Degree of Doctorate of Philosophy

with a

Major in Physics

in the

College of Graduate Studies

University of Idaho

by

Blaise-Alexis Fouetio Kengne

September 2014

Major Professor: David N McIlroy, Ph.D.

Authorization to Submit Dissertation

This dissertation of Blaise-Alexis Fouetio Kengne submitted for the degree of Doctorate of Philosophy with a major in Physics and titled "Surface Chemistry of Hierarchical Nanosprings for Sensing and Catalysis," has been reviewed in final form. Permission, as indicated by the signatures and dates given below, is now granted to submit final copies to the College of Graduate Studies for approval.

Major Professor: _____ Date: _____
David N McIlroy, Ph.D.

Committee Members: _____ Date: _____
Matthew Hedman, Ph.D.

_____ Date: _____
Leah Bergman, Ph.D.

_____ Date: _____
Eric Aston, Ph.D.

Department Administrator: _____ Date: _____
Jo Ellen Force, Ph.D.

College of Science Dean: _____ Date: _____
Paul Joyce, Ph.D.

Final Approval and Acceptance

Dean of the College of Graduate Studies: _____ Date: _____
Jie Chen, Ph.D.

Abstract

Silica nanosprings (NS) were grown and their surface chemistry was modified depending upon the application. For explosive detection, NS were subsequently coated with ZnO, decorated with metal nanoparticles, and functionalized with thiols; while NS supported cobalt catalysts (Co/NS) were prepared for Fischer-Tropsch synthesis (FTS). Scanning and transmission electron microscopies (SEM and TEM), X-ray diffraction (XRD), N_2 physisorption, hydrogen-temperature programmed reduction (H_2-TPR), and X-ray and ultraviolet photoelectron spectroscopies (XPS and UPS) have been used to characterize the hierarchical NS. Based on XPS analysis of the thiolated NS, a single S 2p core level doublet is observed for 4-mercaptobenzoic acid and 11-(1-pyrenyl)-1-undecathiol, which is assigned to S-Au bond. The S 2p core level of L-cysteine, 6-mercaptohexanol and DL-thioctic acid consists of two doublets, where one is S-Au bond and the other is the S-Zn bond. UPS analysis shows that the hybridization of the S 3p states and Au d-bands produces antibonding and bonding states, above and below the Au d-bands, which is characteristic of molecular chemisorption on Au nanoparticles. Gas sensors functionalized with 4-mercaptobenzoic acid and 6-mercaptohexanol showed the strongest responses to ammonium nitrate by factors of 4 and 5, respectively, relative to the less responsive thiols. The response can be correlated to the packing density and ordering of thiols. For FTS, even though Co/NS had 75 times less gravimetric Co content than the reference catalyst, without being fully reduced, it still showed higher activity. This is attributed to higher Co dispersion on NS and greater gases accessibility. *In situ* XPS has been used to monitor the reduction of Co/NS. The analysis shows that cobalt is present in the starting catalyst as Co_3O_4 spinel phase. At 385 ^{0}C and 10^{-6} Torr of H_2 a two-step reduction from Co_3O_4 to CoO and then to Co^0 is observed, which is

consistent with H_2-TPR results. The two reduction steps are concurrent. The reduction saturates at the value of 41% after 20 hours, which correlates with the drop observed in FTS activity. Heat is lost by convection and radiation along the NS. Conversely, Co/NS is fully reduced at 680 ºC and 10 Torr of H_2 after 10 hours.

Acknowledgments

I would like to express my sincere gratitude to my major professor Dr. David N McIlroy first for accepting me in his research group, then for his patience in training and guiding through challenging experimental research problems. I will hold on to his values and ideals as a skillful scientist throughout my career.

I would like to thank all the Physics Department faculties and staffs, especially Mr John Faila who is instrumental with all the machining, for any job to be successfully completed in our group. My warmest regards to Dr. Vladimir Dobrokhotov at Western Kentucky University, to Dr. Patrick J. Hrdlicka at the Department of Chemistry, to Dr. Armando G. McDonald at the Department of Forest, Rangeland & Fire Sciences, and their students for the frank and effective collaboration. I would like to thank all the members of our group, both present and past, thinking of Dr. Miles Beaux and Dr. Ishwar B. Niraula who trained me in photoemission experiments.

I'm mindful of my church family at the Moscow First Presbyterian Church for their constant and multiform support. I would like to sincerely thank my dear friend Dr. Jean Claude Chokomakoua who triggered my Doctorate's journey in the United States and has been both supportive and inspiring in bringing this endeavor to full fruition.

Finally, I would like to acknowledge the financial support of the Office of Navy Research (ONR), the National Institute for Advanced Transportation Technology (NIATT), and the College of Science's Dyess Faculty Fellowship.

Blaise-Alexis Fouetio Kengne

Dept. of Physics

Univ. of Idaho, Moscow ID, 83844-0903

Dedication

To my wife Adel Florence Makuete

and my children:

Tony Nginlabhe Fouetio,

Glory Lys Kengne Fouetio,

Chadrac Fouodo Fouetio, and

Otniel Leo Kuete Fouetio

Table of Contents

List of Figures

List of Tables

CHAPTER 1
Introduction

1.1 Nanomaterials and Detection of Explosives

A nanomaterial is any material with at least one characteristic dimension less than 100 nm. Nanotechnology research has been experiencing lots of interest and investment, the motivation being novel size dependent physical and chemical properties of nanomaterials. In fact, nanoscale effects significantly modify nanomaterials catalytic,[1] electrical,[2] magnetic,[3] mechanical,[4] optical,[5] and thermal properties, that can sometimes differ from those of their bulk form. Those differences are the consequences of changes in the surface chemistry which influence the surface energy, the functionality and the structural stability of nanomaterials.[6] For instance, their large surface area increases the surface energy, thereby increases the reactivity.[7]

Sensing, which is closely related to reactivity, has been one of the most successful applications of nanostructures. They are highly sensitive platforms for the detection of molecules adsorbed on their surfaces because the distances over which the interactions modify their local environment are comparable to their dimensions; their optical and electrical properties can be modulated by molecular adsorption as well.[8] Despite the progress achieved in the past decades in the detection of chemicals, acts of terror perpetrated with explosive materials after security breaches, continue to demonstrate the limitations of the existing detection techniques. Given the variety of chemicals and combinations that can be used as explosives, constant research efforts continue to be put into the development of highly sensitive and selective sensors for explosives. For this purpose, nanomaterials are promising sensor platforms.

The proposed sensing mechanisms for ZnO nanostructures are illustrated in Figure 1.1. In general, a gas sensor response corresponds to capture and release of electrons by molecular adsorption on the surface of the sensor, followed by desorption. In the case of ZnO, when exposed to air, oxygen molecules chemisorbed onto its surface and formed oxygen ions by capturing electron from the conduction band. Once ZnO is exposed to a reducing gas like toluene, the gas reacts with oxygen ions, releasing the electrons back to the conduction band, hence an increase in the conductivity. This process corresponds to the redox of ZnO. The decoration of ZnO with metal nanoparticles creates nano -Schottky contacts. Upon adsorption of oxygen onto the metal nanoparticles, a depletion layer is formed due to near-surface band bending (Fig. 1.1 b). The exposure to toluene reduces the band bending (depletion layer) as electrons are transferred to the conducting region, resulting in an increase in the conductance (Fig. 1.1 c). The Fermi level pinning during this process can be translated into the modulation of the Schottky barrier, $E_b = \Phi - \chi$, where E_b is the surface energy barrier, Φ is the work function, and χ is the electron affinity of ZnO. Another well-known mechanism invoked to explain the enhanced sensitivity by metal decoration is the spillover effect, where catalytic dissociation of the adsorbed molecules onto the metal nanoparticle surface followed by the diffusion of atomic species in the substrate increases the conductivity.

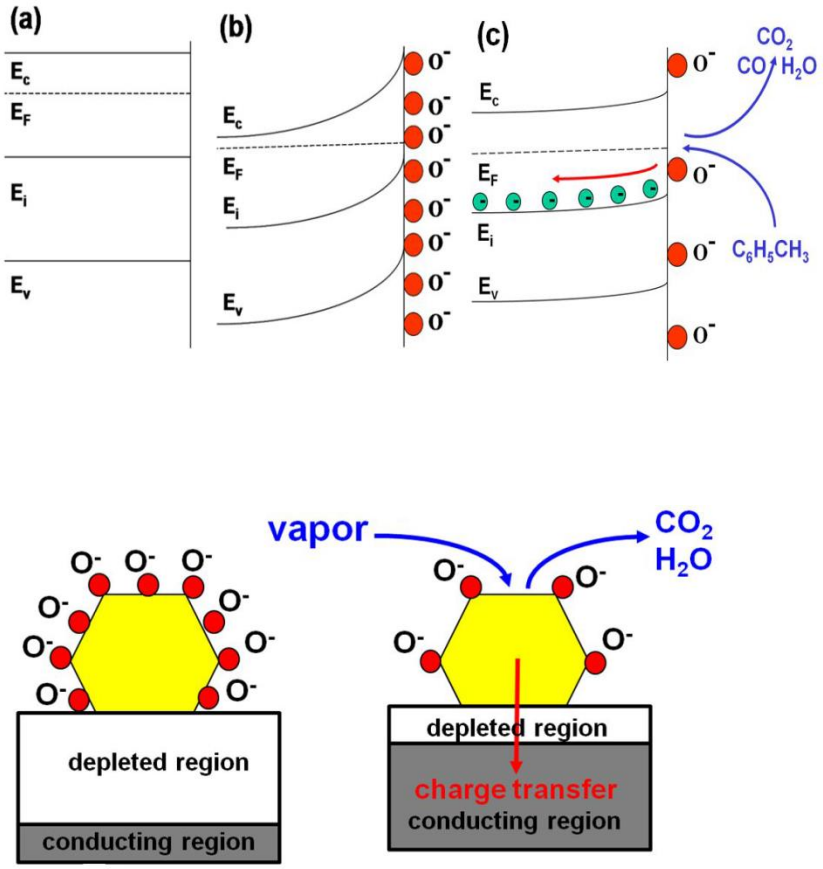

Figure 1.1 (Top) Modulation of nano-Schottky .barriers and (bottom) depletion model.[8]

For selective sensing, based on the successful realization of molecular switches for memory and logic devices,[9] molecular rectification of nanostructures has been used. Generally, molecules can be attached to the surfaces of semiconductors, metals, or metal oxides. Self-assembly is the ability of small, interacting components to aggregate into a global minimum structure through a statistical exploration of intermediate states.[10] Self-assembly allows patterning and functionalization of extended surfaces with long range ordered molecules. Thiol-based chemistry is one of the techniques used to achieve defect free, densely packed, self-assembled monolayers (SAMs) on metal oxides or semiconductors. In SAMs on atomically flat substrates, molecules are organized in periodically structured overlayers with a defined orientation towards the surface.[11] Different headgroups can be used to target

specific analytes. SAMs applications include chemical and biological sensing,[12-13] passivation layers,[14] opto-electronics and molecular electronics.[15]

1.2 Catalytic Production of Fuels

The world depends on transportation fuels, 96 % of which is produced from fossil fuels (petroleum and natural gas).[16] There are many economic and environmental issues related to the abundant use of fossil fuels as source of energy, such as the uneven distribution of oil and other natural resources, the depletion of the oil reserves, and the greenhouse gases emissions. To reduce the dependency from fossil fuels, there is a pressing need to increase the use of other sources of energy (nuclear, solar, wind, biomass). In the context of biomass for energy, biomass derived energy is referred to as green energy, where biomass implies plant based material. Biomass is biological material derived from living, or recently living, organisms (wood, energy crops, agricultural residues, food waste, industrial waste and co-products). So, biomass can equally apply to both animal and vegetable material. Biomass can be converted into energy and other chemicals in many ways, but thermochemical conversion is suitable for fuel production. Thermochemical conversion is a multi-step process, comprising syngas (synthetic gas) production and cleaning, and fuel synthesis. Syngas in its simplest form is a mixture of two molecules, carbon monoxide (CO) and hydrogen (H_2). Its composition (H_2:CO ratio) varies as a function of production technology and feedstock, 3:1 for steam methane reforming and closer to 1:1 for coal and biomass gasification.[17] Besides Methanol-to-Gasoline process, where methanol has to be produced from syngas first, Fischer-Tropsch synthesis (FTS) provides a direct method with which to convert syngas into liquid fuels. FTS is a heterogeneous catalytic process that includes the following reactions:

$CO + 3H_2 \rightarrow CH_4 + H_2O$ (Methanation) (1.1)

$nCO + (2n+1)\ H_2 \rightarrow C_nH_{2n+2} + nH_2O$ (Paraffins) (1.2)

$nCO + 2nH_2 \rightarrow C_nH_{2n} + nH_2O$ (Olefins) (1.3)

$nCO + 2nH_2 \rightarrow C_nH_{2n+1}OH + (n-1)\ H_2O$ (Alcohols) (1.4)

$CO + H_2O \rightarrow CO_2 + H_2$ (Water-Gas-Shift) (1.5)

$2CO \rightarrow C + CO_2$ (Boudouard Reaction) (1.6)

The reaction products range from methane to long chains paraffins and olefins, alcohols and some aromatics. The products distribution followed the statistical model of Anderson-Shulz-Flory (ASF) described by the following relationship:

$$W_n = n(1-\alpha)^2\alpha^{n-1} \quad (1.7)$$

, where W_n is the weight percent of hydrocarbons containing n carbon atoms and α is the chain growth probability, which is determined by the rates of chain growth (R_p) and chain termination (R_t), and is expressed by ($\alpha = R_p/(R_p + R_t)$).[18] Equation (1.7) is plotted in Fig. 1.2 and displayed the calculated distributions for several products.

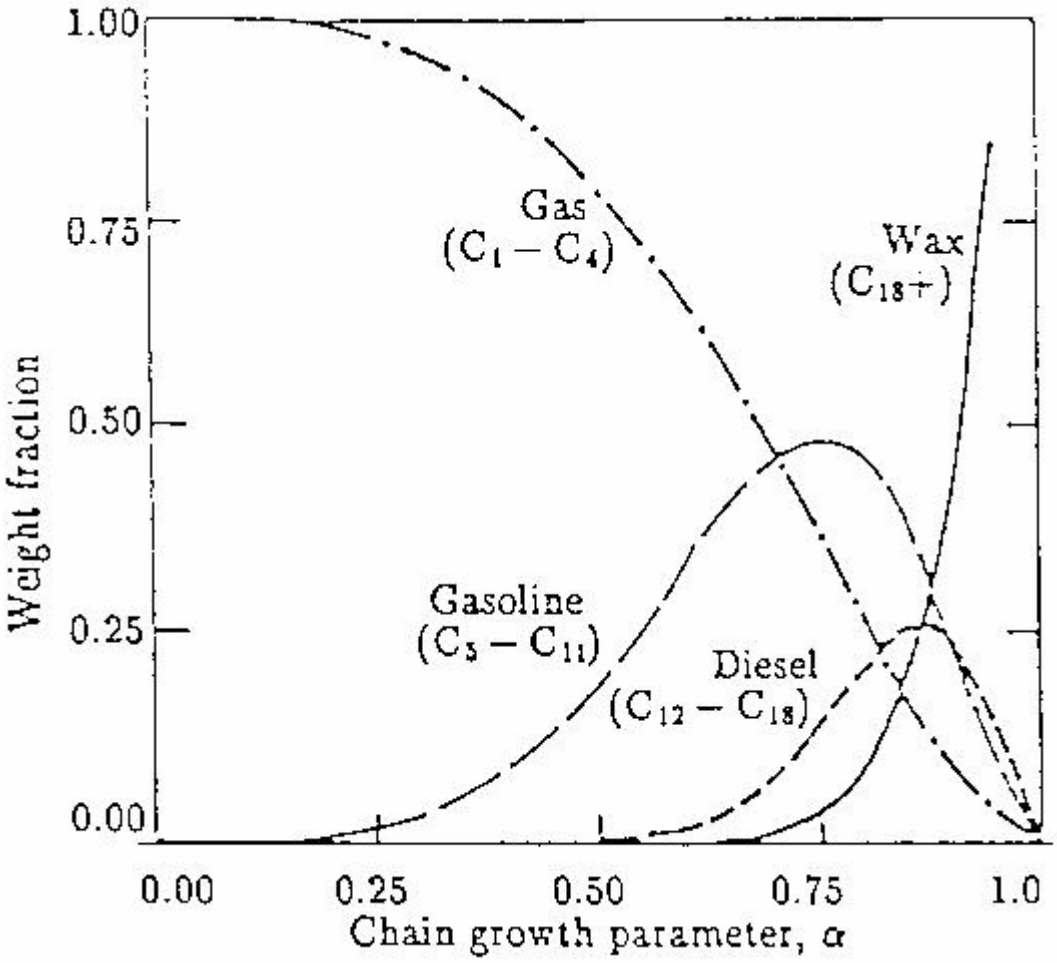

Figure 1.2 Production distribution in FTS as a function of chain growth probability (α).[19]

The selectivities to gasoline ($C_5 – C_{11}$) and Diesel ($C_{12} – C_{18}$) are limited to roughly 45 % and 30 %, respectively. There is a maximum yield for all products; high selectivities are only possible to light and heavy products. Variables that influence product distributions are temperature, pressure, gas composition and catalyst types.

Several metals (ruthenium (Ru), iron (Fe), cobalt (Co), nickel (Ni), iridium (Ir), platinum (Pt), and palladium (Pd)) are active catalysts for the FT process, but Fe and Co stand out as the most viable in an industrial scale. Fe is used for high-temperature FTS (300 – 350 ºC), while Co is preferred for low-temperature FTS (200 – 240 ºC). The Catalyst usually consists of metal nanoparticles dispersed onto an oxide support (SiO_2, TiO_2, Al_2O_3, and MgO).

The water-gas-shift (WSG) and the Boudouard reaction are FTS side reactions. High WGS activity is not desirable because the formation of CO_2 would result in low molecular weight hydrocarbons yield. On the other hand, the Boudouard reaction leads to carbon deposition on the catalyst surface, causing deactivation. Other causes of catalyst deactivation are poisoning, sintering, re-oxidation, and strong metal-support interaction.[20] The catalyst is poisoned by sulfur and nitrogen compounds, also by the presence of chlorine, alkali and alkaline earth metals in the reaction medium. Sintering of crystallites occur through atomic migration (Ostwald ripening or coarsening) and crystallite migration (coalescence), resulting in the reduction of active surface area. Water, which is the most abundant FTS byproduct, may cause surface oxidation of metal nanoparticles. A strong metal-support interaction leads to the formation of hardly reducible metal species.

1.3 Nanosprings: Catalyst Supports and Building Blocks for Sensor Platforms

Nanosprings (NS) are suitable catalyst supports and superior scaffoldings to build sensors owing to a number of morphological and structural parameters. NS coil coherently and have a large surface area in the range of 350 – 400 m^2/g, which is higher relative to their thin film and nanowire counterparts. $1cm^2$ of a flat substrate coated with 80 μm thick coating of NS has approximately 0.15 m^2 of surface area, or a 1500 surface area to footprint advantage. NS has no closed pore (not accessible from the external) and 99.8 % of the surface area is accessible to solvents and gases. Moreover, given the flexible surface chemistry of NS, several processes have been developed that allow their surface modification: atomic layer deposition (ALD), plasma enhanced chemical vapor deposition (PECVD), wet impregnation, and thiol functionalization.

1.4 Overview of the Study

In this dissertation, Chapter 2 describes the experimental techniques and instrumentation used throughout the study for physical, chemical, and electrical characterization. In Chapter 3, the electronic structure of NS coated with ZnO and subsequently decorated with differing metal nanoparticles are investigated, along with their chemiresistors capabilities (vapor sensing properties). A thorough characterization including surface electronic structure of SAMs of thiols adsorbed on Au/ZnO coated NS and their responsiveness to vapors of ammonium nitrate, a signature of explosive materials, is presented in Chapter 4. The FTS catalytic performances of Co supported on NS (Co/NS) are evaluated in the first part of Chapter 5, the second part being devoted to the description of the reduction state of Co/NS during activation. Finally, Chapter 6 is a summary of the study, where the important conclusions, the implications, and the future outlook are outlined.

References

(1) Grass, M. E., Joo, S. H., Zhang, Y. & Somorjai, G. A. Colloidally Synthesized Monodisperse Rh Nanoparticles Supported on SBA-15 for Size- and Pretreatment-Dependent Studies of CO Oxidation. *J. Phys. Chem. C* **113,** 8616–8623 (2009).

(2) Yang, S. B., Kong, B.-S., Kim, D.-W., Baek, Y.-K. & Jung, H.-T. Effect of Au Doping and Defects on the Conductivity of Single-Walled Carbon Nanotube Transparent Conducting Network Films. *J. Phys. Chem. C* **114,** 9296–9300 (2010).

(3) Hori, H. *et al.* Diameter dependence of ferromagnetic spin moment in Au nanocrystals. *Phys. Rev. B* **69,** (2004).

(4) Smart, S. *et al.* The effect of carbon nanotube hydrophobicity on the mechanical properties of carbon nanotube-reinforced thermoplastic polyurethane nanocomposites. *J. Appl. Polym. Sci.* NA–NA (2010). doi:10.1002/app.31115

(5) Nehl, C. L. & Hafner, J. H. Shape-dependent plasmon resonances of gold nanoparticles. *J. Mater. Chem.* **18,** 2415 (2008).

(6) Srisombat, L., Park, J.-S., Zhang, S. & Lee, T. R. Preparation, Characterization, and Chemical Stability of Gold Nanoparticles Coated with Mono-, Bis-, and Tris-Chelating Alkanethiols. *Langmuir* **24,** 7750–7754 (2008).

(7) Ivanov, M. R. Covalently functionalized gold nanoparticles: synthesis, characterization, and integration into capillary electrophoresis. (2011). at <http://ir.uiowa.edu/etd/987.>

(8) Dobrokhotov, V. *et al.* ZnO coated nanospring-based chemiresistors. *J. Appl. Phys.* **111,** 044311 (2012).

(9) Heinrich, A. J., Lutz, C. P., Gupta, J. A. & Eigler, D. M. Molecular Cascades. *Science* **298,** 1381–1387 (2002).

(10) Hogg, T. Robust self-assembly using highly designable structures. *Nanotechnology* **10,** 300–307 (1999).

(11) Nuzzo, R. G., Dubois, L. H. & Allara, D. L. Fundamental studies of microscopic wetting on organic surfaces. 1. Formation and structural characterization of a self-consistent series of polyfunctional organic monolayers. *J. Am. Chem. Soc.* **112,** 558–569 (1990).

(12) Vossmeyer, T. *et al.* Gold Nanoparticle/Polyphenylene Dendrimer Composite Films: Preparation and Vapor-Sensing Properties. *Adv. Mater.* **14,** 238–242 (2002).

(13) Zamborini, F. P. *et al.* Electron Hopping Conductivity and Vapor Sensing Properties of Flexible Network Polymer Films of Metal Nanoparticles. *J. Am. Chem. Soc.* **124,** 8958–8964 (2002).

(14) Scott, A. & Janes, D. B. Characterization of electrochemically grafted molecular layers on silicon for electronic device applications. *J. Appl. Phys.* **105,** 073512 (2009).

(15) Aviram, A. & Ratner, M. A. Molecular rectifiers. *Chem. Phys. Lett.* **29,** 277–283 (1974).

(16) U.S. Energy Information Administration. *U.S. Energy Information Administration / Annual Energy Review 2011*. 370 (2012).

(17) *Thermochemical processing of biomass: conversion into fuels, chemicals and power*. (John Wiley & Sons, 2011).

(18) Wang, Z., Yan, Z., Liu, C. & Goodman, D. W. Surface Science Studies on Cobalt Fischer-Tropsch Catalysts. *ChemCatChem* **3,** 551–559 (2011).

(19) American Chemical Society. *Industrial chemicals via C_1 processes*. (American Chemical Society, 1987).

(20) Tsakoumis, N. E., Rønning, M., Borg, Ø., Rytter, E. & Holmen, A. Deactivation of cobalt based Fischer–Tropsch catalysts: A review. *Catal. Today* **154,** 162–182 (2010).

CHAPTER 2
Experimental Techniques and Instrumentation

2.1 Sample Preparation

2.1.1 Synthesis of Nanospring-mats

All the nanosprings (NS) used in this study were grown via a vapor-liquid-solid (VLS) mechanism. VLS growth proceeds through three steps: alloying, nucleation and growth (Fig 2.1).

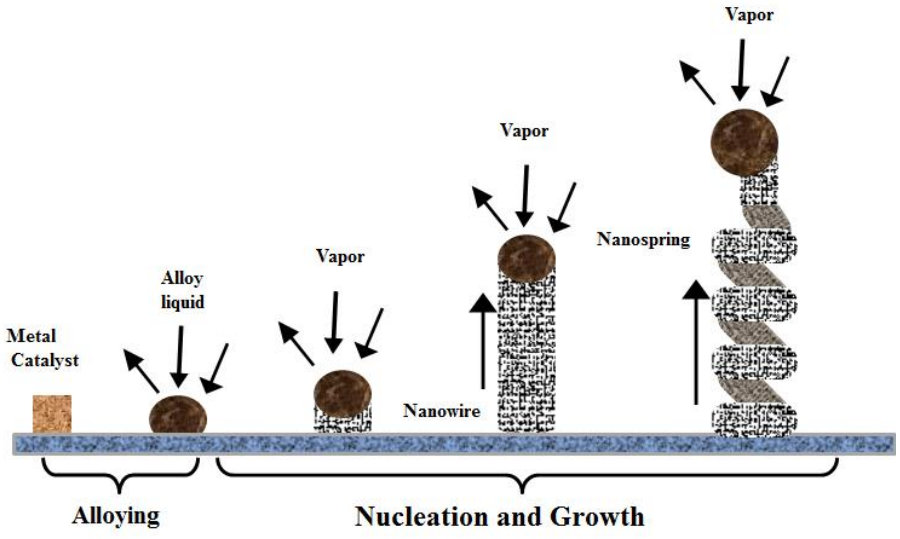

Figure 2.1 An illustration of the VLS growth mechanism for nanowire and nanospring. VLS mechanism utilizes a metal catalyst for crystallization from the vapor. When heated inside a reactor, the metal thin film breaks up and liquid nanodroplets are formed, which serve as the catalyst. The molten catalyst, now in the form of droplets, absorbs vapors of the precursors from the surrounding atmosphere. As the droplet absorbs more and more vapor it eventually becomes supersaturated, at which point a nanowire is initiated at the catalyst-substrate interface (nucleation). The continuous feeding and subsequent precipitation results in the formation of a solid wire structure between the substrate and the catalyst (growth). The

growth ceases if there is insufficient quantity of reactants in the vapor or the catalyst solidifies (freezes). In other words, the temperature should be kept above the melting point of the catalyst concomitant with a steady flow of reactants. As long as the liquid catalyst particle is sitting symmetrically atop the structure, the morphology, in general, is a nanowire (linear growth). The helical growth of NS is attributed to the offset of the center of mass of the catalyst from the axis of the nanowire.[1]

The technology for NS growth has been previously reported by Wang et al.[2] and McIlroy et al.[1] NS synthesis was performed in a furnace operated at atmospheric pressure. The general principles of the furnace were discussed in detail by McIlroy et al.[1] Briefly, the process uses a thin gold layer as a catalyst, which is then exposed to a proprietary silicon precursor. During the NS synthesis, a constant N_2/O_2 flow rate is maintained concomitant with the silicon precursor. With a growth time of 30-45 minutes, a 80 μm thick nanospring-mat is achieved. Typical field emission scanning electron microscopy (FESEM) images of a nanospring-mat and single nanospring are shown in Figure 2.2.

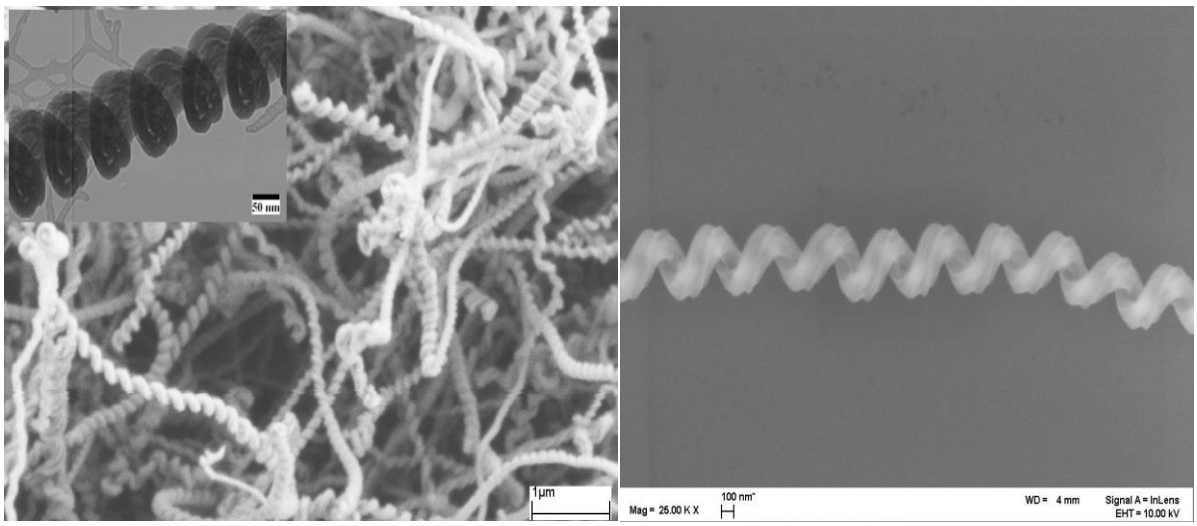

Figure 2.2 FESEM micrographs of nanosprings (The inset is a TEM image).

It is apparent from the examination of the inset in Figure 2.2 that the silica NS are comprised of multiple nanowires, in the range of five to eight with a typical diameter of 20 nm, that coherently coil to form the nanospring [1].

2.1.2 Metal Nanoparticle Decoration of Nanosprings

Nanosprings are first grown on a substrate specific to the application. Aluminum foil, Si wafer, glass frit, and stainless steel mesh are used as substrate in this study, but NS grow on almost anything that can withstand the growth temperature. The subsequent metal nanoparticles decoration is achieved by a wet impregnation process. In this process, the precursor solution is prepared by dissolving an organometallic compound in an appropriate solvent; the typical metal concentration used is 19.5 mM. This molarity, multiplied by the molecular weight of the metal precursor, yields the mass concentration (amount of precursor per unit volume of solvent). The NS-coated sample is dipped in the metal-containing solution, and after allowing the volatiles to evaporate, the sample is reduced in a preheated tube furnace (see Table 2.1) under a flow of Ar/H_2 (130/10 $mL.min^{-1}$) for 15 minutes. The procedure is repeated, as needed, to obtain the desired metal nanoparticle loading. The table below describes the precursors used and the reduction temperatures for all the metal nanoparticles.

Table 2.1 Metal precursors and their reduction temperature (T_R)

Metal	Gold	Silver	Palladium	Platinum	Cobalt	Nickel
Precursor	$AuCl_3$	AgCl	$PdCl_2$	$Pt(Acac)_2$	Co(Acac)3	$NiCO_3.2Ni(OH)_2.xH_2O$
T_R (°C)	300	300	500	500	500	450
Particle size (nm)	10±4	10	2.4±0.2	-------	10.4±2	-------

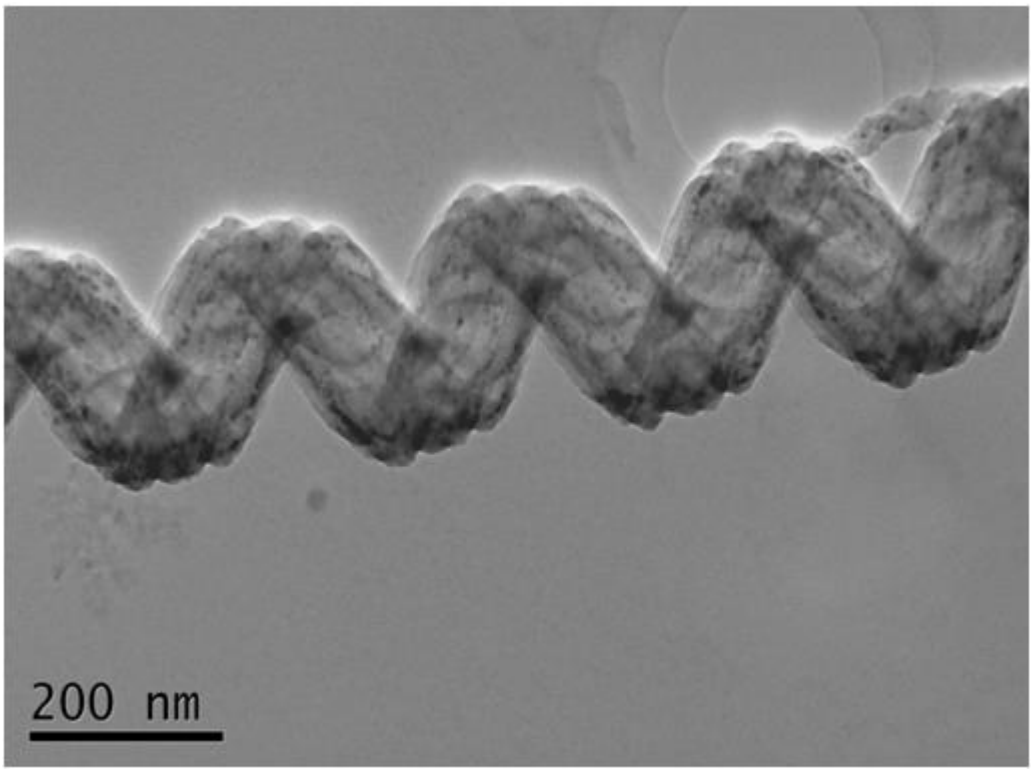

Figure 2.3 TEM image of a cobalt decorated nanospring.

Transmission electron microscopy (TEM) is used for particle size measurement and size distribution. The particle size was measured using in-house computer program that compared the size of each particle to the scale bar. Using TEM images from different areas of the sample, the statistical average size was obtained from surveying multiple nanosprings. The results are presented in Table 2.1. For nickel and platinum, there was a lack of contrast that made it difficult to resolve the nanoparticles.

2.1.3 Atomic Layer Deposition (ALD) Coating of Nanosprings

For sensing applications, NS were coated with a thin layer of ZnO using the technique of atomic layer deposition (ALD). ALD utilizes a binary reaction sequence of self-saturating chemical reactions between gaseous precursor molecules and a solid surface to deposit films in a monolayer-by-monolayer fashion.[3-4] The diagram in Figure 2.3 is a schematic representation of the custom ALD reactor used in this work. Pneumatically actuated valves and the vacuum gate valves are controlled with a LABVIEW-based algorithm. The former are sequenced to deliver each reactant and purge gas to the reactor or bypass line.

The precursors are alternatively introduced into a growth chamber, which is a viscous flow ALD reactor.[5] The pulses of precursors are interspersed between purging nitrogen. Therefore, chemical reactions inside the chamber volume are effectively avoided and precursors meet and react only on the surface of the growing film.[6] The reaction products and surplus reactants are carried first into a cold trap and finally into a mechanical pump. The cold trap keeps them from combining in the pump to form particles. The flow tube is heated radiatively by convection to the desired deposition temperature. Films grown using ALD are extremely conformal to the underlying substrate.[5] At low growth temperatures ALD ZnO films retain their favorable properties, thereby enabling the construction of hybrid organic/ZnO materials.[7]

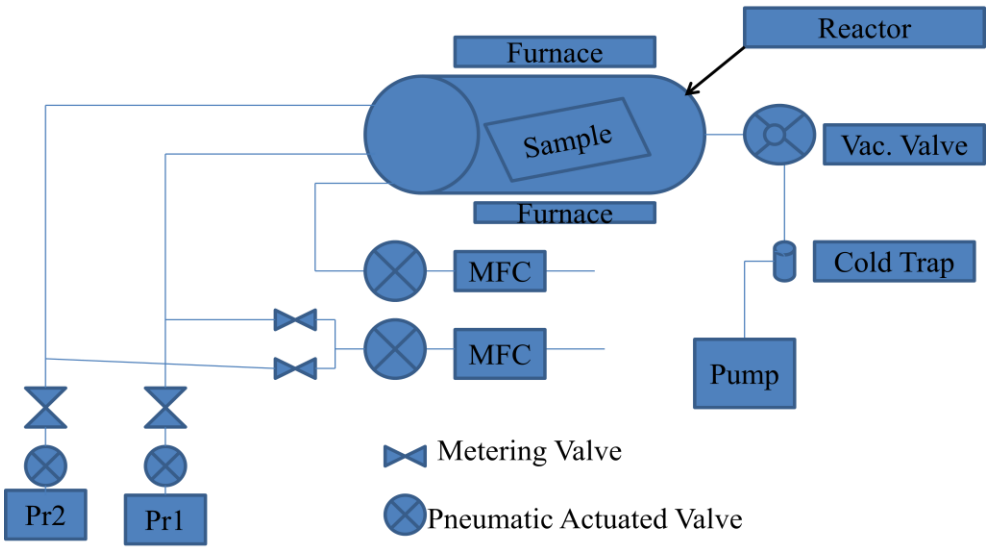

Figure 2.4 Schematic diagram of the atomic layer deposition system used in this study.

For NS ZnO coating, ALD was performed in a clear quartz reactor, heated by a Lindberg/Blue single zone programmable tube furnace operated at 170℃, which is in the so-called "ALD window" reported to range from 100-200°C for ZnO.[8] The volatile metalorganic diethyl zinc (DEZn) was the zinc precursor and deionized water was the oxygen precursor. High purity N_2 was used both as carrier and purging gas. Pulses of the precursors were injected into the carrier gas flow using the computer- controlled pneumatically actuated valves. The amplitudes of the precursor pulses were adjusted using metering valves. The chemical formation of ZnO is described by the following equation:

$$Zn(C_2H_5) + H_2O \rightarrow ZnO + 2C_2H_6 \qquad (2.1)$$

The thickness of the ZnO layer is controlled by the number of cycles and the precursor pulse widths. Precursors cycle times were ~ 0.25 s or less, and the N_2 purge and pump times 20-25 s. A typical ZnO coating on the nanosprings was obtained with 200 cycles. Subtle changes in the pump and purge times provides control over the size of the ZnO nanocrystals. SEM

imaging of ZnO/nanosprings shows that the range of average grain sizes is between 3 nm and 100 nm, depending on the ALD conditions. Long (short) purging time privileges growth with c-axis perpendicular (parallel) to the surface.[7] Smaller (larger) grain size is therefore obtained for longer (shorter) purging time. A double cycle deposition was created where a 10 nm thick semiconductor layer, with an initial 1nm layer deposited on the nanosprings, followed by a second ZnO layer, with shorter water purging time (20 s), which produced a ~9 nm nanocrystals uniformly distributed on the surface of the nanosprings. A field emission scanning electron microscopy (FESEM) micrograph of a typical ZnO-coated silica nanospring mat is shown in Figure 2.4.

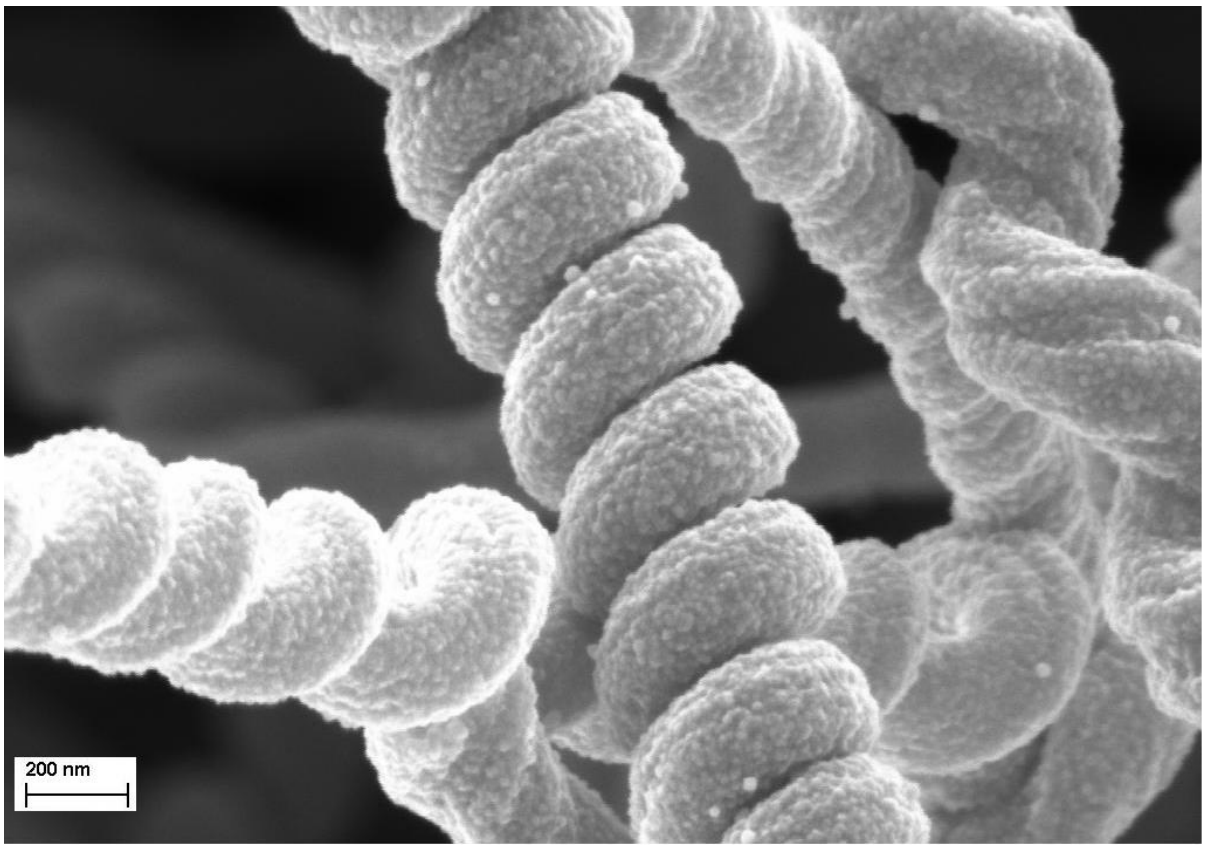

Figure 2.5 FESEM micrograph of a mat of ZnO-coated silica nanosprings (200 cycles).

2.2 Physical Characterization of Samples

2.2.1 Electron Microscopy

As demonstrated above, electron microscopy is one of the most important tools for sample characterization. Surface morphologies can be visualized, the particle size can be measured, and the crystal structure deduced from the diffraction pattern. The elemental composition of the samples can also be determined using energy dispersive X-ray or spectroscopy (EDX or EDS). In this process electrons of the probe beam can excite electrons of the elements of the sample into excited state, where upon relaxation X-rays are produced, otherwise known as fluorescence. The beam travels through a vacuum in the column of the microscope and is condensed and focused on the sample by electromagnetic lenses. For SEM, when the primary beam strikes the surface of the sample, the atomic structure of the sample is excited and secondary electrons are emitted from the sample. As the beam scans the sample in a two dimensional pattern, the emitted secondary electrons are collected by a detector and a magnified image of the details of the surface structure is built up. For FESEM, a strong electric field is used to draw electrons from a wire (Tungsten single crystal) instead of thermionic sources (Tungsten and LaB_6 emitters) used in SEMs.

In a TEM, the electron beam travels through the specimen. At the bottom of the microscope the unscattered electrons hit a fluorescent screen, which gives rise to a “shadow image” of the specimen. The image is then photographed by a camera.

FESEM and TEM characterizations were performed using a Zeiss Supra 35 SEM equipped with an EDS spectrometer and (Jeol JEM-2010 TEM, 200kV), respectively. Specimens for TEM were prepared by scraping the nanosprings off the substrate upon which they were

grown, followed by dispersion in ethanol, and subsequent dropping the suspension onto a copper grid and allowing the ethanol to evaporate.

2.2.2 Nitrogen Physisorption and Hydrogen Temperature Programmed Reduction (H_2-TPR)

The specific surface area and the pore size distribution of a substrate can be determined from nitrogen adsorption isotherm at 77 K. The Brunauer-Emmett-Teller (BET) isotherm for multilayer coverage is given by:[9]

$$\frac{x}{V(1-x)} = \frac{1}{V_m C} + \left(\frac{C-1}{V_m C}\right)x \qquad (2.2)$$

where V is the adsorbed amount of adsorbate at relative pressure x ($x = P/P_0$) with adsorbate pressure P, and adsorbate saturated vapor pressure (P_0) at 77 K, V_m the amount of adsorbate needed for monolayer coverage of adsorbent and C the equilibrium constant of adsorption in the first adsorption layer.

Plotting the experimental data in the form of x/V(1-x) versus x, the y-axis intercept ($1/CV_m$) and the slope ($(C-1)/V_mC$) can be determined. In turn, the values of V_m and C are obtained. Then the specific surface area of the sample A_s is evaluated from V_m using the area covered by an individual molecule of the adsorbate σ (for nitrogen adsorption at normal boiling point of nitrogen a value of 0.162 nm^2 is commonly applied), as the follows:[10]

$$A_s = \frac{V_m N_A \sigma}{22414m} \qquad (2.3)$$

,where V_m is the monolayer volume, N_A is the Avogadro's number, σ is the area covered by one molecule of the adsorbate, and m is the mass of the sample.

The Barret-Joyner-Halenda (BJH) [11] method is widely used for the determination of the pore volume and pore size. In the capillary condensation region of the isotherm ($P/P_0 > 0.4$), each

pressure increase causes an increase of the thickness of the layer adsorbed on the pore walls. The capillary condensation in the pores has a core (which is the empty space in the pores after adsorption of the monolayer) size r_C, as defined by the Kelvin equation:[10-12]

$$\ln\left(\frac{P}{P_0}\right) = \frac{-2\gamma\omega_m \cos\varphi}{RTr_C} \qquad (2.4)$$

,where r_C is the radius for cylindrical pores or distance between walls for slit shaped pores, γ is the surface tension of the adsorbate, ω_m is the molar mass, and φ the contact angle. From the assumed geometry (cylindrical and slit shaped), the contribution of the adsorbed film to the total volume and then the core volume are calculated. The core volume is transformed into pore volume and the core size into pore size.[11]

The specific surface area, pore volume, and average pore radius of the supports and catalysts were determined by N_2 physisorption using a (Micromeritics TriStar II 3020). Before the analysis, samples were degassed at 300°C for 1 h under vacuum. The specific surface area was obtained using the (BET) model and the pore size by the BJH method.

For H_2-TPR, a defined amount of catalyst powder is inserted in a quartz reactor and oxidized by flowing oxygen, if needed, to ensure a well-defined oxidation state for the starting catalyst. The sample is then cooled under an inert gas flow. At the start temperature, the inert gas flow is switched to a flow of argon containing a small percentage of hydrogen, at which point the temperature is linearly increased. The rate of the reduction is monitored by measuring the composition of the reducing gas mixture at the outlet of the reactor. The experiment allows the determination of hydrogen consumed, from which the degree of reduction and, thus, the oxidation states can be deduced. The reduction peaks appear at specific temperatures corresponding to maxima in the hydrogen uptake.

H_2-TPR spectra of the catalysts were recorded using a Micromeritics AutoChem II 2920 Chemisorption Analyzer, equipped with a thermal conductivity detector (TCD). A sample (50 mg) was loaded in a U-shape quartz reactor and purged in a flow of He (50 mL.min^{-1}) at 250ºC for 1 h to remove water, cooled to 50°C, then purged, followed by exposure to an atmosphere of 10% H_2 in Ar (50 mL min^{-1}) and heated to 800ºC at 10°C min^{-1}.

2.2.3 X-ray Diffraction (XRD)

Interaction of X-rays with a crystal creates a secondary "diffracted" beam of X-rays whose pattern is characteristic of the crystal structure. In fact, diffraction peaks appear in the pattern only if constructive interference occurs after diffraction by two planes. This is the case only when Bragg's law ($n\lambda = 2d\sin\theta$) is satisfied, where n is an integer, θ is the diffraction angle, λ is the wavelength of the radiation and d is the inter-planar spacing between crystal planes.

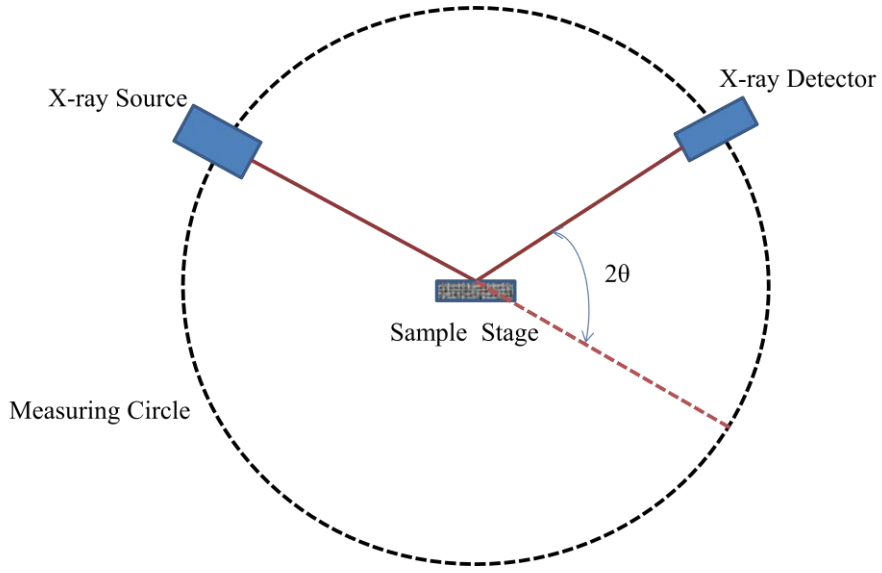

Figure 2.6 Schematic diagram of a diffractometer.

The X-ray powder diffraction (XRD) patterns were obtained using a Siemens D5000 powder diffractometer with Cu/Kα radiation (λ = 1.54 Å). The spectra were recorded with 0.01° steps

using a 1.00 s acquisition time per step. The average particle size of the particles was calculated according to Scherrer's equation ($d = K\lambda/\beta\cos\theta$), where K is the shape factor ($K = 1$), λ is the wavelength of X-ray, β is the line broadening at half the maximum intensity (FWHM) in radians, and θ is the Bragg angle.

2.2.4 X-ray Photoelectron Spectroscopy (XPS)

XPS is based on the photoelectric effect, where the emission of electrons is observed when a material is exposed to ionizing electromagnetic radiation. In XPS, electrons have absorbed a photon of sufficient energy ($E = h\nu$) to be ionized and to overcome the work function of the material (W), thereby emerging as a free, or unbound, electron with non-zero kinetic energy. The experimental quantity that is measured is the kinetic energy of the electron E_K, which is dependent on the photon energy ($h\nu$) of the primary X-ray source. The binding energy of the electron (E_B) is the initial state of the photoemitted electron in its bound state. The relationship between the parameters involved in the XPS experiment is

$$E_B = h\nu - E_K - \Phi \qquad (2.5)$$

,where the remaining parameter Φ is the work function and is dependent on the difference between the work function of the material and the detector (electron energy analyzer).

The XPS process is schematically depicted in Figure 2.6, where an electron from the 1s shell is ejected from an atom.

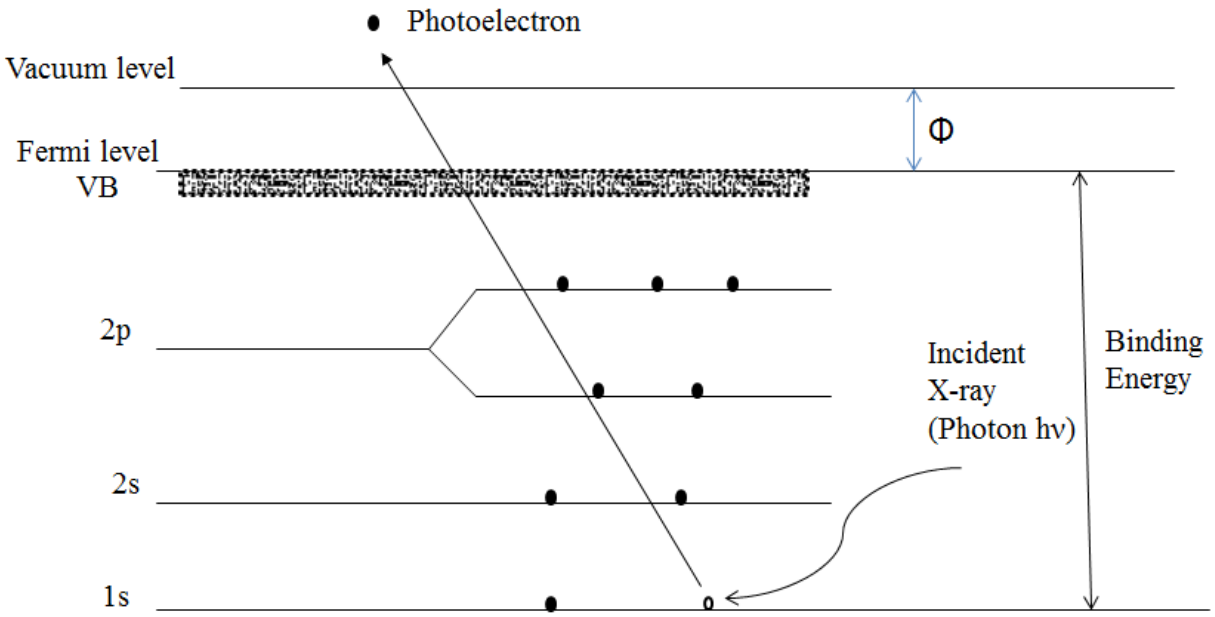

Figure 2.7 Schematic representation of the XPS process, showing photoionization of an atom by ejection of a 1s electron.

Each chemical element has a characteristic electronic structure and, thus, a characteristic XPS spectrum. Figure 2.8 shows the XPS spectrum of Au.

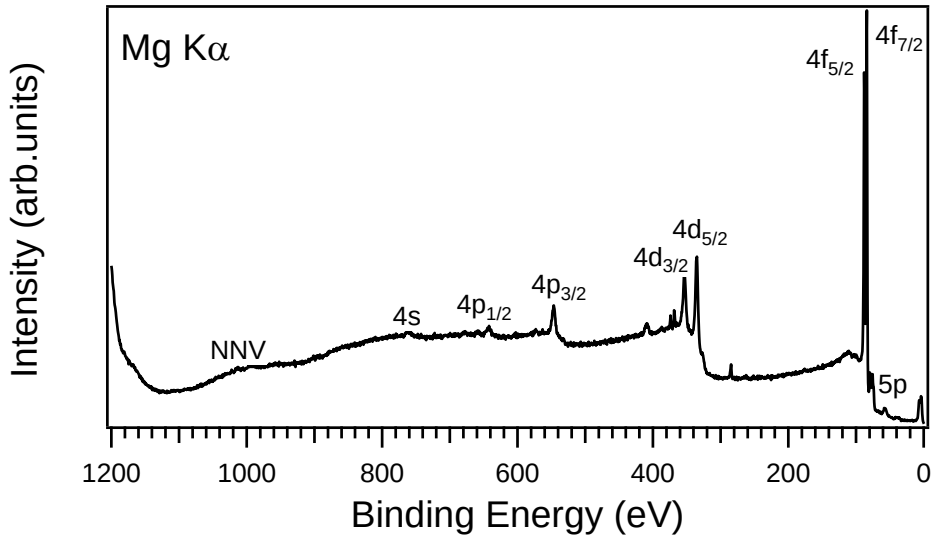

Figure 2.8 XPS spectrum of Au. Conditions: Mg Kα (hν = 1253.6 eV) at a source power of 400 W, and an energy analyzer pass energy = 50 eV.

The peaks appearing on a background correspond to electrons which are excited and escape without energy loss, while the background originates from those that undergo inelastic scattering, i.e. their kinetic energy isn't conserved. The observed peaks can be grouped into three categories: peaks originating (i) from core levels, (ii) from valence levels (0-20 eV) and (iii) from X-ray excited Auger emission. The nomenclature employed to describe XPS peaks is based on the momenta associated with the orbital of the electrons of a specific element, indicated by quantum numbers n, l, j. XPS uses the spectroscopic notation: first the principal quantum number (n =1, 2, 3…), then l = 0, 1, 2,… indicated as s, p, d, …, respectively, and finally the j value given as suffix (1/2, 3/2, 5/2, …). The peaks in the spectra deriving from orbitals whose angular momentum quantum number is greater than zero (l>0) are usually split into two, which are two states with different total angular momentum $j = l \pm s$. This is the result of the interaction of the electron spin with the orbital angular momentum known as spin-orbit coupling. These two states show up in the XP spectra with energetically separate peaks, whose area is proportional to the number of projected states m_j for each value of j (degeneracy = 2j+1). The peaks' separation is called spin-orbit splitting, which depends upon the strength of the spin orbit coupling. For a given value of both n and l the separation increases with the atomic number of the atom. For a given atom it decreases with both increasing n and with increasing l. The relative intensities of XP peaks are governed by the ionization efficiencies of the different core shells, designated by photoionization cross-section. The line width, defined as the full width at half-maximum (FWHM), is a convolution of several contributions: the natural width of the core level, the width of the X-ray line and the resolution of the spectrometer.

As just described, the XPS spectrum provides compelling evidence for the quantization of the atomic energy levels. The X-ray induced Auger emission is one of the ways atoms in an excited state relax, the other being the X-ray fluorescence. Both decay phenomena are illustrated in Figure 2.9.

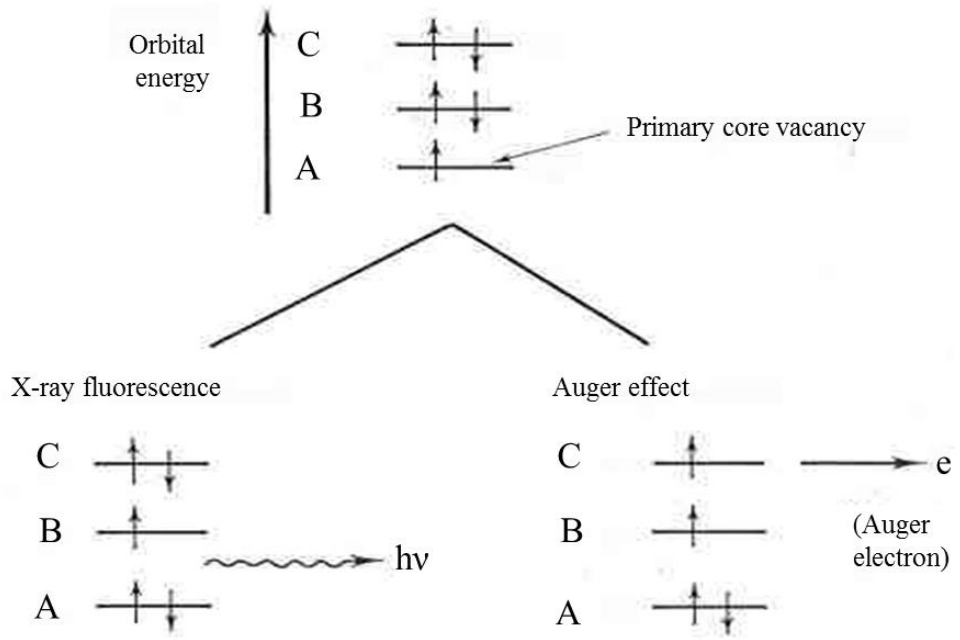

Figure 2.9 Energy level diagrams illustrating the alternative modes of decay of a core hole state.[13]

Satellite Features

Satellite features stem from multielectron processes in photoemission and appear at the higher binding energy side of the main peaks. They are namely plasmons, shake-up and shake-off satellites.

Shake-up Satellites

They occur when the outgoing photoelectron excites a valence electron to a higher energy level (shakes it up). The energy of the core electron is then reduced slightly, giving rise to a satellite feature a few electron volts above the binding energy of the core level position. The dominant factor in their generation is the final-state effects (possibilities that the electronic states of the photoionized atom may be different from that of the initial state, usually the atomic ground state) such as the screening of the core hole by valence electrons, the relaxation of electrons orbitals and the polarization of the surrounding species. Shake-up satellites are useful in identifying many metal oxides.

Shake-off Satellites

They are generated in the same manner as the shake-up satellites, but the only difference is that the valence electron is ejected from the ion completely. They appear as a broadening of the core level peak or as contributions to the background.

Plasmons

They arise when the outgoing photoelectron excites collective longitudinal oscillations in the conduction band electrons and suffers a discrete energy loss in multiples of the plasmon energy. They appear at the high binding energy side of the main photoemission peak.

Core-level Binding Energy Shift (Chemical Shift)

Non-equivalence of atoms of the same element can arise in several ways: difference in the oxidation state, difference in the molecular environment, difference in lattice site.., etc. Within the charge potential model [13-14] the binding energy E_i of a particular core level on an atom i depends on the partial charge of the atom itself and the charges of the surrounding atoms within the chemical structure

$$E_i = E_i^0 + kq_i + \sum_{j \neq i} \frac{q_j}{r_{ij}} \quad (2.6)$$

, where E_i^0 is the binding energy of the unsubstituted atom, k is a constant, q_i the partial charge on atom i, and the last term is the potential on atom i (V_i) due to "point charges" on surrounding atom j.

A change in the chemical environment gives rise to a spatial redistribution of valence charges and a different potential created by the nuclei and electronic charges of other atoms in the compound. Thus, the shift in binding energy for a given core level of atom i in two different environments is:[15]

$$E_i^{(1)} - E_i^{(2)} = k(q_i^{(1)} - q_i^{(2)}) + (V_i^{(1)} - V_i^{(2)}) \quad (2.7)$$

, where the first term ensures that increases in the binding energy accompanies decrease in the valence electron density on atom i,[16] the second term is the Madelung potential. Final-state effects (intra-atomic and extra-atomic relaxation effects) as mentioned above are the major contributing factors to binding energy shift.

2.2.5 Ultraviolet Photoelectron Spectroscopy (UPS)

For UV photoemission the electrons are excited by a low energy photon source (10 eV < hν < 100 eV). The photoionization cross-section of valence electrons are less for X-ray than for UV radiation, which makes UPS a powerful tool to probe electronic structure at surfaces because the valence states are prominent and thus better resolved. Note, there is no well-defined boundary between valence states and core states. Valence states can extend to 10-15 eV in the binding energy scale and core levels can be as shallow as a few eV. Surface states, sometimes referred to as "dangling bonds", are equally important. Surface states are electron orbitals primarily localized at or near the surface, but in general delocalized in two

dimensions over the surface, whose existence stems from the presence of the solid-vacuum discontinuity. The most compelling indication of a surface state is the disappearance of the photoemission signal when a sub-monolayer quantity of gas is allowed to adsorb onto the surface: this destroys the solid-vacuum interface, and hence the surface states.

For adsorption studies, the chemical relevance of UPS relies on the fact that small energy shifts caused by electronic adsorbate-substrate interactions, or by surface states, can be detected. Bonding shifts of adsorbates can be studied by comparison with gas phase UPS adsorbate spectra.[17] The strength of the binding energy shift allows distinction between physisorption and chemisorption. A UPS spectrum of a molecularly modified metal surface generally shows superposition of the band structure of the substrate with specific spectral lines stemming from the electronic structure of the adsorbate. The background corresponds to inelastically scattered photoelectrons that still have enough energy to escape into the vacuum. Photoelectron attenuation in the overlayer results in a decrease of the Fermi edge and of the valence band states of the substrate.

The sample work function Φ can be obtained from a UPS spectrum by subtracting the width W of the emitted electrons from the photon energy ($\Phi = h\nu - W$). W is measured from the onset of secondary electrons to the Fermi edge.

XPS/UPS Instruments

A typical photoelectron spectroscopy system consists of: (i) an X-ray source for XPS and/or a UV source for UPS, (ii) an electron energy analyzer, combined with a detection system and (iii) a sample stage, all assembled in an ultra-high vacuum (UHV) chamber with base vacuum in the range of 10^{-8} to 10^{-10} Torr. The reasons for an UHV are to improve the detection of photoelectrons (attenuation by gases) and to avoid surface contamination by the

surrounding atmosphere. In the case of the photon energies in this study, namely, 1253.6 eV X-rays and 21.2 eV UV light, they are adsorbed by air. Furthermore, the low energy electrons are scattered by residual gas molecules leading to loss of energy, so that not only the intensity of the peaks is attenuated, but the signal to noise of the spectra is low. Lowering the vacuum level to 10^{-6} Torr, for example, would immediately result in a monolayer of residual gas adsorbed onto the sample surface in less than a second. An example of a complete XPS/UPS system is shown in Figure 2.10, while Figure 2.11 shows a schematic diagram of an XPS/UPS with an X-ray source, a UV source and a hemispherical sector analyzer (HSA).

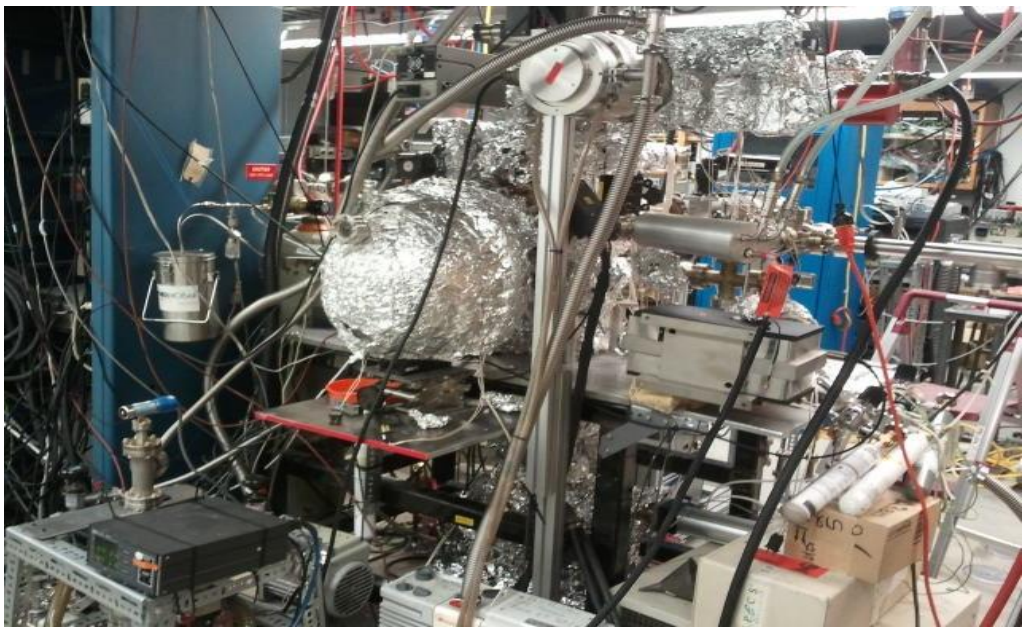

Figure 2.10 Picture of a custom built full setup for XPS and UPS.

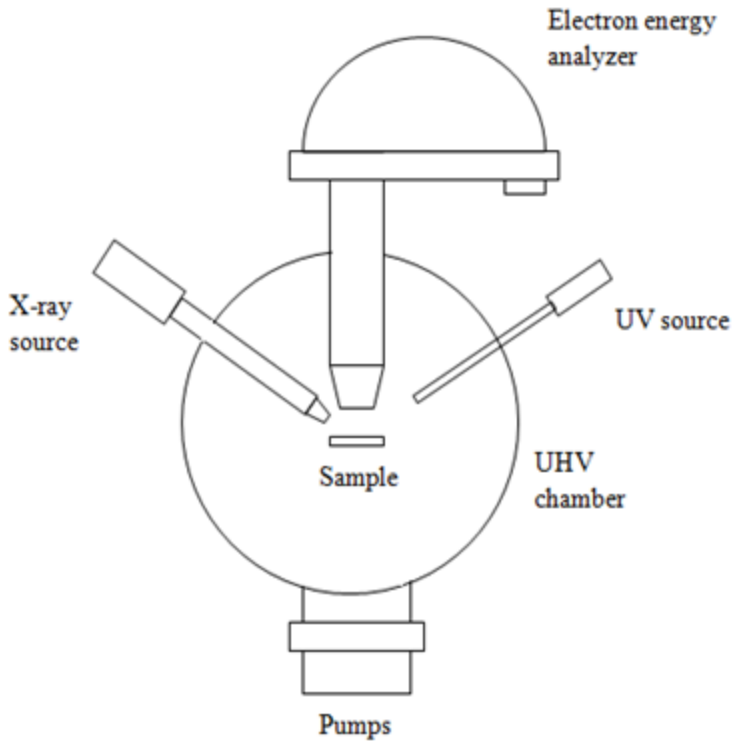

Figure 2.11 Schematic representation of an XPS/UPS setup with a hemispherical sector analyzer.

X-rays are generated by bombarding an anode with high energy electrons. The most popular anode materials are aluminum and magnesium housed in a single dual anode X-ray gun. Al Kα and Mg Kα X-rays have energies of 1486.6 eV and 1253.6 eV, respectively. On the other hand, the source of UV radiations is normally a noble gas discharge lamp. The most common is the He-discharge lamp that emits 21.2 eV (He I) 40.8 eV (He II) photons, respectively. XPS from insulating samples causes electrostatic charging on the surface to occur, resulting in a shift in the peak position in the direction of higher binding energy. To overcome, or eliminate, this artifact of photoemission process, charge compensation is achieved with an electron flood gun that ‘floods’ the sample with low energy electrons.

For the HSA, a potential difference is applied across the two hemispheres with the outer hemisphere being more negative than the inner hemisphere. Electrons injected tangentially at the input will only reach the detector if their energy is given by:

$$E_p = e\Delta V\left(\frac{R_1 R_2}{R_1^2 - R_2^2}\right) = ke\Delta V \tag{2.8}$$

,where E_p is the kinetic energy of the electrons, e the charge of an electron, k is the spectrometer constant, ΔV is the potential difference between the hemispheres and R_1 and R_2 are the radii of the inner and outer hemispheres, respectively. A channel detector system (channel electron multiplier or channeltron) is used to improve the sensitivity of the HSA. The number of channeltrons can vary from one to as many as sixteen for a multimode detection system.

Electrons entering the analyzer on the mean radius will reach the exit slit. Electrons whose energy is higher than E_p follow trajectories whose radii is larger than the mean radius of the analyzer, and those with low kinetic energy follow trajectories with smaller mean radius of the analyzer.

The HSA operates in two modes: constant analyzer energy (CAE), also called fixed analyzer transmission (FAT) and constant retard ratio (CRR), also known as fixed retard ratio (FRR). In the CAE mode electrons are accelerated or retarded to some user-defined energy (E_p, pass energy) which is the energy the electrons possess as they pass through the analyzer. Those electrons with energies matching the pass energy are transmitted, detected and eventually amplified into pulses by the channeltron. The retarding field is then ramped, and such the electrons are counted as a function of energy. The advantage in this case is a constant energy resolution in the spectrum as a function of the energy, which explains why the CAE mode is

widely used. The pass energy in the region of 20 eV is used for high-resolution scans of individual core levels.

In the CRR mode, the voltages of the hemispheres are changed with the energy of the spectrum so that the ratio of the electron kinetic energy to pass energy is constant (retard ratio). In this mode the transmission function is optimized at the expense of the energy resolution.

Information in XPS

For XPS the primary beam has a penetration depth of a few micrometers. The photoelectrons can only travel a limited distance, called the attenuation length λ, before being inelastically scattered. Note, the attenuation length depends on the electron kinetic energy, i.e. λ(E). The characteristic depth d from which photoelectrons are emitted, defined as the escape depth d, is given by:

$$d = \lambda(E)\cos\theta \qquad (2.9)$$

, where θ is the angle of emission of photoelectron from the surface normal. The attenuation length depends on the element which is emitting the electron and the matrix element of the transition, which depends on the energy of the transition. Typical values of λ are, as shown in Figure 2.11, in the range of 1 to 10 atom layers.[18] This is the basis for the surface sensitivity of XPS and UPS.

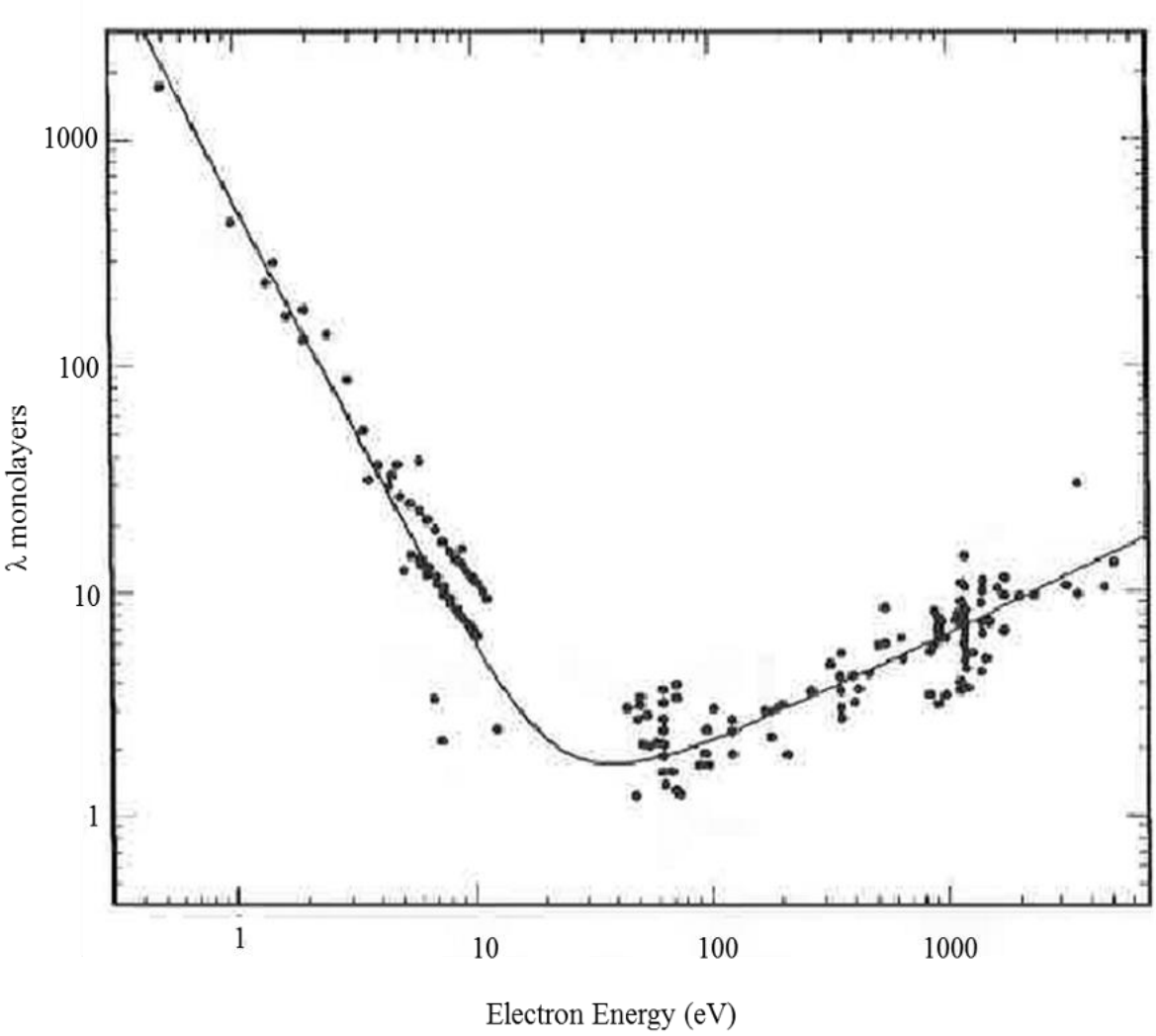

Figure 2.12 Attenuation length versus electron energy.[18]

Qualitative Analysis

Qualitative analysis consists in identifying the elements that are present in the surface region of the sample. A survey or wide scan is recorded for the purpose of determining the elemental composition of the sample in question. With the help of a library (software), the identification of the peaks is straightforward, except if peaks are overlapping.

Quantitative Analysis

To determine the surface composition of the sample in question, individual peaks are scanned in a high energy resolution. The peak intensity I_A of a core level associated with an element A depends on the concentration N_A of the element A in the sample, the photoionization cross section σ_A, the attenuation length λ_A, the angular distribution factor Φ and the spectrometer transmission function T. This can be written simply as:[19]

$$I_A \propto N_A \lambda_A \sigma_A \Phi T \qquad (2.10)$$

The molar fraction x_A in a homogeneous sample composed of ith elements, assuming that Φ and T remain constant during the experiment, is given by:

$$x_A = \frac{N_A}{\sum N_i} = \left(I_A / S_A\right) / \sum \left(I_i / S_i\right) \qquad (2.11)$$

, where I_i is the area of the peak generated by constituent i, N_i is the number of moles of the ith element, $S_i = \sigma_i \lambda_i$ its atomic sensitivity factor. For the peak area measurement, the background must be subtracted. The Shirley [20] or the Tougaard [21] background correction procedures are the two most widely used methods. The measurement must also include or be corrected for, X-ray satellites, chemically shifted species, shake-up peaks, plasmons or other losses.

Chemical Analysis

A clear shift in the binding energy of a core level peak in XPS is indicative of differences in the chemical environment of the emitting element. The capability to distinguish between different chemical states is the main capability of XPS, hence its other acronym ESCA (Electron Spectroscopy for Chemical Analysis). To extract chemical information, the peak position must be determined accurately and the peak recorded with the highest resolution possible. In case of overlapping peaks, peak deconvolution is necessary.

Photoelectron spectroscopy was performed in a custom built ultrahigh vacuum (UHV) chamber (Figure 2.9) with a base pressure of $1.5x10^{-10}$ Torr. The chamber is equipped with an Omicron model EA 125 hemispherical electron energy analyzer, a dual anode X-ray source, and a He UV lamp. Both the X-ray source and the UV lamp are at the so-called magic angle of 54.7° relative to the axis of the electron analyzer. The MgKα emission line (1253.6 eV) was used for XPS data acquisition. Given the highly disordered nature of the nanospring samples (randomly oriented nanosprings and a mat thickness of ~ 60 μm), in conjunction with the specifications of the X-ray source and electron analyzer, the upper resolution of the XPS spectra is estimated to no better than 300 meV based on the FWHM (full width at half maximum) of the Au $4f_{7/2}$ core level state. To avoid spurious charging the sample was grounded and exposed to an electron beam using an electron flood gun. The binding energy was referenced to the C 1s peak at 284.70 eV for catalyst samples and 285 eV for thiols functionalized samples. UPS spectra were acquired with the He I line (21.2 eV) from a Specs UVS 10/35 source, using ultrapure He (99.999%) that was passed through a liquid nitrogen cold trap to remove unwanted contaminants such as oxygen and nitrogen. The Fermi edge of a polycrystalline Au specimen was used for binding energy calibration. In both experiments the takeoff angle was 90°, corresponding to photoelectron emission normal to the sample surface. All spectra were acquired at room temperature. The fitting of the XPS spectra consisted of subtracting a Shirley background prior to peak fitting with Voigt functions.

2.3 Electrical and Chemical Characterization of Samples

2.3.1 Sensor Evaluation

A standard two-electrode geometry was used for measuring the electrical response of nanospring-based chemiresistors to exposure to chemical vapors. The electrical leads were attached to the nanospring-mat using a silver epoxy, where the epoxy was cured by placing the sensor on a hot plate at 125°C for 12 hours. The ohmic nature of the contacts was verified by linear nature of the current as a function of voltage, or I-V sweeps. The sensor was connected to a thermocouple and placed on a variable temperature platform for temperature control, as shown in Figure 2.11. The sensor response was acquired with a Keithley 2400 source-sense meter interfaced to a computer via Labview operated data acquisition software allowing for real time conductance measurements. A continuous flow of synthetic air (20% O_2 and 80% N_2) on the sensor was maintained at all times. The sensor was initially heated to the desired temperature. When a steady state resistance was obtained, pulses of vapor were introduced in the air flow by the VaporJet calibrator,[22] shown in Figure 2.13(b, c). Liquid analytes were evaporated while solid ones were sublimated. The VaporJet's ability to sublimate solids almost instantly allows for extremely short pulses on the order of milliseconds.[22]

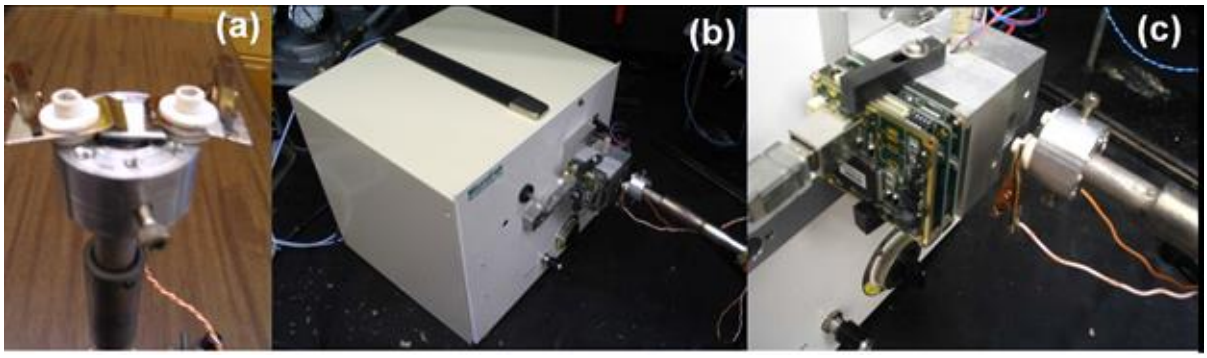

Figure 2.13 Photograph of the sensing experimental setup: (a) The sensor holder, (b) The sensor holder in front of the output of the VaporJet, and (c) a close up of the sensor holder in front of the VaporJet.

2.3.2 Catalyst Evaluation

The catalytic performance of Fischer-Tropsch catalysts were evaluated in a quartz tube (10x300 mm^2), fixed-bed microreactor (Figure 2.14). The reactor was heated using a small tube furnace (Supelco) and the temperature controlled with a PID controller. Reactant gases (CO and H_2) and inert gas (N_2) were introduced from the top of the reactor, and their flow rates metered with digital mass flow controllers. Prior to the reaction, the catalysts were reduced *in situ* at 400°C for 12h in a flow of H_2. After reduction, the reactor was operated at 230°C with a syngas flow rate of 60 mL min^{-1} (H_2/CO = 2) and N_2 used as internal standard. Products were collected every 10h in a three-stage impinger trap placed in a liquid nitrogen bath. The uncondensed vapor stream was collected in a Tedlar^{TM} PVF (300x300 mm^2) gas sampling bag. Condensed liquid products were analyzed by gas chromatography-mass spectrometry (GC-MS, Focus-ISQ, Thermoscientific). Separation was achieved on a RTx-5ms (30 mx0.25 mm) with a temperature program of 40 to 250°C at 5°C min^{-1}. 1,2,4-Trichlorobenzene was used as internal standard. Compounds were identified by their mass spectra, library mass spectral matching (NIST 2008) and retention times of known standard

n-alkanes. Gaseous products taken from the sampling bag with a syringe were analyzed by gas chromatography-thermal conductivity detector (GC-TCD, GOWMAC, Series 350) equipped with a Haysep DB stainless steel packed column (9.1mx 3mm). Standard curve was prepared from individual gas (i.e. N_2, CO, CO_2, and CH_4) for quantification. Catalytic activity, product selectivity, and stability of the catalysts were monitored during a period of 120h. FTS activity is reported as CO conversion rate (g CO/g Cat./h), and water-gas-shift (WGS) reported as CO_2 formation rate (g CO_2/g Cat./h).

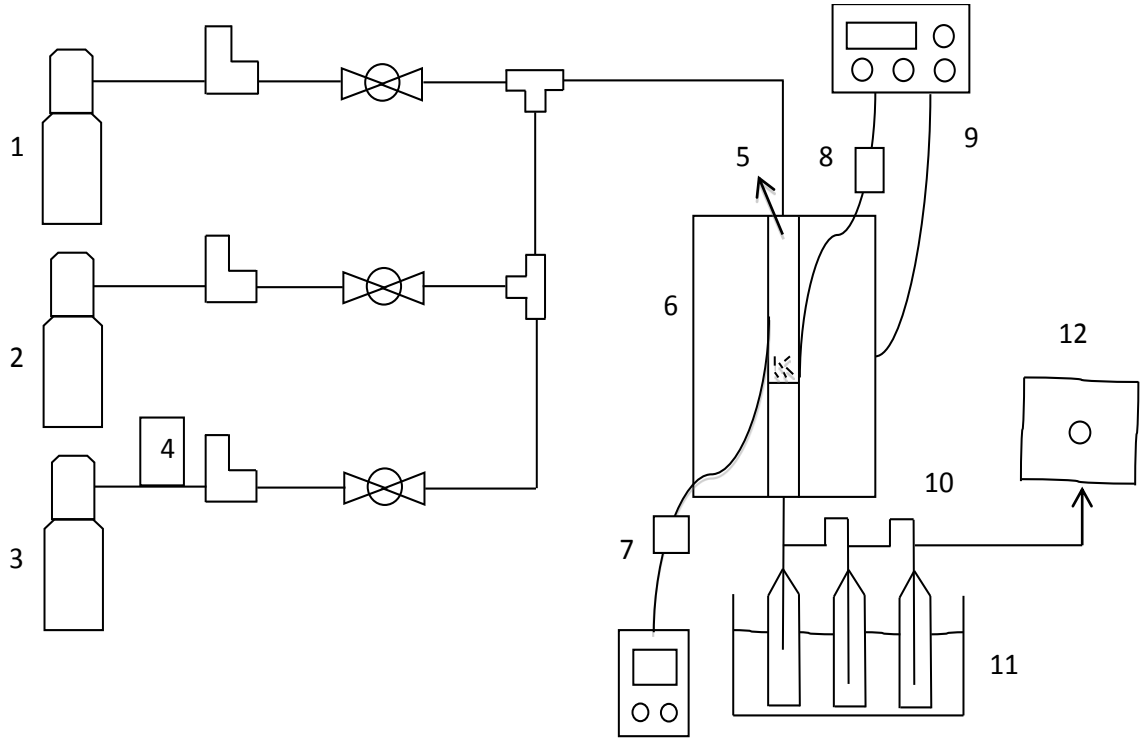

Figure 2.14 Schematic diagram of FTS reactor. (1) CO cylinder; (2) H_2 cylinder; (3) N_2 cylinder; (4) mass flow controllers; (5) quartz tubular reactor; (6) furnace; (7) K-type thermocouple; (8) J-type thermocouple; (9) temperature controller; (10) 3 sample collection impingers in series; (11) liquid N_2 bath; and (12) gas sampling bag.

References

(1) McIlroy, D. N. *et al.* Nanospring formation—unexpected catalyst mediated growth. *J. Phys. Condens. Matter* **16,** R415–R440 (2004).

(2) Wang, L. *et al.* High yield synthesis and lithography of silica-based nanospring mats. *Nanotechnology* **17,** S298–S303 (2006).

(3) Elam, J. W., Groner, M. D. & George, S. M. Viscous flow reactor with quartz crystal microbalance for thin film growth by atomic layer deposition. *Rev. Sci. Instrum.* **73,** 2981 (2002).

(4) George, S. M., Ott, A. W. & Klaus, J. W. Surface Chemistry for Atomic Layer Growth. *J. Phys. Chem.* **100,** 13121–13131 (1996).

(5) Elam, J. W. & George, S. M. Growth of ZnO/Al_2O_3 Alloy Films Using Atomic Layer Deposition Techniques. *Chem. Mater.* **15,** 1020–1028 (2003).

(6) Guziewicz, E. *et al.* ZnO by ALD — Advantages of the Material Grown at Low Temperature. *Acta Phys. Pol. A* **116,** 814 (2009).

(7) Przezdziecka, E. *et al.* Characterization of ZnO Films Grown at Low Temperature. *Acta Phys. Pol. A* **114,** 1303 (2008).

(8) Guziewicz, E. *et al.* Extremely low temperature growth of ZnO by atomic layer deposition. *J. Appl. Phys.* **103,** 033515 (2008).

(9) Brunauer, S., Emmett, P. H. & Teller, E. Adsorption of Gases in Multimolecular Layers. *J. Am. Chem. Soc.* **60,** 309–319 (1938).

(10) Leofanti, G., Padovan, M., Tozzola, G. & Venturelli, B. Surface area and pore texture of catalysts. *Catal. Today* **41,** 207–219 (1998).

(11) Barrett, E. P., Joyner, L. G. & Halenda, P. P. The Determination of Pore Volume and Area Distributions in Porous Substances. I. Computations from Nitrogen Isotherms. *J. Am. Chem. Soc.* **73,** 373–380 (1951).

(12) Storck, S., Bretinger, H. & Maier, W. F. Characterization of micro- and mesoporous solids by physisorption methods and pore-size analysis. *Appl. Catal. Gen.* **174,** 137–146 (1998).

(13) Siegbahn, K. *et al.* ESCA, Atomic, Molecular and Solid State Structure Studied by Means of Electron spectroscopy. *Nova Acta Regiae Soc. Sci. Ups.* **20,** (1967).

(14) Siegbahn, K. *et al.* ESCA-Aplied to Free Molecules. *N.-Holl. Amst.* (1969).

(15) Cardona, M. & Ley, L. *Photoemission in solids: General principles*. (Springer-Verlag, 1978).

(16) *Practical surface analysis: by auger and x-ray photoelectron spectroscopy*. (Wiley, 1983).

(17) Demuth, J. & Eastman, D. Photoemission Observations of π-d Bonding and Surface Reactions of Adsorbed Hydrocarbons on Ni(111). *Phys. Rev. Lett.* **32,** 1123–1127 (1974).

(18) Seah, M. P. & Dench, W. A. Quantitative electron spectroscopy of surfaces: A standard data base for electron inelastic mean free paths in solids. *Surf. Interface Anal.* **1,** 2–11 (1979).

(19) Ertl, G. *Low energy electrons and surface chemistry*. (VCH, 1985).

(20) Shirley, D. High-Resolution X-Ray Photoemission Spectrum of the Valence Bands of Gold. *Phys. Rev. B* **5,** 4709–4714 (1972).

(21) Tougaard, S. & Sigmund, P. Influence of elastic and inelastic scattering on energy spectra of electrons emitted from solids. *Phys. Rev. B* **25,** 4452–4466 (1982).

(22) Antohe, B. V. *et al.* Portable vapor generator for the calibration and test of explosive detectors. in 114–120 (IEEE, 2009). doi:10.1109/THS.2009.5168023

CHAPTER 3
Electronic Structure of Metal-ZnO Coated Nanosprings

3.1 Introduction

Nanotechnology as a cross-disciplinary field has led to the fabrication of several novel materials for a wide range of applications. Nanoparticles have proved their effectiveness for drug delivery in cancer as they enhance the intracellular concentration of drugs, reduce or overcome the drug resistance.[1] The utilization of semiconductor nanocrystalline in photocatalysis is a very attractive route for the purification of air and water.[2] The use of DNA-based nanowires as interconnects in nanoscale integrated circuitry offers a promising alternative to optical lithography for the miniaturization of features.[3] Overall chemical and biological sensing appear to be the most important applications of nanomaterials as they are used to detect toxic and explosive gases or proteins.[4,5] Furthermore, hybrid or hierarchical type nanostructures are being considered to take advantage of the cooperative or collective properties not attainable with a single component. The properties of nanomaterials can vary from one growth method to another or with the experimental conditions within the same growth technique. Characterization therefore, is a crucial step where those properties are assessed. Characterization provides not only a feedback on the growth procedure but more importantly an insight for the potential application. While no single technique can fully characterize a material, electronic structure via photoemission is suitable for materials whose behavior is governed by the surface properties.

The motivation behind the synthesis of nanostructures studied herein is the development of a sensitive solid state device for detection of explosive materials. Because of their insulating nature nanosprings interact poorly with gases. Nevertheless, their very flexible surface

chemistry and their large surface area (in the range of 350-400 m^2/g) make them attractive scaffoldings upon which sensitive layers can be built. Metal-semiconductor composites constitute a very good choice for this purpose as Schottky contacts, which are surface barriers, are readily created. With these coatings, the sensor response corresponds to the modulation of the surface barrier height when the sensor interacts with analytes from the surrounding atmosphere. ZnO was chosen for being the most widely applied metal-oxide semiconductor sensing material besides its prospective applications in light emitters, solar cells, piezoelectric transducers and acoustic wave devices.[6-7] . For the metal nanoparticles, their selection was based on their known catalytic activity. There have been several growth methods for the synthesis of ZnO thin films: sol-gel method,[8] sputtering,[9] metalorganic chemical vapor deposition (MOCVD) [10] or atomic layer deposition (ALD).[11] Metal-ZnO composites have been obtained from wet chemical precipitation-deposition,[12] electrochemically,[13] hydrothermally,[14] via thermal evaporation and sputtering or combined thermal evaporation and sputtering, and photoreduction.[15]

In this chapter we report the electronic structures of silica nanospring-mats coated with a thin layer of ZnO produced by ALD technique and subsequently decorated with differing metal nanoparticles such as Ag, Au, Ni, Pd, and Pt. The responses of these chemiresistrors to vapors of toluene, which is a degradation product of the powerful explosive TNT (trinitro-toluene) are also presented and discussed.

3.2 Results and Discussion

3.2.1 X-ray Photoelectron Spectroscopy (XPS)

The elemental composition of the surface region of the samples was investigated. For this purpose, survey scans were recorded (not shown). Spectra from ZnO coated samples exhibited signals from Zn, O, and adventitious C. Samples that were subsequently decorated with Ag, Au, Ni, Pd, and Pt showed additional signals from these metals. Signals from Si were not detected, indicating that the silica was completely buried under the coatings.

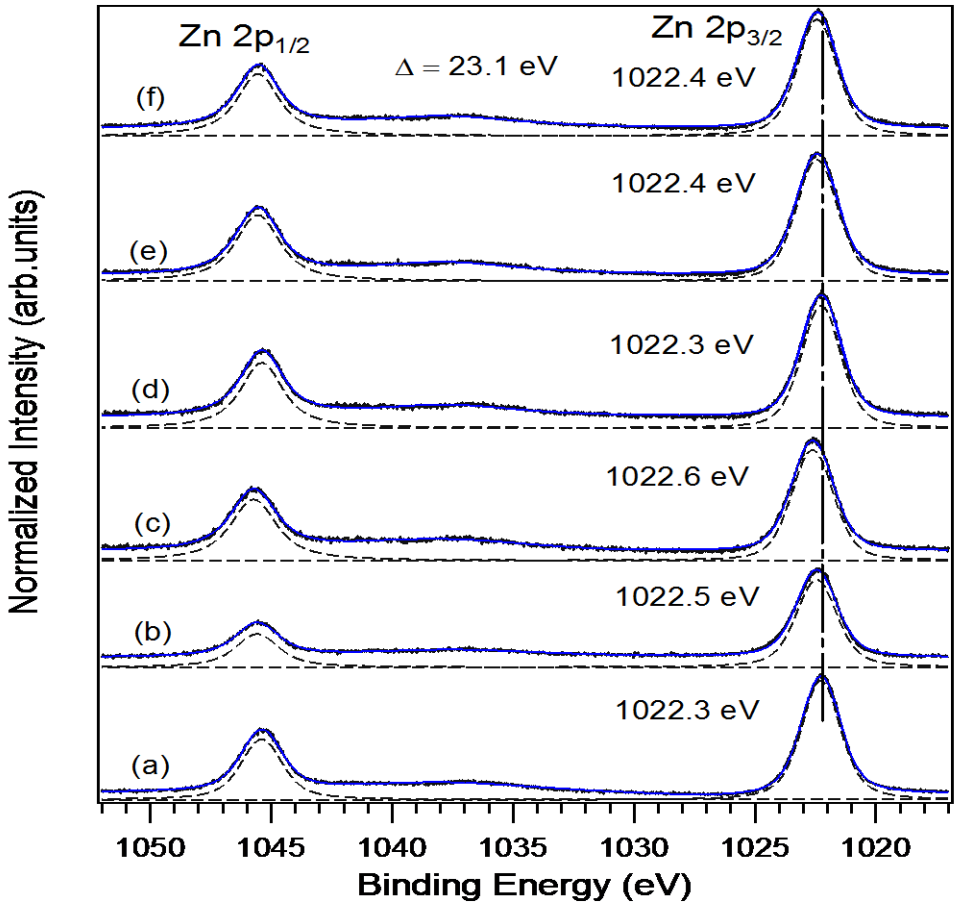

Figure 3.1 The Zn 2p core level states from (a) ZnO, (b) Ag/ZnO, (c) Au/ZnO, (d) Ni/ZnO, (e) Pd/ZnO, and (f) Pt/ZnO nanospring samples.

To determine the oxidation states of the detected elements, high resolution scans were taken for individual core level states. The Zn 2p core levels are shown in Figure 3.1. The peaks at ~1022.5 eV and 1045.6 eV are emission from Zn $2p_{3/2}$ and Zn $2p_{1/2}$ states, respectively. The spin-orbit splitting is 23.1 eV and a plasmon feature appears around 1037 eV. The peak position for Zn $2p_{3/2}$ agrees well with the reported binding energy from the wurtzite ZnO phase reported at 1022.4 eV.[6] No metallic zinc at 1021.5 eV was observed, indicating that all the Zn atoms are in the Zn^{2+} state.[16] Upon metallization, except for Ni/ZnO sample, the peak shifted to higher binding energy by 0.1-0.3 eV, which reflects the similar electronegativity (1.4) of the metals.

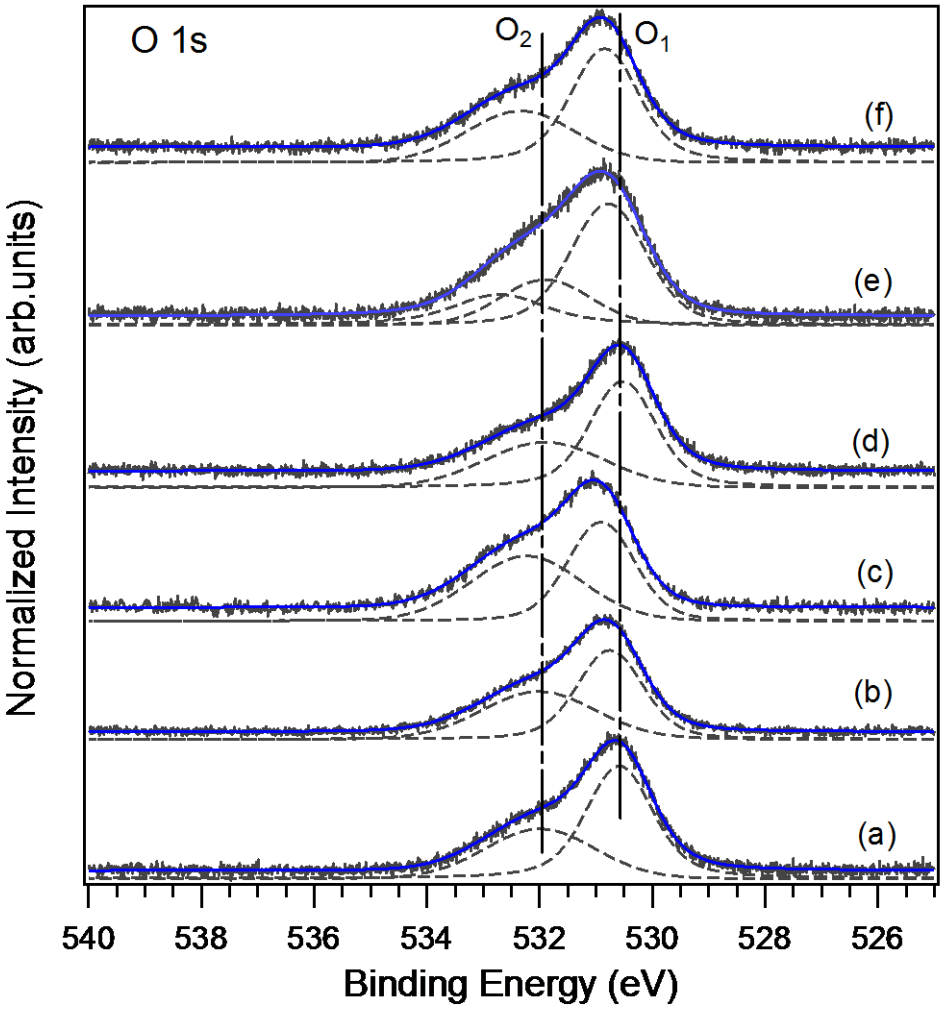

Figure 3.2 The O 1s core level states from (a) ZnO, (b) Ag/ZnO, (c) Au/ZnO, (d) Ni/ZnO, (e) Pd/ZnO, and (f) Pt/ZnO nanospring samples.

For the O 1s core level states (Figure 3.2), the asymmetry of the peaks suggests at least two kinds of oxygen species in the surface of the samples. As reported in the literature, the peak at ~531.0 eV (O_1) is due to the lattice oxygen in ZnO, which is the O^{2-} state.[16] There are three possible candidates for the peak at ~532.6 eV (O_2): the subsurface oxygen, the carbonates and the oxygen of surface hydroxyls. Neither Si nor carbonates C 1s signals were detected, which ruled out the first two possibilities. The component was therefore ascribed to hydroxyl groups [6,17] which play a very important role in the sensing ability of ZnO. The spectrum for Pd/ZnO sample was deconvolved into three components, the third component being the photoemission from the Pd $3p_{3/2}$ core level which overlaps with the hydroxyl component. Comparing the ratio O_1 to O_2 showed that the concentration of surface hydroxyls was fairly constant with Au decoration, while it was reduced for the other four metal coatings. The reduction was greater for Pd and Pt decorated samples which were annealed at higher temperature (500ºC). The reduced concentration might stem from the lability of the OH group which either desorbs or undergoes an acid-base reaction to form water, also removed during H_2 thermal reduction of the samples.

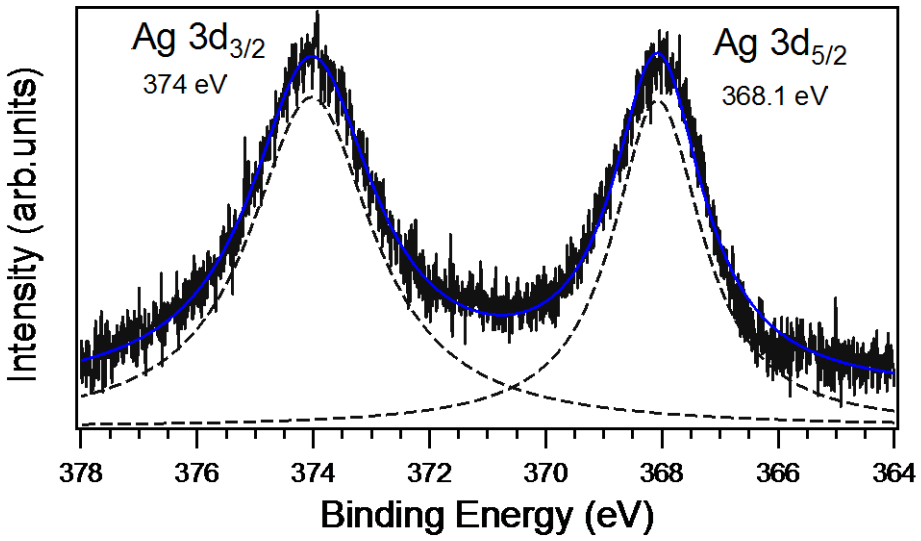

Figure 3.3 The Ag 3d core level states from Ag/ZnO nanospring sample.

For the Ag/ZnO sample, the peaks observed at 368.1 eV and 374.0 eV (Figure 3.3) correspond to direct photoemission from Ag $3d_{5/2}$ and Ag $3d_{3/2}$ core level states of metallic silver, respectively. The shift to lower binding energy compared to the bulk (368.3 eV and 374.3 eV) is indicative of partial oxidation as Ag and ZnO align their Fermi levels to the same value.[18] Though Ag_2O was detected by XRD (data not shown), with XPS there was no peak at 367.8 eV and 367.4 eV corresponding to Ag_2O and AgO, respectively. It was therefore concluded that Ag_2O crystallites detected by XRD, which is a bulk characterization technique, are sandwiched between Ag and ZnO crystallites, well below the photoelectron escape depth for XPS.

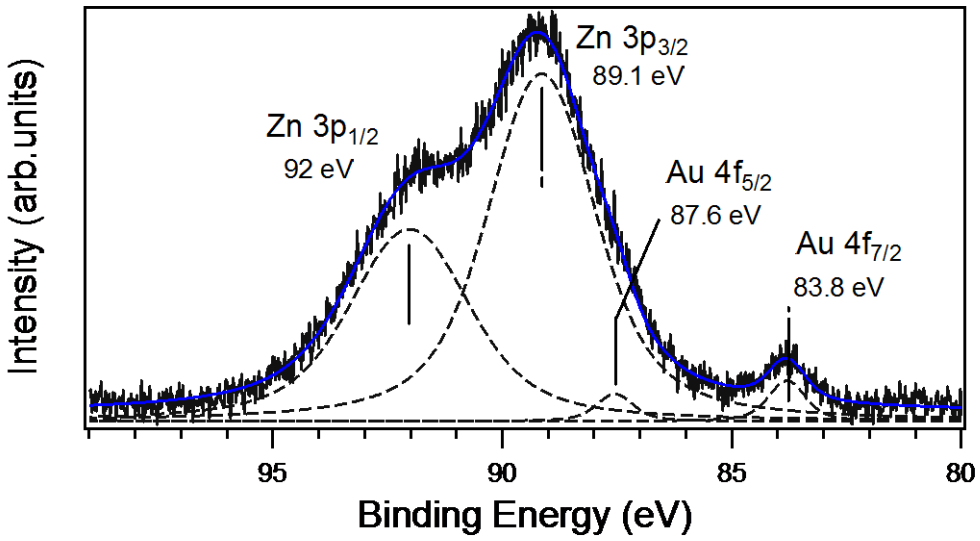

Figure 3.4 The Au 4f-Zn 3p core level states from Au/ZnO nanospring sample.

The Au $4f_{5/2}$ was overlapped by the signal of Zn 3p as shown in Figure 3.4. The binding energy of 83.8 eV for Au $4f_{7/2}$ is slightly shifted to lower value compared with typical value of 84.0 eV. Since the binding energy of Au (δ^+) always shifts to greater value,[19] it was concluded that nanoparticles should be in the metallic state Au (0). The peak shift is tentatively attributed to electron donation from the conduction band of ZnO under X-ray irradiation in the XPS experiment.[20] Yonlan et al. [20] had reported a shift of Au $4f_{7/2}$ to 82.85 eV for their Au/ZnO nanocomposites, and Tada et al. [21] XPS peaks at 83.2 eV in Au/TiO_2 catalysts.

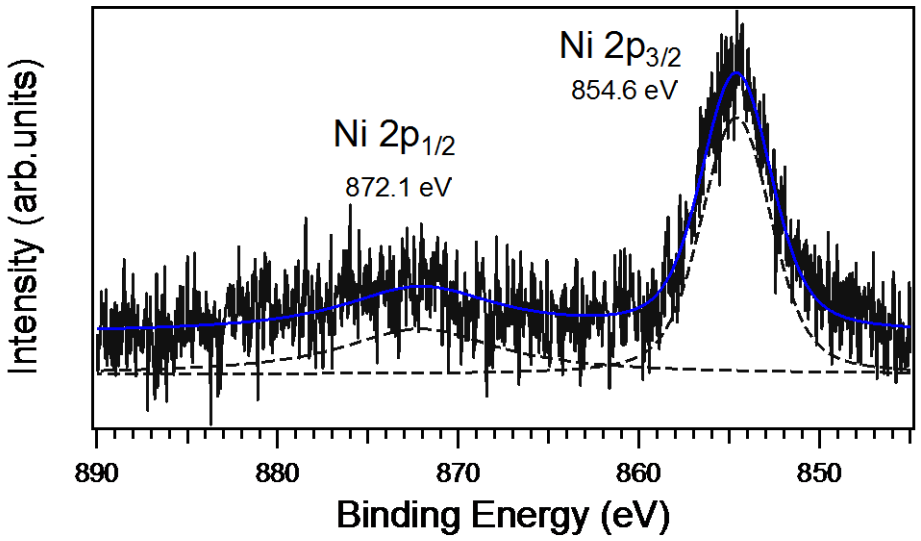

Figure 3.5 The Ni 2p core level states from Ni/ZnO nanospring sample.

The binding energy position of Ni $2p_{1/2}$ and Ni $2p_{3/2}$ are 854.6 eV and 872.1 eV, respectively. These values are close to the reported values of Ni in NiO, and do not match those of metallic Ni and Ni_2O_3.[22] Since there is no shake-up satellite peak on the side of higher binding energy, characteristic of NiO, it can be safely concluded that Ni atoms are in an intermediate oxidation state between 0 and 2+.

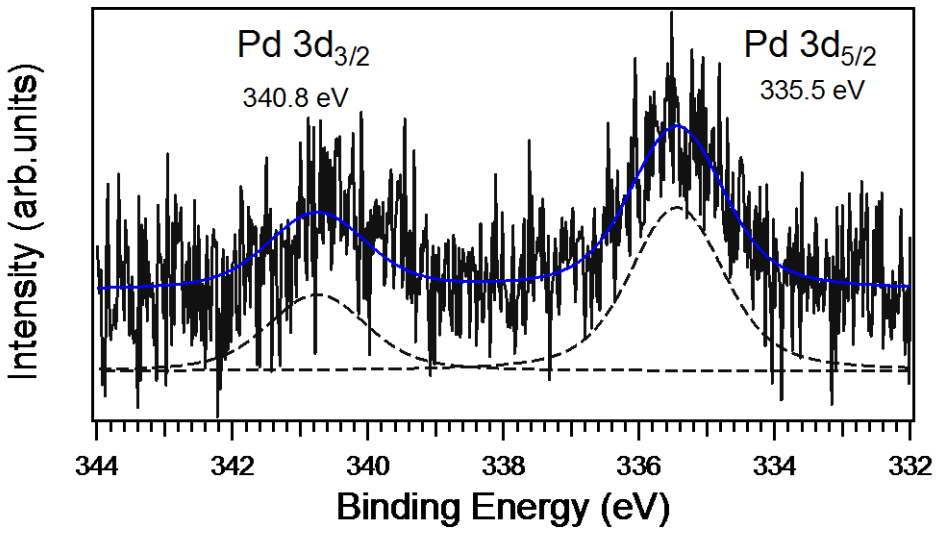

Figure 3.6 The Pd 3d core level states from Pd/ZnO nanospring sample.

The spectrum of Pd 3d (Figure 3.6) is not smooth, which may be attributed to the little content of Pd in the samples. The peaks locate at 335.5 eV and 340.8 eV correspond to photoemission from Pd $3d_{5/2}$ and Pd $3d_{3/2}$, respectively. These binding energies though shifted to slightly greater values compared to the bulk (335.2 eV and 340.5 eV), are in good agreement with those reported by Yunyan et al.[23] for their Pd/ZnO nanocomposites.

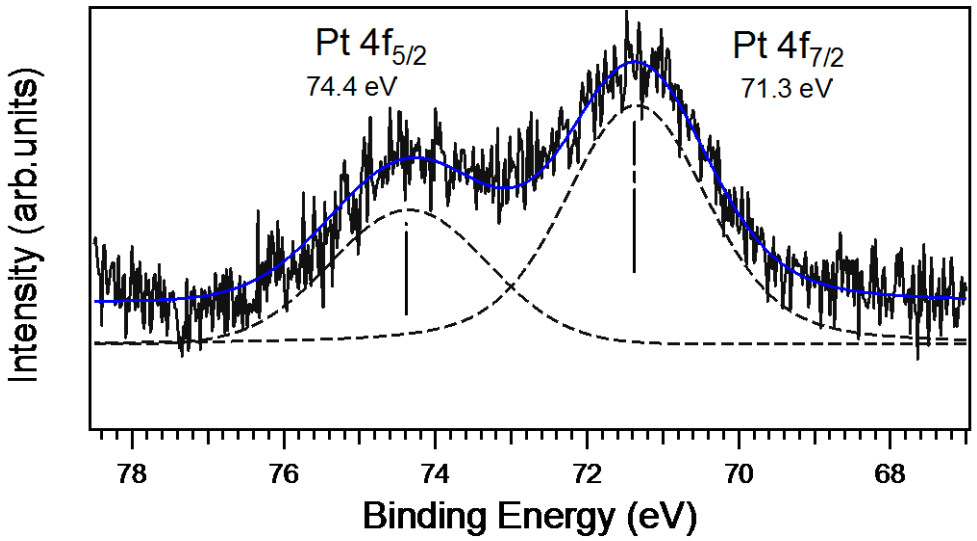

Figure 3.7 The Pd 4f core level states from Pt/ZnO nanospring sample.

The peaks position of Pt $4f_{7/2}$ and Pt $4f_{5/2}$ are 71.3 eV and 74.4 eV, respectively (Figure 3.7), which closely matches with the reported values of Pt.[22] This indicates that all the Pt atoms are in the metallic state. The negative binding energy shift which translates to strong metal-support interaction was not observed.

3.2.2 Ultraviolet Photoelectron Spectroscopy (UPS)

UPS valence bands spectra of the samples are displayed in Figure 3.8. Also shown (right panel) are linear extrapolations of the low binding energy edge to the background to obtain the valence band maximum (VBM) positions, while in the left panel are the work functions, each next to the energy cutoff that was used for the determination.

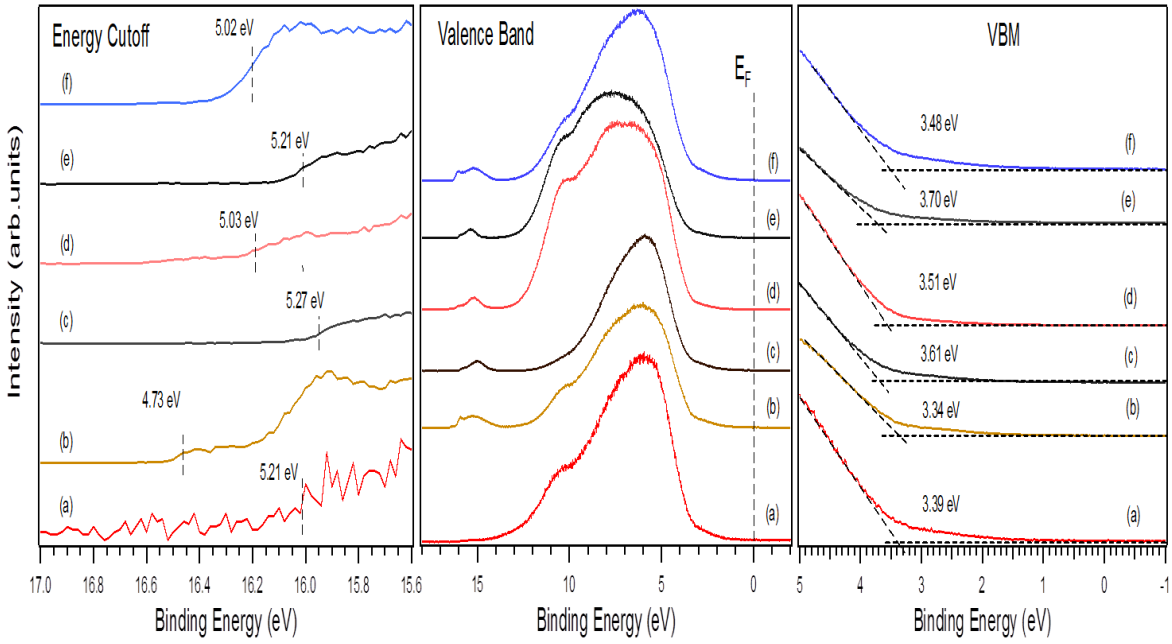

Figure 3.8 The UPS (He I) valence bands spectra for (a) ZnO, (b) Ag/ZnO, (c) Au/ZnO, (d) Ni/ZnO, (e) Pd/ZnO, and (f) Pt/ZnO nanospring samples. (Left Panel) Energy cutoffs, (Right panel) Valence band maximum (VBM) obtained by linear extrapolations.

The valence band of ZnO extends from 3 to 8 eV; theory predicts that emission from 3-5 eV corresponds to non-bonding O 2p orbitals, and that from 5 to 8 eV is a bonding combination of O 2p and Zn 4s orbitals. In spite of the proximity of the Zn 3d core levels to the valence band, which corresponds to the weak shoulder around ~10 eV, the O 2p and Zn 4s orbitals are significantly hybridized.[24] For the decorated samples, one would expect some changes in the spectrum. For example, a sharp cutoff of the partially filled d-band of metals such as Ni and Pt at the Fermi energy, or an increased density of states at E_F for Pd, Ni and Pt.[25] The valence bands are still dominated by ZnO features because of the very low content of the metals. The d shell forms a broad band between 4-8 eV for the Ag 4d, 2-8 eV for the Au 5d, 0-5 eV for Pd, 0-8 eV for Pt, and 0-6 eV for Ni. These superimpositions result in the broadening of the band features as observed. There are nevertheless obvious changes as

demonstrated by the positions of the VBM or the work functions. The measured work functions are in good agreement with values reported in the literature.[26] The schematic energy band diagrams as extracted from the UPS data are shown in Figure 3.9. In each case, the band bending parameter $\zeta = E_v - E_{F,}$ is the distance between the valence band maximum (E_v) and the Fermi level (E_F).

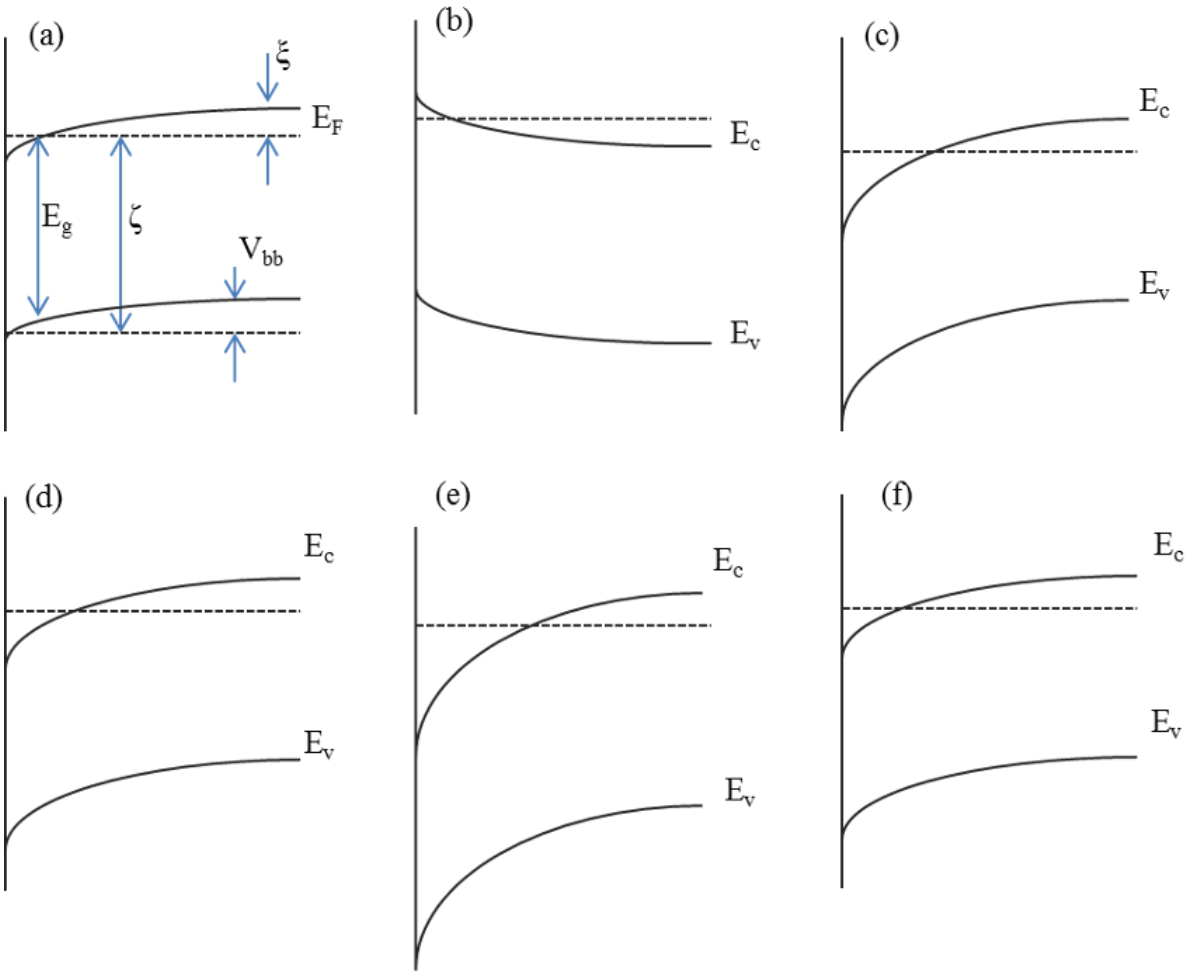

Figure 3.9 Band bending schematic diagrams of (a) ZnO, (b) Ag/ZnO, (c) Au/ZnO, (d) Ni/ZnO, (e) Pd/ZnO, and (f) Pt/ZnO nanospring samples.

The near-surface band bending (V_{bb}) was obtained from $V_{bb} = E_g - \zeta - \xi$, where E_g is the energy band gap (3.3 eV), $\xi = (k_B T/q)\ln(N_c/n)$ is the energy difference between the conduction band minimum E_C (n is the intrinsic carrier concentration and N_C the effective density of states of the conduction band). The values used for n and N_C are 2.0×10^{19} cm^{-3} and 3.7×10^{18} cm^{-3}, respectively.[27] Negative values of V_{bb} correspond to downward surface band bending and electron accumulation, while positive values are associated with upward band bending and the presence of a surface depletion region.[28] As shown in Figure 3.9, an accumulation layer is readily formed on the surface of ZnO, and apart from the Ag/ZnO sample where there is a depletion layer, the accumulation layer increases upon decoration with the other four metals in the order Pt<Ni<Au<Pd. Starting with the bare ZnO, the dominant surface defects are O vacancies. When those point defects are created, the electronic charges donated to the surface upon removal of surface O^{2-} ions results in an accumulation layer and an increase in the surface conductivity. It is this accumulation layer that is affected by chemisorbed atoms, with the resulting changes in surface conductivity that make ZnO an important material for gas sensors.[24] The downward band bending could be formed by a high concentration of surface O vacancies, leaving an excess of electrons in the surface region. On the other hand, a depletion layer, which may occur if the surface were covered with adsorbed oxygen (as O_2^- or O^-), produces and upward bending of the bands. The band bending in each case is cause by an unequal concentration of (positive) ionized impurity centers and (negative) electrons in the space-charge region. The metal and semiconductor work function difference plays an important role in the Fermi level pinning which in turn determines the nature of the contact.

Consider ZnO (n type semiconductor) with a work function of 5. 2 eV, when brought into contact with a low-work function metal like Pt (5.1 eV), electrons begin moving from Pt to ZnO. The net transfer of electrons from the metal to the semiconductor leaves a net excess of electrons at the surface (accumulation layer). The process continues until the Fermi levels are aligned. The energy bands of ZnO bent downwards near the contact (initial state). The magnitude of the band bending and its extension into the semiconductor are very small. As a result there is virtually no potential barrier between the metal and the semiconductor and the electrons can flow freely through the contact, such a contact is ohmic. The surface band bendings as obtained for nanospring samples (Fig. 3.9) are consistent with those of low work function metal on n-type semiconductor,[29] except for Ag/ZnO. The rectifying behavior would normally indicate a high-work function metal on an n type semiconductor. However, given the low work function of Ag (4.7 eV), the nonlinear behavior may be, instead, due to the Ag_2O layer sandwiched between Ag and the ZnO substrate as pointed out earlier (see section 3.2.1), where the p type conductivity of Ag_2O comes into play.

Heinhold et al.[28] show that annealing ZnO to 750℃ changes irreversibly the downward band bending to upward band bending. Therefore, annealing the nanospring samples as it is done during the sensing measurements would make all the contacts rectifying.

3.2.3 Chemiresistor Response

The sensors were found to operate between 100ºC and 500ºC. The lack of sensitivity below 100ºC is due to significant drop in the surface O vacancies. The reduction of sensitivity above 500ºC is caused by activation of surface phonons, resulting in a significant increase in oxygen desorption rate. Sensors responses to vapors of toluene are displayed in Figure 3.10. For Au/ZnO and Ni/ZnO sensors the three peaks correspond to responses to 100, 130, and

160 ppm vapors of toluene. The vapor pressure of toluene was 500 ppm for the rest of the sensors. The ZnO nanocrystal size in the samples was ~20 nm. For the pristine ZnO the resistance changes from few kΩ to few MΩ. This is an opposite behavior to that of bulk ZnO. Heating bulk ZnO excites free carriers, producing a drop in resistance.[29] However, for ZnO-coated nanosprings two competing processes interplay: thermal generation of free carriers (decreases the resistance) and trapping of free electrons by ionized oxygen at the surface (increases the resistance). At elevated temperatures, the depletion layer caused by adsorbed oxygen dominates, resulting in a thinner conducting layer.[26] When thermally activated ZnO is exposed to air, oxygen molecules chemisorbed onto its surface and form oxygen ions (O^-) by capturing electrons from the conduction band. As ZnO is exposed to a reducing gas like toluene, the redox reaction taking place strips the O^- species from the surface of ZnO. The trapped electrons are released back to the bulk, resulting in an increase in the conductance of ZnO.[26] Each peak in conductance as seen in Figure 3.10, correspond to release and capture of electrons by oxidation of toluene and re-oxidation of ZnO surface. During this interaction the surface band bending is modulated. It can be seen that the response (signal) became less noisy with particles decoration. All the sensors self-refreshed upon discontinuing exposures to vapors of toluene and returned to their baselines. The sensors' response was found to be ZnO grain size dependent. The lower and upper bounds were 3 and 20nm, with changes in conductance by factors of 50 and 100, respectively.

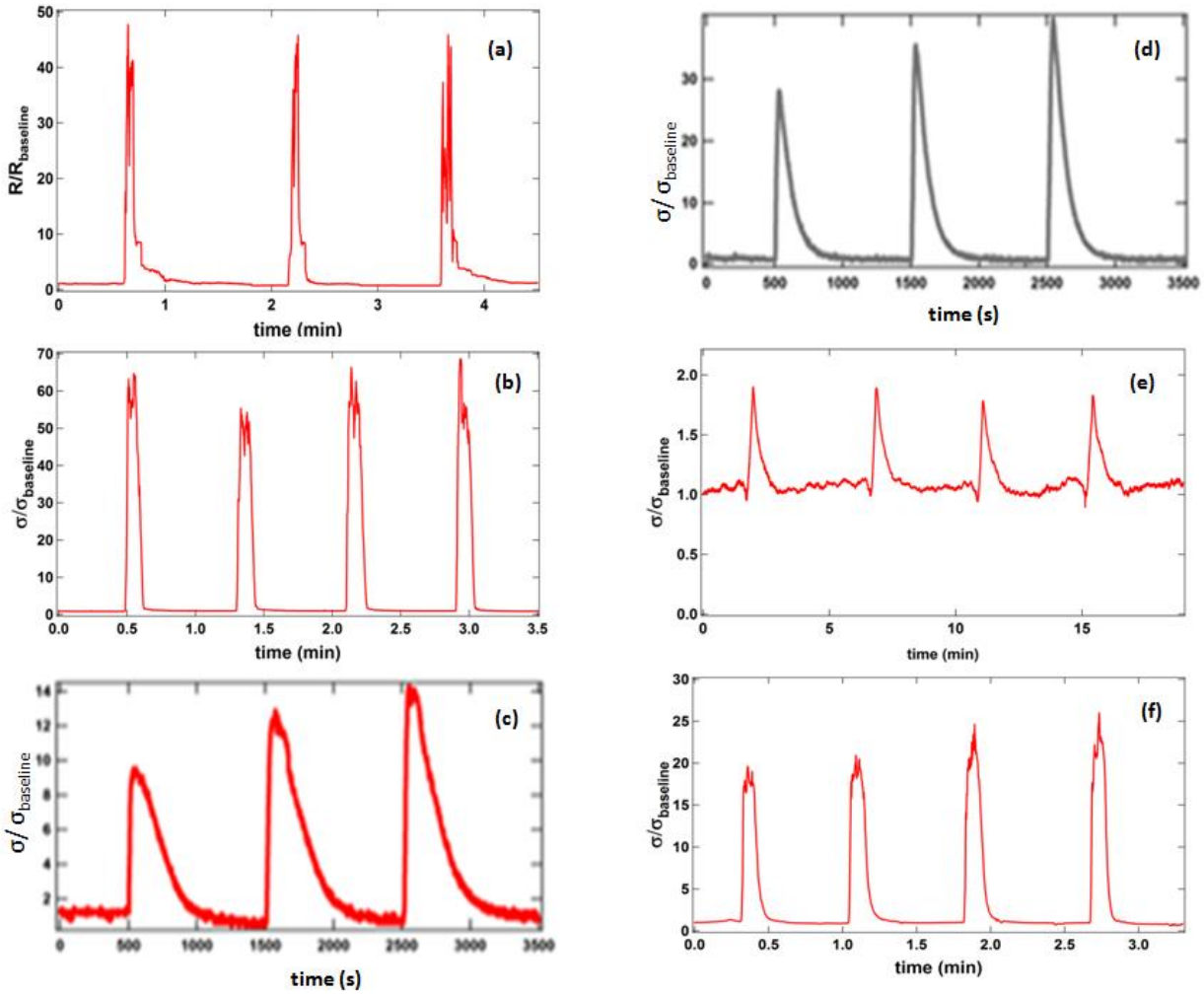

Figure 3.10 Relative changes in resistance or conductance of thermally activated (a) ZnO, (b) Ag/ZnO, (c) Au/ZnO, (d) Ni/ZnO, (e) Pd/ZnO, and (f) Pt/ZnO nanospring sensors upon exposure to vapor of toluene.

The best response was achieved with ZnO nanocrystals of average size of 15 nm, with an enhancement factor of 1000 (Figure 3.11).

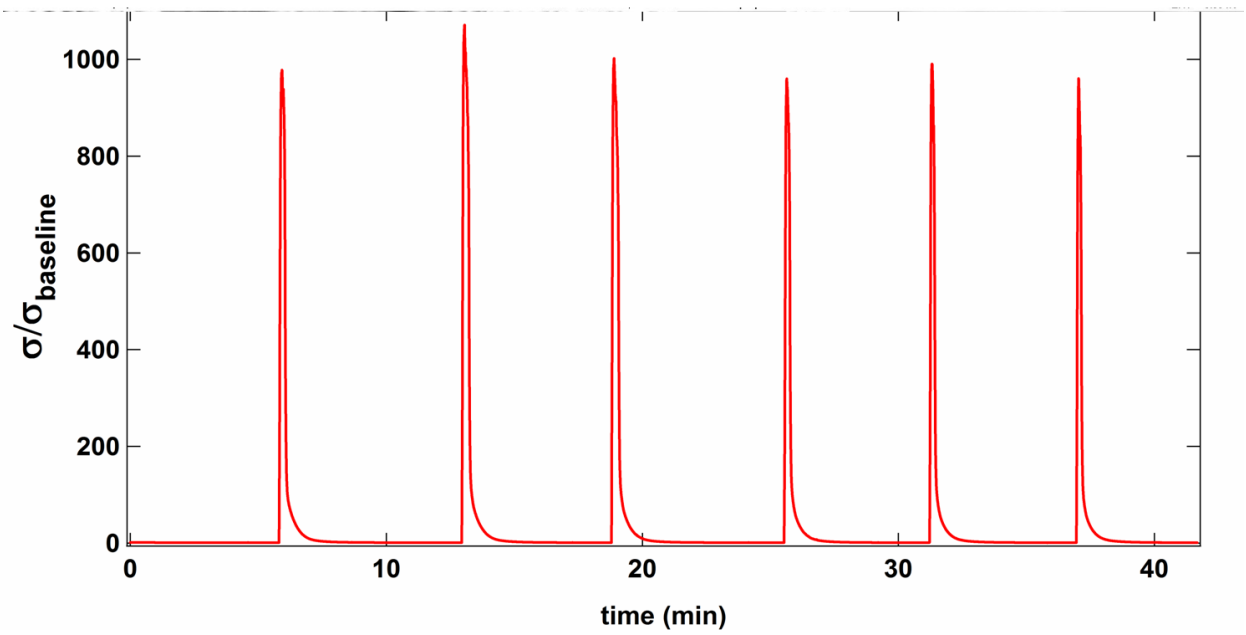

Figure 3.11 Relative changes in conductance of 15 nm-grain ZnO-coated nanosprings.

The size dependency of the chemiresistors response is closely related to the adsorption of oxygen and the availability of free electrons in the grain. The amount of adsorbed oxygen decreases as the grain area shrinks, and very small grains do not have as many free electrons available for "trapping" as the optimal size grains do. Moreover, given the low UV photocurrent of the 3nm-grain relative to the significant value of the 15nm-grain, the size dependency of the response may be attributed to finite size effects. These effects were modeled by Brus,[30] where the size dependency of the band gap of a semiconductor nanoparticle is given by the following formula:

$$\Delta E = E_{g(nano)} - E_{g(bulk)} \approx \frac{h^2}{8R^2}\left[\frac{1}{m_e} + \frac{1}{m_h}\right] - \frac{1.8e^2}{\varepsilon R} \qquad (3.1)$$

, where ΔE is the shift with respect to the bulk band gap $E_{g(bulk)}$, R is the radius of the nanoparticles, m_e (m_h) is the effective of the electron (hole) and ε is the semiconductor dielectric constant. The first term is the quantum energy of localization, increasing as R^{-2} for both electron and hole. The second term is the Coulomb attraction energy, which increases as

R^{-1}. In the limit of large R, the value of $E_{g(nano)}$ approaches that of $E_{g(bulk)}$, hence the reduce sensitivity with 20 nm-grain and above. The observed lack of photoconductivity for ZnO nanocrystals with a radius of 3 nm or less is attributed to finite size induced band gap widening, consistent with finite size effects explained by equation (3.1). The addition of Pd nanoparticles onto ZnO-coated nanosprings of 15 nm grain size increased the change in conductance response to vapors of toluene from the factor of 1000 to 1500 (Figure 3.12), corresponding to an enhancement of 50%.

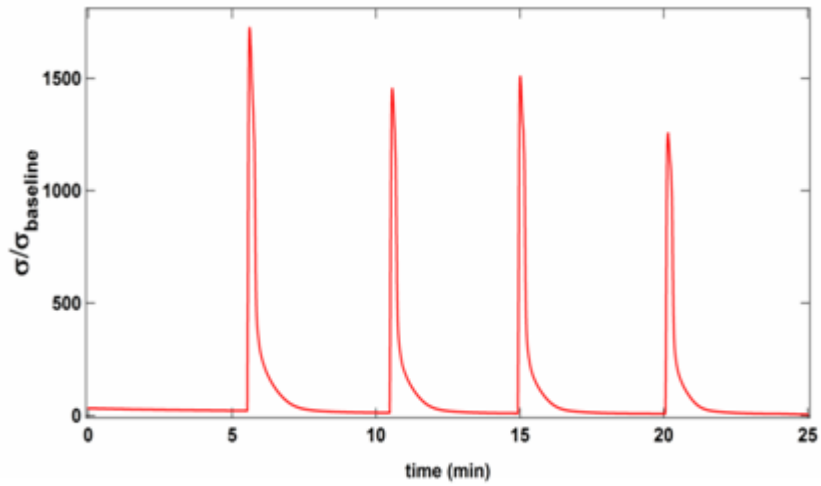

Figure 3.12 Relative changes in conductance of 15 nm-grain ZnO-coated nanosprings, subsequently decorated with Pd nanoparticles.

The improvement of the sensitivity with Pd decoration can be explained by two mechanisms. For the first mechanism, an external electrostatic potential is induced on the nanoparticles by adsorbed oxygen species. Exposure to vapors of analyte removes the oxygen and causes a drop in the induced electrostatic potential. This in turn, causes transfer of electrons from the nanoparticles to the ZnO. The system is equivalent to a field effect transistor (FET), where the nanoparticles is the gate and the adsorbed oxygen the source of the electrostatic potential.

The second mechanism is the so-called "spillover effect". The catalytic dissociation of molecular species at the surface of Pd nanoparticles followed by diffusion of the atomic species into ZnO produces higher density of O^-, which increase the rate of oxidation of vapors of toluene, hence the improved sensitivity.

3.3 Conclusion

In this chapter, we have investigated the electronic structure of nanosprings coated with ZnO and subsequently decorated with metal nanoparticles. The oxidation states of the elements present within the surface region of the samples were determined by XPS. Shifts were observed in the core levels binding energies of the metalized samples, which indicate charge redistribution as the metal and the ZnO substrate align their Fermi levels. UPS valence band spectra of the samples are dominated by ZnO features because of the low metal content. There is nevertheless a broadening of the bands, changes in the work function and the position of the valence band maximum upon metallization. The band structures as extracted from the UPS data showed surface band-bendings at the interface metal-ZnO associated with the formation of an accumulation layer or a depletion layer. Sensing tests showed that the samples are responsive to vapors of toluene and self-refreshable. The sensitivity is temperature and ZnO nanocrystals size dependent. The optimum operational temperature and grain size were found to be 400ºC and 15 nm, with change in the conductivity by a factor of 1000. Further decoration of the 15 nm–grain ZnO improved the sensitivity by 50%, making this hierarchical nanocomposite one of the most sensitive platforms for vapors detection. Chemiresistors in general can respond to several analytes. The next chapter will concentrate on the surface modification of nanospring-based chemiresistors to target specific analytes.

References

(1) Cho, K., Wang, X., Nie, S., Chen, Z. & Shin, D. M. Therapeutic Nanoparticles for Drug Delivery in Cancer. *Clin. Cancer Res.* **14,** 1310–1316 (2008).

(2) Mills, A. & Le Hunte, S. An overview of semiconductor photocatalysis. *J. Photochem. Photobiol. Chem.* **108,** 1–35 (1997).

(3) Stoltenberg, R. M. & Woolley, A. T. DNA-Templated Nanowire Fabrication. *Biomed. Microdevices* **6,** 105–111 (2004).

(4) Barreca, D. *et al.* 1D ZnO nano-assemblies by Plasma-CVD as chemical sensors for flammable and toxic gases. *Sens. Actuators B Chem.* **149,** 1–7 (2010).

(5) Singh, S. Sensors—An effective approach for the detection of explosives. *J. Hazard. Mater.* **144,** 15–28 (2007).

(6) Guziewicz, E. *et al.* ZnO by ALD — Advantages of the Material Grown at Low Temperature. *Acta Phys. Pol. A* **116,** 814 (2009).

(7) Xiang, Q. *et al.* Ag nanoparticle embedded-ZnO nanorods synthesized via a photochemical method and its gas-sensing properties. *Sens. Actuators B Chem.* **143,** 635–640 (2010).

(8) Huang, J.-S. & Lin, C.-F. Influences of ZnO sol-gel thin film characteristics on ZnO nanowire arrays prepared at low temperature using all solution-based processing. *J. Appl. Phys.* **103,** 014304 (2008).

(9) Furuta, M., Hiramatsu, T., Matsuda, T., Furuta, H. & Hirao, T. Effect of Energetic Particle Bombardment on Microstructure of Zinc Oxide Films Deposited by RF Magnetron Sputtering. *Jpn. J. Appl. Phys.* **46,** 4038–4041 (2007).

(10) Lin, H. *et al.* Structural and optical properties of a-plane ZnO thin films synthesized on γ-LiAlO2 (302) substrates by low pressure metal-organic chemical vapor deposition. *Thin Solid Films* **516,** 6079–6082 (2008).

(11) Guziewicz, E. *et al.* Extremely low temperature growth of ZnO by atomic layer deposition. *J. Appl. Phys.* **103,** 033515 (2008).

(12) Zheng, Y. *et al.* Photocatalytic Activity of Ag/ZnO Heterostructure Nanocatalyst: Correlation between Structure and Property. *J. Phys. Chem. C* **112,** 10773–10777 (2008).

(13) Mahamuni, S., Borgohain, K., Bendre, B. S., Leppert, V. J. & Risbud, S. H. Spectroscopic and structural characterization of electrochemically grown ZnO quantum dots. *J. Appl. Phys.* **85,** 2861 (1999).

(14) Zhang, Y. & Mu, J. One-pot synthesis, photoluminescence, and photocatalysis of Ag/ZnO composites. *J. Colloid Interface Sci.* **309,** 478–484 (2007).

(15) Tan, T. *et al.* Two-step preparation of Ag/tetrapod-like ZnO with photocatalytic activity by thermal evaporation and sputtering. *Mater. Chem. Phys.* **111,** 305–308 (2008).

(16) Chen, M. *et al.* X-ray photoelectron spectroscopy and auger electron spectroscopy studies of Al-doped ZnO films. *Appl. Surf. Sci.* **158,** 134–140 (2000).

(17) Coppa, B. J., Davis, R. F. & Nemanich, R. J. Gold Schottky contacts on oxygen plasma-treated, n-type ZnO(000$\bar{1}$). *Appl. Phys. Lett.* **82,** 400 (2003).

(18) Zheng, Y. *et al.* Ag/ZnO Heterostructure Nanocrystals: Synthesis, Characterization, and Photocatalysis. *Inorg. Chem.* **46,** 6980–6986 (2007).

(19) Boyd, D. *et al.* Reductive routes to stabilized nanogold and relation to catalysis by supported gold. *Appl. Catal. Gen.* **292,** 76–81 (2005).

(20) Luo, Y. ZnO microrods photodeposited with Au@Ag nanoparticles: Synthesis, characterization and application in SERS. *Colloid J.* **71,** 223–232 (2009).

(21) Tada, H. *et al.* Au-Core/Pt-Shell Bimetallic Cluster-Loaded TiO_2 . 1. Adsorption of Organosulfur Compound. *J. Phys. Chem. B* **106,** 8714–8720 (2002).

(22) Moulder, J. F., Stickle, W. F., Sobol, P. E. & Bomben, K. D. *Handbook of X-ray Photoelectron Spectroscopy*. (Perkin-Elmer Corporation, Physical Electronics Division, 1995).

(23) Zhang, Y., Wang, Q., Xu, J. & Ma, S. Synthesis of Pd/ZnO nanocomposites with high photocatalytic performance by a solvothermal method. *Appl. Surf. Sci.* **258,** 10104–10109 (2012).

(24) Henrich, V. E. & Cox, P. A. *The surface science of metal oxides*. (Cambridge University Press, 1994).

(25) McLachlan, A. D., Jenkin, J. G., Leckey, R. C. G. & Liesegang, J. A valence band study of Ag-Pd alloys using ultraviolet photoelectron spectroscopy. *J. Phys. F Met. Phys.* **5,** 2415–2424 (1975).

(26) Dobrokhotov, V. *et al.* Toward the nanospring-based artificial olfactory system for trace-detection of flammable and explosive vapors. *Sens. Actuators B Chem.* **168,** 138–148 (2012).

(27) Maragliano, C. *et al.* Quantifying charge carrier concentration in ZnO thin films by Scanning Kelvin Probe Microscopy. *Sci. Rep.* **4,** (2014).

(28) Heinhold, R., Williams, G. T., Cooil, S. P., Evans, D. A. & Allen, M. W. Influence of polarity and hydroxyl termination on the band bending at ZnO surfaces. *Phys. Rev. B* **88,** (2013).

(29) Lüth, H. *Solid surfaces, interfaces and thin films*. (Springer-Verlag, 2010).

(30) Dobrokhotov, V. *et al.* Thermal and Optical Activation Mechanisms of Nanospring-Based Chemiresistors. *Sensors* **12,** 5608–5622 (2012).

(31) Brus, L. E. Electron–electron and electron-hole interactions in small semiconductor crystallites: The size dependence of the lowest excited electronic state. *J. Chem. Phys.* **80,** 4403 (1984).

CHAPTER 4

Self-Assembled Monolayers of Thiols Adsorbed on Au/ZnO-Functionalized Silica Nanosprings: Photoelectron Spectroscopy Analysis and Detection of Vaporized Explosives

4.1 Introduction

Selectivity of surfaces to organics is a major thrust area in the field of interfacial science. Specifically, organic chemistry is being employed to tune organic/inorganic interface properties of materials used in nanoelectronics, chemical sensing, and passivation layers.[1] In fact, combining inorganic and organic materials into hybrid structures enables one to take advantage of new "collective effects" (i.e. phenomena that the individual components comprising the interface do not exhibit).[2] SAMs on metal nanoparticles or semiconductors surfaces are one approach to tailor these interfaces with close-packed molecules with a variety of headgroups, chain lengths and film thicknesses.[3] SAMs of thiols on the surface of gold nanoparticles are widely used for the following reasons. First, gold is a relatively inert metal: it does not form a stable oxide surface and it resists atmospheric contamination. Second, gold has a strong specific interaction with sulfur that allows the formation of monolayers with different functional groups. Third, when suitably selected, the SAMs films are coherent, densely packed, very stable, and crystalline or liquid-crystalline on gold.[4] Understanding, controlling and optimizing the properties of these molecular interfaces are keys to developing an efficient device for explosives detection.

The adsorption of thiols onto gold surfaces has been studied by many analytical methods including IR spectroscopy, optical ellipsometry, electron diffraction, wetting contact angle measurements, electrochemistry, and photoelectron spectroscopy.[4-6] These studies have shown that defect-free monolayers are spontaneously adsorbed at Au surfaces with a mean

tilt of 20-30°.[5] X-ray and ultraviolet photoelectron spectroscopies, XPS and UPS, respectively, are acutely sensitive to changes in surface morphology and surface functionalization due to their very shallow sampling depths on the order of 30Å. XPS is capable of giving direct and specific insight into the elemental composition, the oxidation states, and the chemical bonding of the elements within the surface region of the material. For example, Joseph et al.[6] analyzed the composition of alkanedithiols films assembled on gold nanoparticles and found that approximately 20 % of the adsorbed thiols were free groups, implying that only 60 % of the alkanedithiol molecules were bound at both ends to the nanoparticles. In terms of sensors, at room temperature the resistance of these films increased reversibly when dosed with vapors of toluene and tetrachloroethylene and the response increased exponentially with increasing length of the alkanethiols. The presence of unattached thiols within the film is important to deciphering the sensing properties of thiol-based sensors. The power of UPS is its ability to probe the valence band density of states. Furthermore, given the large photoionization cross sections of p-type orbitals in the UV regime, UPS is ideal for probing the highest valence bands of organic materials.[7] Specifically, UPS can be used to identify chemisorbed molecules on solid surfaces and the orbital bonding mechanisms responsible for chemisorption. Duwez et al.[7] have successfully used UPS to investigate molecular configurations and conformations of n-alkanethiols, α,ω-alkanedithiols, α-cycloalkyl-ω-alkanethiols adsorbed onto planar surfaces of gold. They found that for n greater than 16, where n is the number of carbon atoms in the hydrocarbon chain, the gold substrate does not disturb the spectral features of SAMs.

The uniqueness of the work reported herein lies in the nature of the substrate: silica nanospring-mats coated with ZnO and subsequently decorated with Au nanoparticles, which

besides being a non-planar surface, is also a hybrid material. ZnO nanosprings have already been shown to be very sensitive chemiresistors, as compared to their thin film and nanowire counterparts.[8] Unfortunately, in some cases, chemiresistors exhibit similar responses to different chemicals. Consequently, molecular surface functionalization of sensor surfaces plays a pivotal role in imparting selectivity toward specific gaseous explosives in a complex background of carrier gases, atmospheric vapors, and degradation products. A wide range of coatings, such as thiols, polymers, peptides or even antibodies, have been shown to impart selectivity to explosive analytes.[9] In this study, Au nanoparticles supported on ZnO-coated silica nanosprings have been functionalized with 6-mercaptohexanol, L-cysteine, 4-mercaptobenzoic acid, DL-thioctic acid and 11-(1-pyrenyl)-1-undecathiol. The first objective of this study is to characterize the binding of thiols to gold nanoparticles and verify the presence of explosive specific receptors at the monolayer-air interface. The second objective is to test the vapor response of the functionalized sensors within the thermal stability range of the Au-S bond. These two objectives are aligned with the ultimate goal of developing a nanospring-based sensor platform capable of selectively detecting vaporized explosives. Based on the success of the aforementioned XPS[6] and UPS[7] studies, they have been employed to achieve our first objective. The vapor sensitivity of the samples has been investigated by exposing them to gaseous analytes while monitoring their conductance. The results of these studies are reported herein.

4.2 Molecular Functionalization of Au/ZnO Nanosprings

A total of five Au/ZnO coated silica nanospring mats (area ~ 1 cm^2 grown on Si wafer) were prepared and functionalized with either 6-mercaptohexanol, L-cysteine, 4-mercaptobenzoic acid, DL-thioctic acid, or 11-(1-pyrenyl)-1-undecathiol (selected for their propensity to interact with vaporized explosives[9,11,12]) through incubation of the mats with 10 mM of the selected thiol in an appropriate solvent (6-mercaptohexanol, 4-mercaptobenzoic acid, and DL-thioctic acid in ethanol, L-cysteine in DI water and 11-(1-pyrenyl)-1-undecathiol in toluene) for 48 h to allow uniform and dense SAM formation. The substrates were subsequently washed thrice in the respective solvents and dried under a stream of argon. Relatively highly concentrated thiol solutions were used due to the high surface-to-volume ratio of nanospring mats (~ 400 m^2/g) (10 µM are typically used when functionalizing flat gold surfaces). 11-(1-pyrenyl)-1-undecathiol was synthesized following the protocol in Appendix B. Fig. 4.1 illustrates the anticipated surface attachment of the thiols to the surface of the Au nanoparticles.

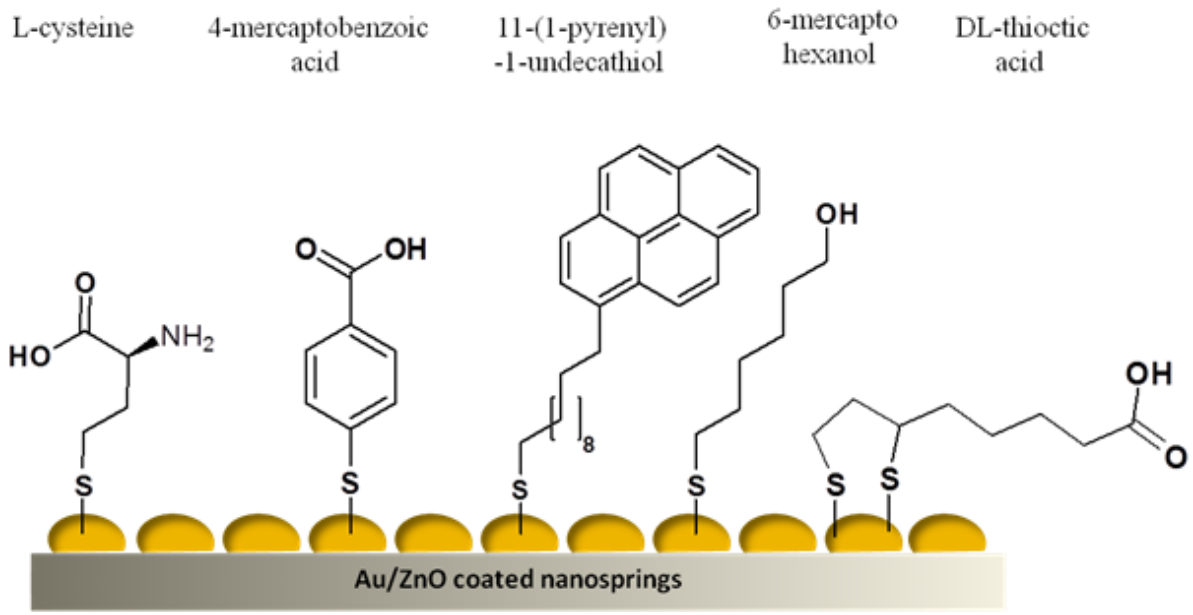

Figure 4.1 Illustration of idealized binding of thiol groups to the surface of Au/ZnO coated nanosprings.

4.3 Results and Discussion

4.3.1 X-ray Photoelectron Spectroscopy (XPS)

Broad survey XPS scans of the five SAM-functionalized Au/ZnO nanosprings samples exhibited core level states of Au (4f), C (1s), Zn (3d, 3p, 3s, 2p), O (1s) and S (2s, 2p) (not shown).The sulfur signal of 11-(1-pyrenyl)-1-undecathiol was very weak, where the weakness is attributed to a different molecular coverage relative to the other thiols, resulting from its long hydrophobic chain. The L-cysteine functionalized sample also included a N (1s) core level state associated with the amine group ($-NH_2$).To investigate the chemical environment of Au, C, S, O, Zn, and N, higher resolution scans for the corresponding specific core levels were acquired. Fig. 4.2 shows the overlapping Au 4f and Zn 3p core level states.

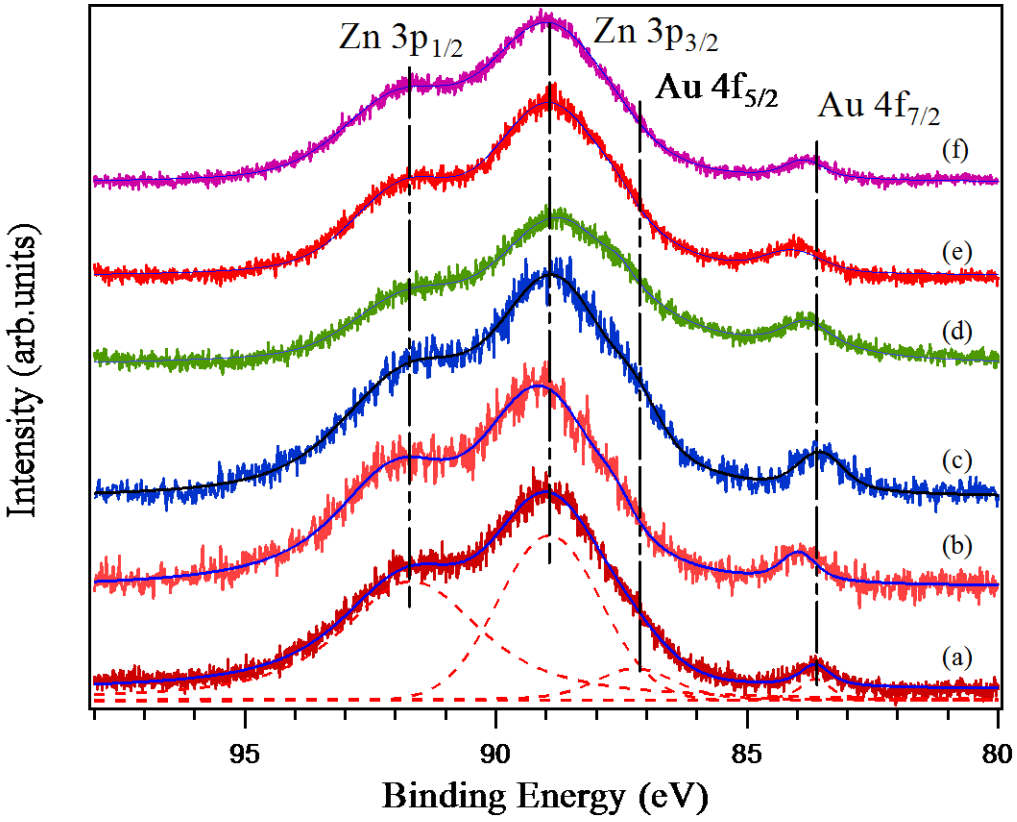

Figure 4.2 The Au 4f-Zn 3p core level states of an untreated (a) Au/ZnO sample and samples treated with (b) DL-thioctic acid, (c) 4-mercaptobenzoic acid, (d) L-cysteine, (e) 6-mercaptohexanol, and (f) 11-(1-pyrenyl)-1-undecathiol.

Quantitative analysis of the XPS spectra of the untreated Au/ZnO sample indicates an atomic ratio of Au/Zn of 0.05. The binding energy of Au 4f for the treated samples is in agreement with results reported for thiols assembled on gold nanoparticles.[6,13] For peak fitting of the spectra in Fig. 4.2 the spin-orbit splitting of Au 4f was held at 3.65 eV and the ratio of the Au $4f_{7/2}$:Au $4f_{5/2}$ intensity held at 4:3. The Au 4f binding energy shifts to higher values with thiol functionalization relative to the pristine Au/ZnO nanosprings sample, with the exception of 4-mercaptobenzoic acid. This is indicative of charge redistribution associated with the formation of the S-Au bond between the thiols and the Au nanoparticles.

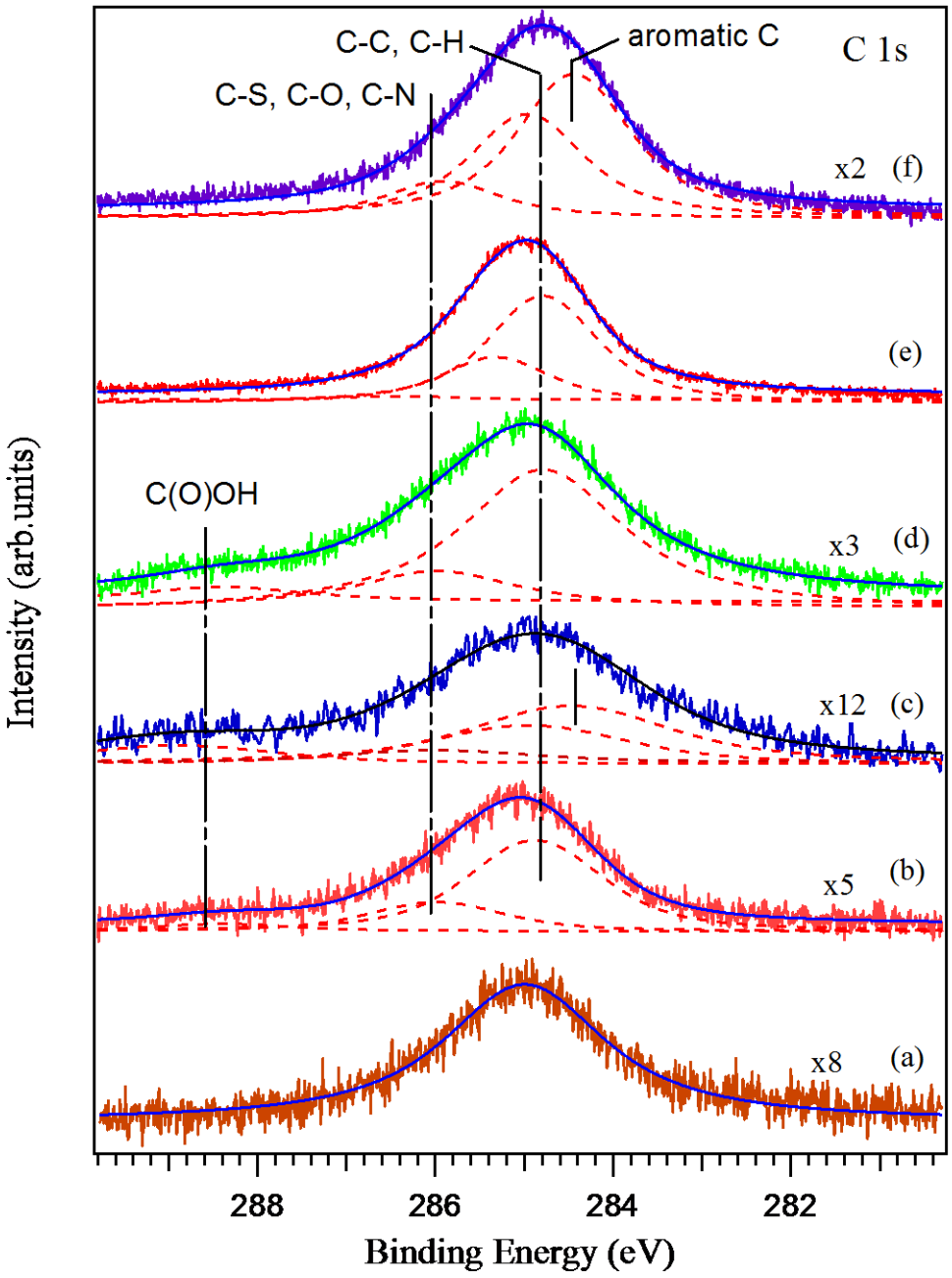

Figure 4.3 The C 1s core level states of (a) an untreated Au/ZnO sample and treated with (b) DL-thioctic acid, (c) 4-mercaptobenzoic acid, (d) L-cysteine, (e) 6-mercaptohexanol, and (f) 11-(1-pyrenyl)-1-undecathiol.

Treated samples contain a substantial amount of carbon due to the organic thiols. In order to achieve a satisfactory peak fitting (Fig. 4.3), the adventitious carbon as detected from the

untreated sample was included in the deconvolution of C 1s spectra. The position of a photoelectron peak is sensitive to the charge density on the un-ionized atom and to the degree of shielding of the core-hole generated by the loss of the electron. For carbon 1s, this sensitivity manifests itself as chemical shifts to higher binding energies for carbons in higher oxidation states or with electronegative substituents.[4] The peaks at 284.79 eV (L-cysteine), 284.80 eV (6-mercaptohexanol), 284.97 eV (11-(1-pyrenyl)-1-undecathiol) and 284.88 eV (DL-thioctic acid) are assigned to the C-C/C-H bonds of the aliphatic carbons in the respective thiols. The peak at 285.33 eV (6-mercaptohexanol) corresponds to C-S. The aromatic carbons are the singlets at 284.44 eV (11-(1-pyrenyl)-1-undecathiol) and 284.42 eV (4-mercaptobenzoic acid) since a chemical shift of ~ 0.5 eV occurs in the aromatic species relative to aliphatic unfunctionalized carbon atoms.[14] The contribution at a binding energy of ~ 286 eV is characteristic for C-S, C-O, or C-N bonds. Signals between 288-289 eV are assigned to carbon species involved in the carboxylic acid functional group (O=C-O) of L-cysteine, 4-mercaptobenzoic acid and DL-thioctic acid. These assignments are summarized in Table 4.1.

Table 4.1 C 1s spectral deconvolution results showing binding energy, possible assignment and reference.

Sample	Binding Energy (eV)	Assignment	Reference
L-cysteine	284.79	C-C, C-H	[1]
	285.99	C-N, C-O or C-S	[15,16]
	288.39	O=C-O	[14]
6-mercaptohexanol	284.80	C-C, C-H	[1]
	285.33	C-S	[16]
	286.43	C-O	[17]
11-(1-pyrenyl)-1-undecathiol	284.44	Aromatic carbon	[14]
	284.97	C-C, C-H	[14]
	285.92	C-S	[16]
DL-thioctic acid	284.88	C-C, C-H	[1]
	285.99	C-O, C-S	[16]
	288.39	O=C-O	[14]
4-mercaptobenzoic acid	284.42	Aromatic carbon	[14]
	284.72	C-C, C-H	[1]
	285.99	C-O, C-S	[16]
	288.90	O=C-O	[14]

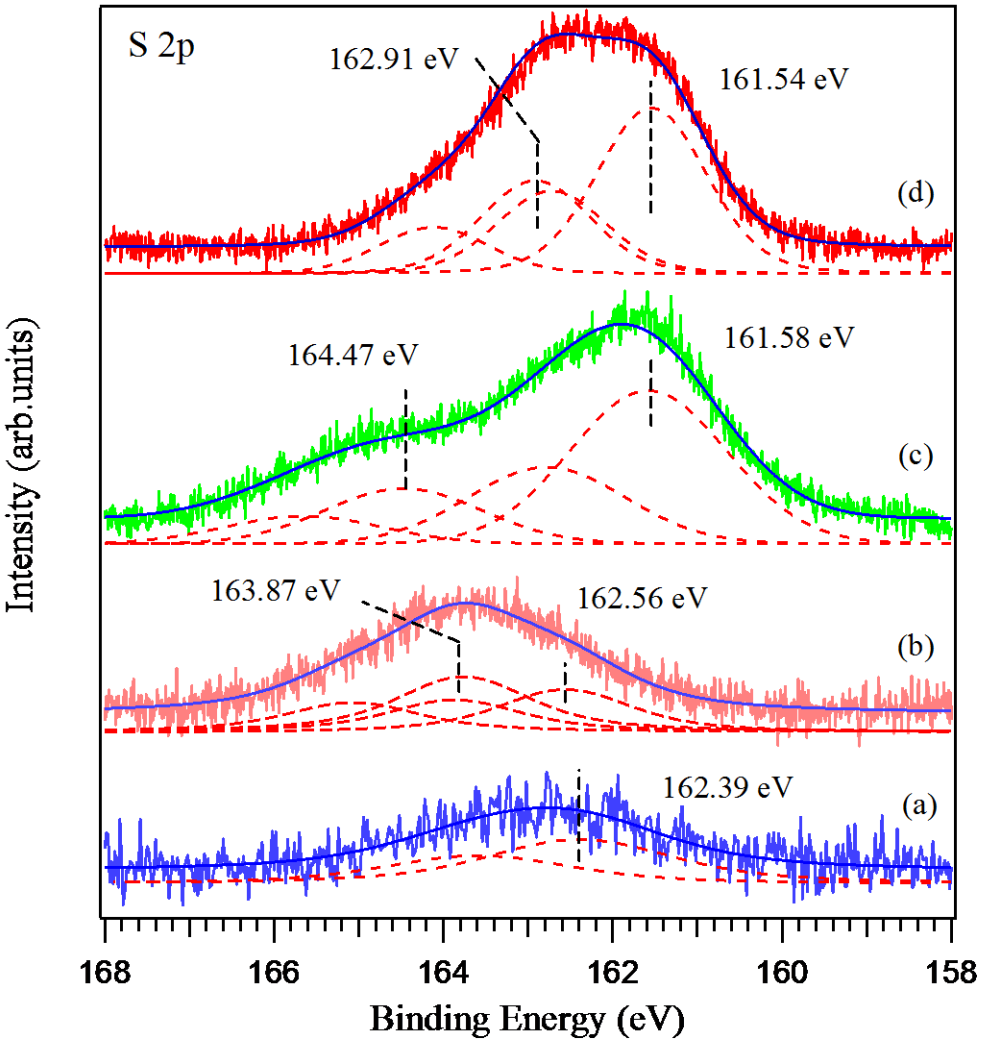

Figure 4.4 The S 2p core level states as determined by XPS for (a) 4-mercaptobenzoic acid, (b) DL-thioctic acid, (c) L-cysteine, and (d) 6-mercaptohexanol treated samples. The peaks were fitted using one or two doublets corresponding to two different sulfur species. These two sulfur species are assigned to sulfur bound to gold and sulfur bound to zinc at higher binding energies.

The S 2p signal was fitted with two or four peaks which correspond to one doublet (S $2p_{3/2,}$ S $2p_{1/2}$) or two sets of doublets (see Fig. 4.4). The fitting procedure of the S doublet consisted of using the same FWHM for both spin states, holding the spin-orbit splitting at 1.2 eV, and a branching ratio of 2:1 (S $2p_{3/2}$:S $2p_{1/2}$). The lower binding energy S doublet is ascribed to

sulfur bound to Au. The second doublet is attributed to unbound free thiol groups, and/or bonding of the headgroup instead of S[16] or a S-Zn bond.[18] In the present work, the second doublet is attributed to the S-Zn bonds because alkanethiols are known to form monolayers on ZnO surfaces through S-Zn bonding [16,18]. A peak at 170 eV, which corresponds to an S-O bond, was not observed. The conclusion is that thiol bonding is either S-Au or S-Zn. The weakness of the sulfur signals of 4-mercaptobenzoic acid and 11-(1-pyrenyl)-1-undecathiol samples reflects the attenuation of the signal due to the hydrocarbon chain length and the density of the molecules on the surface of the Au nanoparticles. It is important to note that the large surface area of the substrate in these samples, notwithstanding, would result in a higher surface density of molecules compared with planar substrates. Furthermore, additional steric hindrance is expected due to the presence of aromatic rings in the headgroup resulting in greater attenuation of the sulfur photoelectrons. Bain et al.[4] reported a weak sulfur signal in the XPS characterization of the following thiols on gold: $HS(CH_2)_{10}CH_3$, $HS(CH_2)_{10}CH_2OH$, $HS(CH_2)_{10}CO_2H$, $HS(CH_2)CO_2CH_3$, $HS(CH_2)_{10}CH_2Cl$, and $HS(CH_2)_8CN$. They invoked monolayer orientation to explain the inelastic scattering of the S 2p electrons by the molecules within the monolayer.

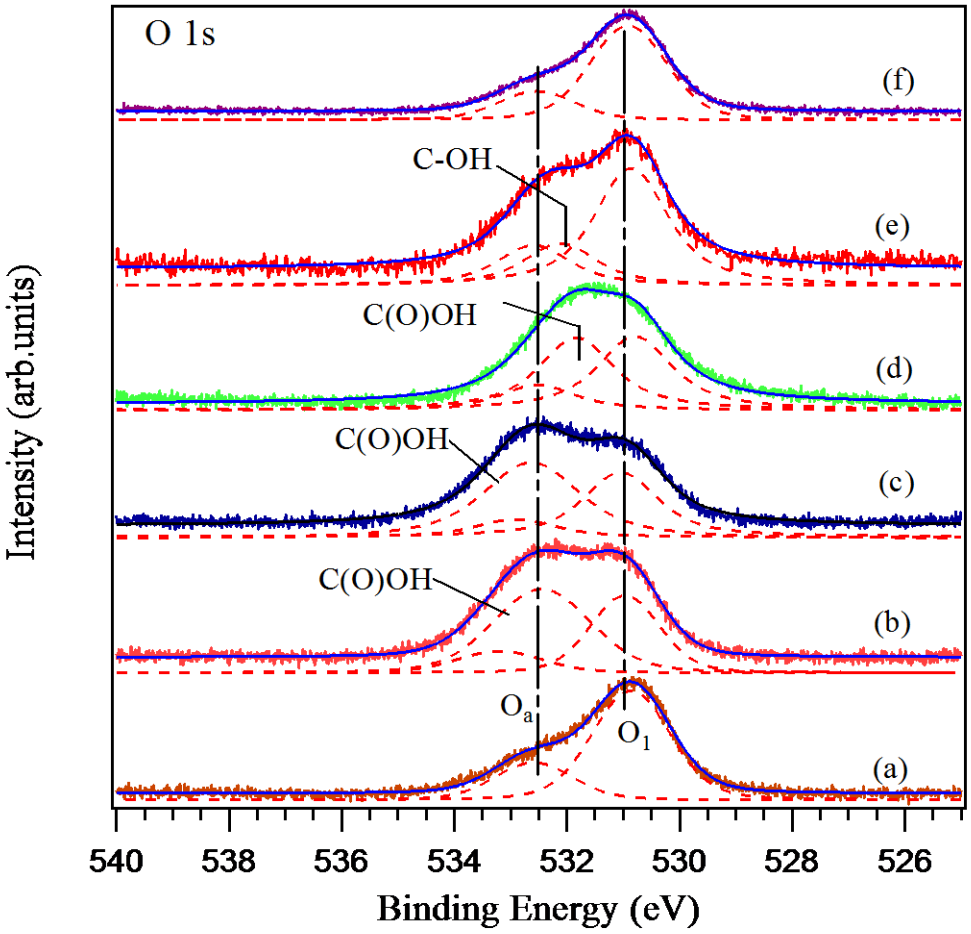

Figure 4.5 The O 1s core level states of (a) an untreated Au/ZnO sample and samples treated with (b) DL-thioctic acid, (c) 4-mercaptobenzoic acid, (d) L-cysteine, (e) 6-mercaptohexanol, and (f) 11-(1-pyrenyl)-1-undecathiol. O_1 represent O^{2-} in the wurtzite structure of ZnO and O_a chemisorbed oxygen.

Fig.4.5 shows O 1s spectra, which were fitted with two to three components. The peak at ~530 eV (O_1) is due to the lattice oxygen in ZnO, which is the O^{2-} state, while the peak at ~532.7 eV (O_a) originates from hydroxyl groups or chemisorbed oxygen.[19-20] The shape for 11-(1-pyrenyl)-1-undecathiol is virtually unchanged relative to the untreated Au/ZnO sample. Besides the fact that 11-(1-pyrenyl)-1-undecathiol is not an oxygen-containing moiety, this suggests that the oxygen sites on ZnO are not involved in the chemisorption of those

molecules onto the substrate. The significant change observed in the spectra of the other treated samples is due to large contributions from the COOH and/or OH groups. Maintaining a fixed ratio between O_1 and O_a allowed us to resolve these contributions. It can be seen that the chemisorbed oxygen shoulder is mainly affected, which suggests that those functional groups are located at the top surface of the monolayer.

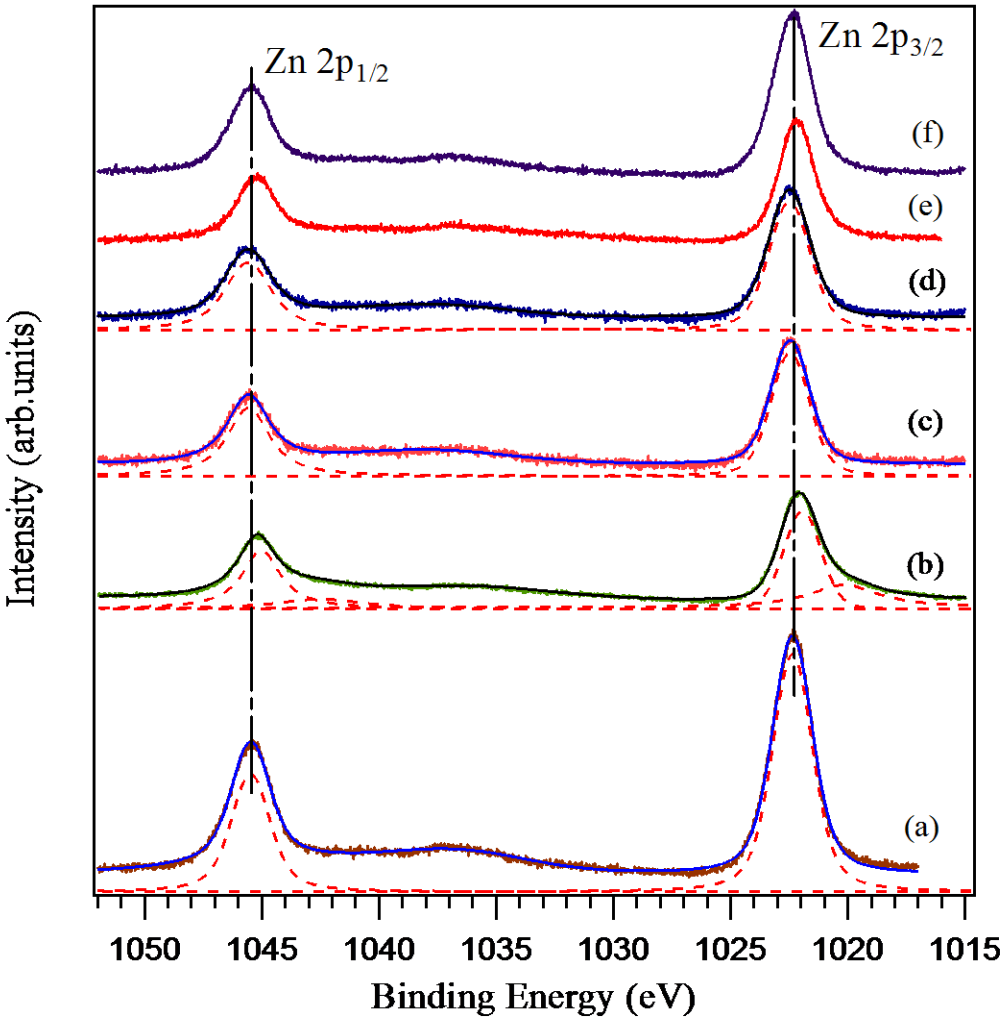

Figure 4.6 The Zn 2p core level states from Au/ZnO as determined by XPS for (a) an untreated sample and treated with (b) L-cysteine, (c) DL-thioctic acid, (d) 4-

mercaptobenzoic acid, (e) 6-mercaptohexanol, and (f) 11-(1-pyrenyl)-1-undecathiol. The pronounced asymmetry in (b) is attributed to electrostatic interaction.

The binding energy of the Zn $2p_{3/2}$ and Zn $2p_{1/2}$ core level states (Fig. 4.6) are at ~1022 eV and ~1045 eV, respectively, consistent with ZnO. The peak position for Zn $2p_{3/2}$ is in good agreement with the wurtzite phase of ZnO at 1022.4 eV.[21] The absence of a metallic zinc peak at 1021.5 eV indicates that the ionization state of Zn is Zn^{2+}.[19] There is a very small spectral contribution on the lower binding energy side of the L-cysteine treated sample. This may arise from the electrostatic interaction between Zn^{2+} ions and the electrically charges sites of L-cysteine which are ($-COO^{-}-$) and ($-NH_3^{+}-$) when L-cysteine exists in the zwitterionic form. Alternatively, it could be attributed to S-Zn bonds. However, the latter possibility is less likely since the four other thiols have been grafted following the same protocol, and the S-Zn bond therefore should have appeared in the Zn 2p core level states of all the samples. The attenuation of the Zn 2p photoelectrons upon treatment, in conjunction with the peaks assignment of the S 2p core level states, demonstrates the formation of an overlayer and the potential formation of S-Zn bonds.

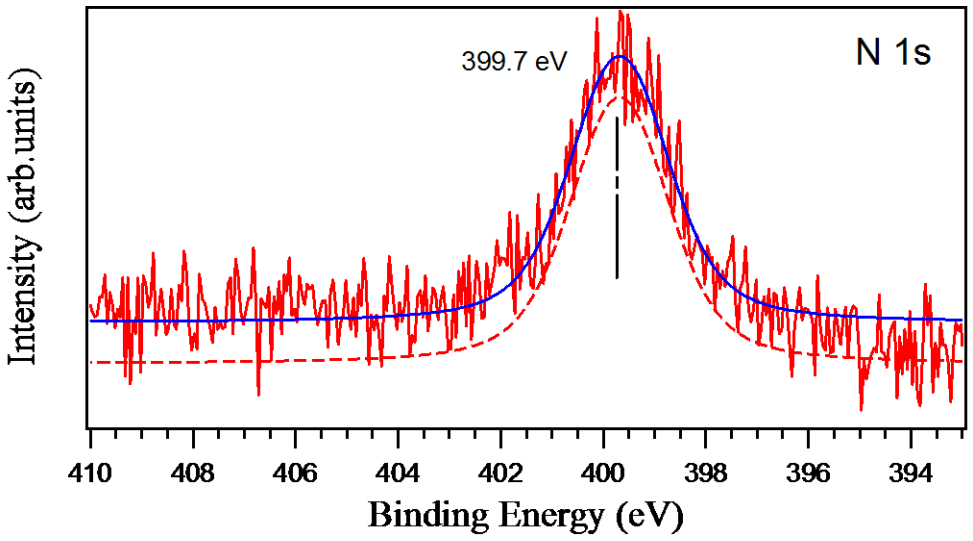

Figure 4.7 The N 1s core level for L-cysteine functionalized Au/ZnO nanospring sample.

The N 1s core level state for L-cysteine is shown in Fig. 4.7. The single peak at ~ 400 eV corresponds to NH_x species.[1] The N 1s signal provides confirmation for the location of the headgroup exclusively at the top surface of the monolayer. Signals from oxidized nitrogen species (NO_x) at higher binding energies were not observed, indicative of the stability and resistance of L-cysteine to oxidation.

Table 4.2 summarizes the atomic ratios of the elements calculated from the integration of the XPS core level states, which were corrected by Scofield sensitivity factors. These factors were obtained from the literature.[22,23] The area of carbon impurities, as detected in the untreated sample, was subtracted from the area of each C 1s core level prior to the elemental analysis.

Table 4.2 Atomic ratios of elements at the outer surface of treated samples

Sample	C1s/S2p		$\frac{S2p}{Au}$	$\frac{Au}{Zn}$	$\frac{S2p}{Zn2p+Au}$	$\frac{C1s+S2p}{Zn2p+Au}$
	Theoretical	XPS				
L-cysteine	1.12	1.40	46.06	0.014	0.64	2.09
6-mercaptohexanol	2.25	2.22	58.59	0.018	1.01	4.38
11-(1-pyrenyl)-1-undecathiol	10.5	10.1	5.88	0.028	0.16	2.59
4-mercaptobenzoic acid	2.62	2.47	6.59	0.057	0.36	1.69

DL-thioctic acid	1.50	1.42	64.73	0.028	1.17	3.67

The carbon to sulfur ratios (C1s/S2p) are close to the expected theoretical values corresponding to the stoichiometry of the linker molecules, which confirm the quality of monolayers and the reliability of the sensitivity factors used. The Au/Zn ratios reflect the low content of Au in the samples. Compared with the value of 0.05 for the untreated sample, the relative decrease (except for 4-mercaptobenzoic acid) provides additional evidence of a monolayer on the Au nanoparticles. For 4-mercaptobenzoic acid the change is likely due to differences in chemical interactions with Au/ZnO and in molecular orientation. The S 2p/Au ratios follow the trend of the S 2p signal detected from the respective samples, but the values should not be too far from unity, if sulfur binds exclusively to Au. Conversely, the S 2p/Au+Zn ratios are more reasonable, consistent with chemisorption through S-Au and S-Zn bonds.

The nature of the interface between Au/ZnO nanosprings and the adsorbed thiols is an important point of interest. X-ray absorption near-edge spectroscopy (XANES) studies of thiol-capped ZnO nanoparticles have demonstrated the existence of a ZnS-ZnO interface at the surface of the nanoparticles, with both ZnS and ZnO showing a wurtzite structure. [24,25,26] The S 2p core level states from L-cysteine, 6-mercaptohexanol, and DL-thioctic acid treated samples clearly exhibited two sulfur signals, which were assigned to S-Au, and S-Zn bonds. In the other samples the S-Au bonds (1-(1-pyrenyl)-1-undecathiol and 4-mercaptobenzoic acid) were dominant. The electron affinity of the benzene rings in 1-(1-pyrenyl)-1-undecathiol and 4-mercaptobenzoic acid may explain the weakness or failure of the S-Zn coordination.

Packing density and order/disorder of SAMs:

Packing densities of thiols were calculated from XPS data following the method described in Ref.[27] Since XPS probes only a few atomic layers of the sample, to estimate the packing density of thiols on nanoparticles XPS integrals must be corrected for the electron escape depth ($\lambda\cos\theta$), where λ is the inelastic mean free path (IMFP) and θ the emission angle to the surface normal. For normal emission, as in our experiments, the escape depth reduces to simply λ. From the NIST Electron Inelastic Free Path Database, the IMFPs of gold and zinc are 1.78 nm and 2 nm, respectively.[22]

The shell method models nanoparticles as a central atom surrounded by shells (layers) of atoms, where the number of atoms in the *n*th shell is $10n^2+2$.[27] The total number of shells can then be determined from the diameters of the atom and the nanoparticles. The number of layers sampled by XPS is the ratio of the escape depth to the atom diameter. From these estimates, a 10 nm gold nanoparticles contains 18 shells but only 6 are sampled, while zinc nanoparticles of 7 nm (size of coordinated zinc in a 18 nm ZnO crystal) contain14 shells, 8 of which are sampled.

The S to Au or to Zn atomic ratios are corrected as follows:

$$\frac{S}{X_{Surface}} = \left(\frac{\sum_{n=n_i}^{n_o} (10n^2 + 2)}{10n_o^{\,2} + 2} \right) \left(\frac{S}{X} \right) \qquad \text{X = Au, Zn} \qquad (4.1)$$

, where n_i is the deepest layer sampled and n_o the outer layer. The surface of ~ 10 nm gold nanoparticles mostly contains (100) crystal planes.[27] Large grains ZnO (~20 nm) correspond to the growth mode with c-axis parallel to the substrate which privileges 100 and 110 orientations, and the surface planes are therefore predominantly (100).

The number of lattice points per unit area of a crystal plane is given by:

$$\rho_{hkl} = \frac{nd_{hkl}}{\Omega} \tag{4.2}$$

, where n is the number of lattice points per unit cell, Ω the volume of the unit cell, and d_{hkl} the interplanar spacing.

The packing density of atoms on a plane is calculated as follows:

$$\sigma_{hkl} = N_0 \rho_{hkl} \tag{4.3}$$

, where N_0 is the number of atoms per lattice point in the plane (hkl). These quantities for Au and Zn are:

$$\sigma_{hkl}(Au) = \frac{2}{a^2\left(h^2 + k^2 + l^2\right)^{1/2}} \tag{4.4}$$

and

$$\sigma_{hkl}(Zn) = \frac{2}{\sqrt{3}a^2 c\left(\frac{4}{3}\frac{h^2 + hk + k^2}{a^2} + \frac{l^2}{c^2}\right)^{1/2}} \tag{4.5}$$

Finally, the packing density of thiols can be approximated from XPS data using the following relationship:

$$PD = \left(\frac{S}{X_{Surface}}\right)\left(\frac{TH}{S}\right)\left(\sigma_{hkl}\right) \tag{4.6}$$

The factor $\frac{TH}{S}$ is 2 for DL-thioctic acid and 1 for the other thiols in this study.

The surface coverage and packing density calculated by the method described above are summarized in Table 4.3.

Table 4.3 Surface coverage and packing density of thiols on Au and Zn as estimated from XPS data

Thiols	L-cysteine	6-mercaptohexanol	11-(1-pyrenyl)-1-undecathiol	DL-thioctic acid	4-mercaptobenzoic acid
Coverage on Au	0.451	0.271	0.0435	0.106	0.0791
PD on Au (molecules/cm^2)	$5.42x10^{14}$	$3.26x10^{14}$	$5.23x10^{13}$	$2.55x10^{14}$	$9.50x10^{13}$
Coverage on Zn	0.239	0.215	--------	0.0475	--------
PD on Zn (molecules/cm^2)	$2.83x10^{14}$	$2.54x10^{14}$	--------	$1.12x10^{14}$	--------

The values agree with the SAMs packing densities which are in the order of 10^{14} molecules/cm^2 on flat gold surface.[28] L-cysteine, 6-mercaptohexanol, and DL-thioctic acid are more densely packed than 4-mercaptobenzoic acid and 11-(1-pyrenyl)-1-undecathiol. The latter thiols have larger end groups, where the reduced packing densities may be due to steric hindrance.

Ordering of thiols is another important factor in their effectiveness as receptors. It has been reported for 4-mercaptobenzoic acid that the proximity of the carboxyl group to the surface of the monolayer – compared to similar types of thiols - reduces its interaction with the substrate, resulting in an increased reactivity with vapors of analytes.[29,30] SAMs of DL-thioctic acid formed in ethanol are highly disordered due to hydrogen bonding between neighboring molecules with a tilt of 38° that results in the loose packing of the SAMs.[31]

Unlike DL-thioctic, the higher degree of ordering of 6-mercaptohexanol SAMs is ascribed to complementary effects, such as the solubility of solvents with the thiol chains and hydrogen bonding of adjacent –OH of thiols or –OH with solvents.[32] Note, a high packing density is required to order long chain molecules within a monolayer;[33] and if this applies to SAMs of 11-(1-pyrenyl)-1-undecathiol with an increased steric hindrance of the headgroups, they are likely to be disordered. Finally, SAMs of L-cysteine are highly ordered, most likely due to intermolecular and intramolecular interactions of hydrophilic ammonium and carboxylic groups that lead to the formation of hydrogen bonds among adsorbed molecules.[34]

4.3.2 Ultraviolet Photoelectron Spectroscopy (UPS)

UPS spectra (He I emission line) of the bare ZnO nanospring sample, the untreated Au/ZnO and the five treated samples are displayed in Fig. 4.8 (upper panel). The spectrum of the untreated sample is reminiscent of polycrystalline Au and ZnO valence bands with some attenuation and hybridization. The Au 5d electrons form a broad band between 2-8 eV and the 6s band is observed between 2 eV and the Fermi level. Note, the 6s band extends to much higher binding energy and is strongly hybridized with the 5d bands.[35] As for ZnO, the valence band extends from 3 to 8 eV; theory predicts that the emission from 3-5 eV corresponds to non-bonding O 2p orbitals, and between 5-8 eV to a bonding between the O 2p and Zn 4s orbitals.[36] A feature at 10 eV of the valence band spectra of bare ZnO, which arises from the Zn 3d band, is attenuated upon decoration with Au nanoparticles. Duwez et al.[7] noted that one of the difficulties one encounters when interpreting valence band spectra consisting of Au and organics is the superimposition of the Au 5d signal with the valence band structure of the organic material. There are, however, obvious changes to the shape of the Au/ZnO spectrum upon the thiol functionalization. For instance, the Au 5d and Zn 4s-O

2p bands are attenuated differently. For DL-thioctic acid and 4-mercaptobenzoic acid functionalization these bands are almost completely suppressed, yet are still resolvable upon functionalization with L-cysteine, 6-mercaptohexanol and 11-(1-pyrenyl)-1-undecathiol. These modifications are indicative of the formation of an overlayer on the surface which is chemically bonded not only to gold, but also to Zn, as demonstrated by the change in the ZnO features in the range of 5-8 eV. The occurrence of the maximum at different binding energies is suggestive of different molecule orientations. The bond formation occurs through a rearrangement of the orbitals of the substrate and of the adsorbed molecules.[7] The thickness and the compactness of the film will affect the intensity of the photoemission of the underlying substrate. XPS analysis showed that the thiols have different packing densities on Au as compared to ZnO. The presence of contributions from Au and ZnO in the valence spectra is related to the hydrocarbon chain length, the size of the end group and the molecular orientation. Finally, the feature at ~15 eV is the background of secondary electrons that arise from the substrate near-surface region, as well as the thiol layer.[3] The onset of secondary electrons was used to determine the change in the work function with respect to the untreated sample.

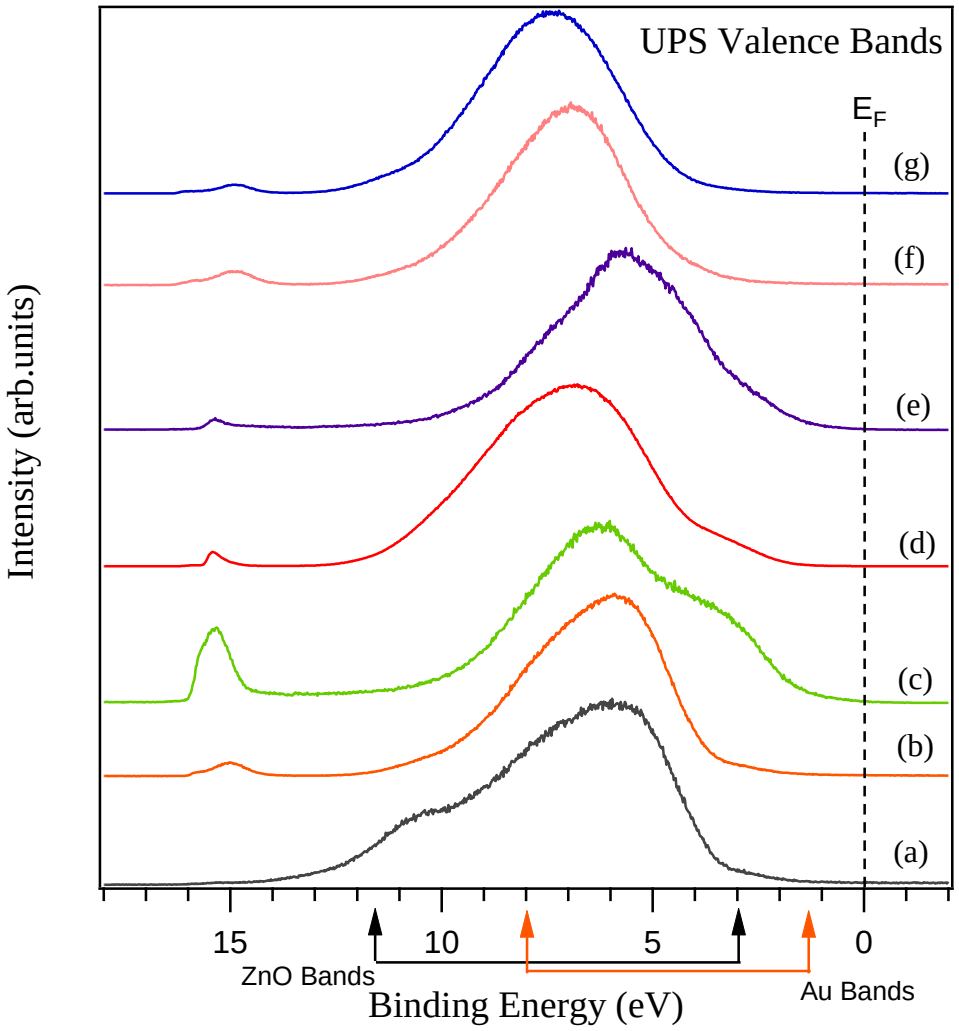
UPS Valence Bands
E_F
(g)
(f)
(e)
(d)
(c)
(b)
(a)
Intensity (arb.units)
15
10
5
0
ZnO Bands
Au Bands
Binding Energy (eV)

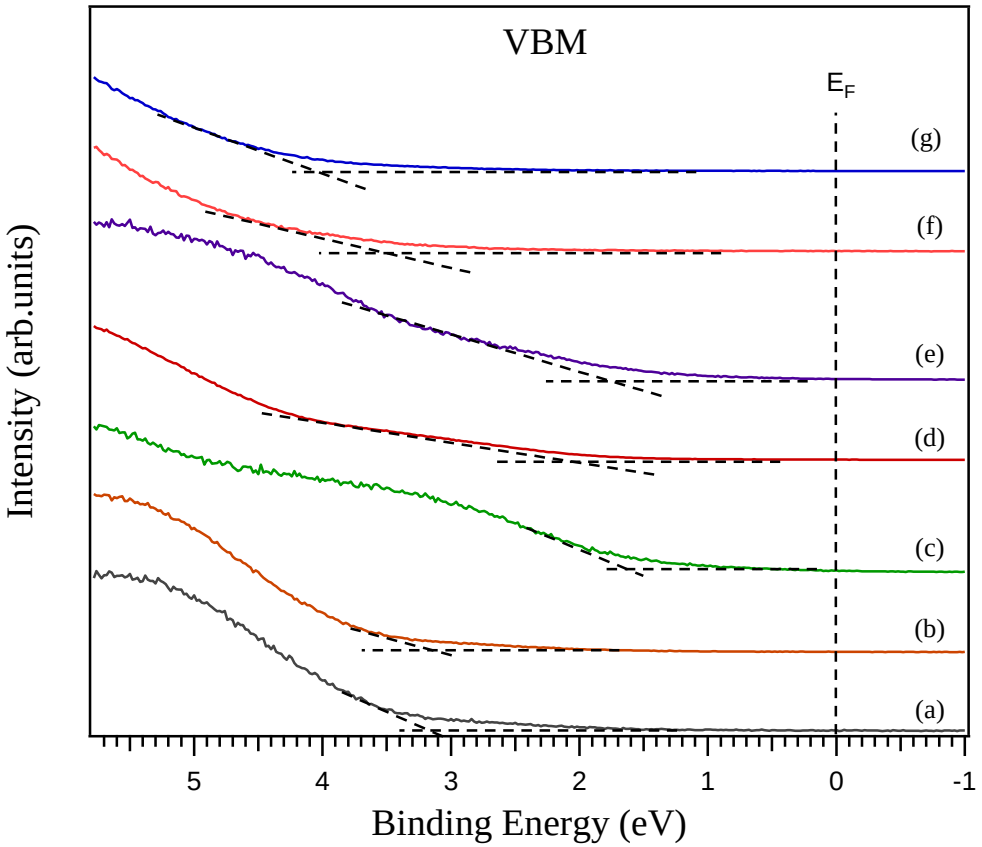

Figure 4.8 (Upper panel).The UPS (He I) valence bands spectra for (a) a bare ZnO nanospring-mat, (b) an untreated Au/ZnO nanospring-mat and treated with (c) L-cysteine, (d) 6-mercaptohexanol, (e) 11-(1-pyrenyl)-1-undecathiol, (f) DL-thioctic acid, and (g) 4-mercaptobenzoic acid. (Lower panel).The Valence band maximum (VBM) of the same samples obtained by linear extrapolations.

Table 4.4 Position of the VBM and change in the work function of the treated samples

Sample treated with	L-cysteine	11-(1-pyrenyl)-1-undecathiol	6-mercaptohexanol	4-mercaptobenzoic acid	DL-thioctic acid
VBM (eV)	1.50	1.45	1.80	3.10	3.05
ΔΦ(eV)	+0.17	-0.38	-0.02	+0.10	+0.22

Also shown in Fig. 4.8 (lower panel) are linear extrapolations of the leading edge to zero intensity to obtain VBM positions of the samples. Band bending and dipole layer formation upon chemisorption lead to shifts in the VBM (band bending), in electron binding energies and in the energy cutoff (change in the work function) (Table 4.4).[3] Different values of the VBM position and $\Delta\Phi$ illustrate differences in the self-assembled films.

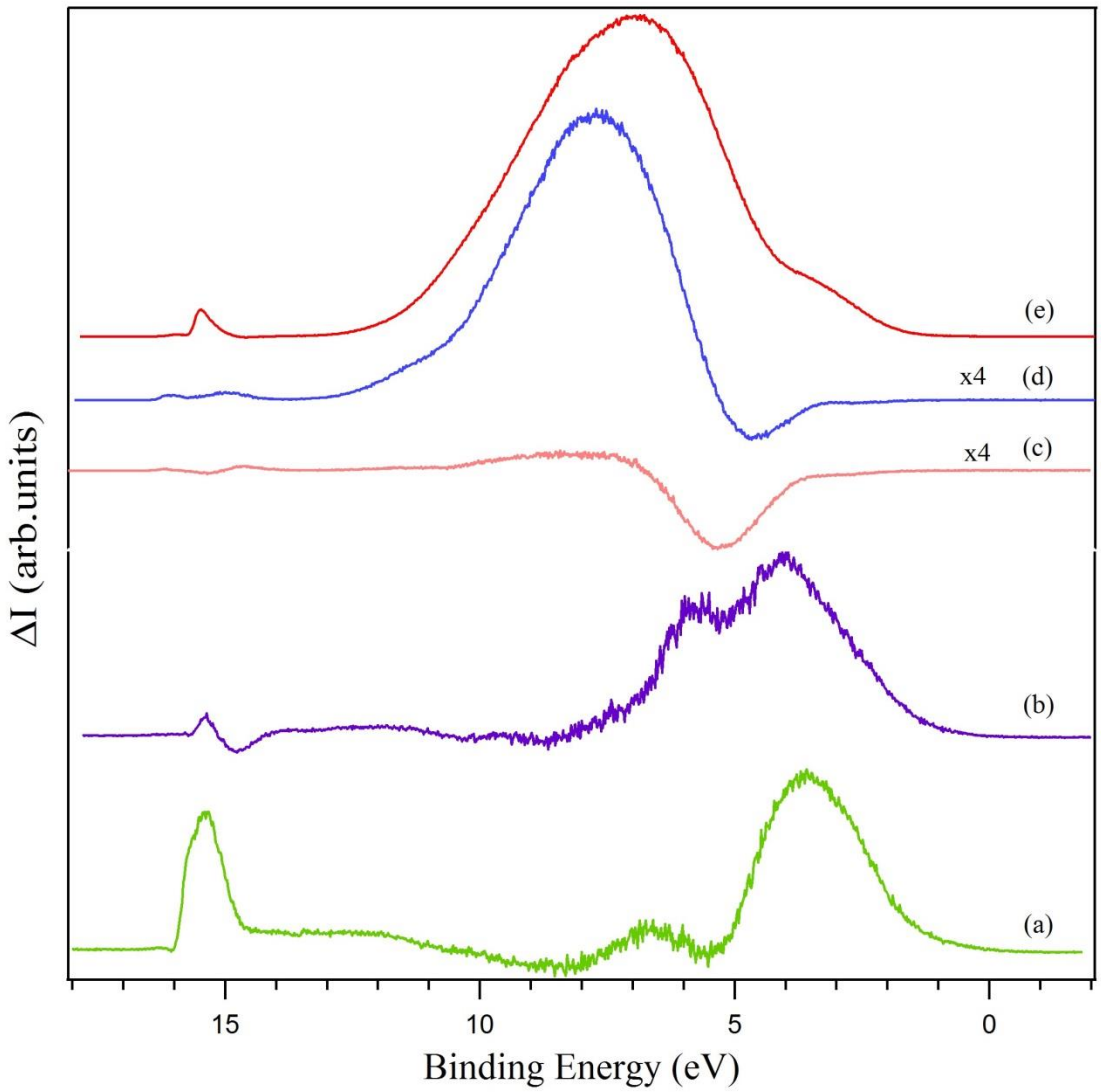

Figure 4.9 UPS difference spectra for chemisorbed (a) L-cysteine, (b) 11-(1-pyrenyl)-1-undecathiol, (c) DL-thioctic acid, (d) 4-mercaptobenzoic acid, and (e) 6-mercaptohexanol on Au/ZnO nanospring-mats.

Difference spectra analysis of the valence band spectra in Fig. 4.9 was performed to elucidate the changes in the valence band density of states of the five thiols. The procedure is described in detail in Ref. [37] The results are shown in Fig. 4.9. Negative features in the difference curve arise from suppression of valence band density of states of the Au/ZnO nanosprings substrate. The attenuation is attributable to either electron scattering arising from disorder in the thiol layer or hybridization of S and Au surface atoms. The negative features at a binding energy of ~ 5eV of the difference curves of L-cysteine, DL-thioctic acid and 4-mercaptobenzoic acid correspond to Au d-bands prior to thiol functionalization. The attenuation of the Au d-bands in the case of DL-thioctic acid is due to electron scattering due to disorder within the layer (see section 4.3.1), which also accounts for the lack of distinguishable molecular orbitals of the adsorbate. The difference spectrum of 4-mercaptobenzoic acid, taken in conjunction with its low coverage (Table 4.3), suggests that the attenuation of the Au feature is due to hybridization of S with the Au surface, as opposed to electron scattering. The molecular orbitals of 4-mercaptobenzoic acid in the range of ~6-12 eV support this conclusion. The new density of states in the range of 1-2 eV for L-cysteine, 11-(1-pyrenyl)-1-undecathiol, and 6-mercaptohexanol is attributed to hybridization of the antibonding S 3p-states with the Au 5d-bands, where the additional new states with binding energies > 2 eV are the molecular orbitals of the respective thiols, which may, or may not, hybridize with the Au d-bands. In the case of L-cysteine, there is a contribution from N 2p states above 1.5 eV.[38] Note, the assignments are based on the assumption that the

S antibonding 3p orbital does not mix with the wavefunctions on the hydrocarbon chain. The formation of hybrid orbitals of both bonding and antibonding type, below and above the metal d bands, is consistent with the Newns-Anderson model for atomic and molecular chemisorption on metal surfaces.[39] This is clearly demonstrated by the L-cysteine difference spectrum, which confirms Felice and co-workers [40] theoretical predictions of the above mentioned model applied to cysteine chemisorbed on Au (111). The bonding and antibonding orbitals are both π-like and σ-like. In the outer valence band region ~6-12 eV, bands can be attributed to thiol orbitals with contributions from C 2p and N 2p states in the specific case of L-cysteine. These orbitals also contribute to the bonding of the molecule to the surface, especially the ZnO surface where the bonding primarily occurs via high-lying orbitals.[41]

4.3.3 Gaseous Analytes Detection Properties

To test the response of the functionalized samples with respect to vaporized explosive compounds, the sensor responses have been measured as relative changes in conductance normalized with respect to a baseline signal level when no vapor is present. The results for exposures to different vapors are displayed in Fig. 4.10. The operational temperatures of the sensors functionalized with 11-(1-pyrenyl)-1-undecathiol and DL-thioctic acid were 100°C, and 150°C for the other four sensors. The sensors were heated to thermally activate carriers.[42]

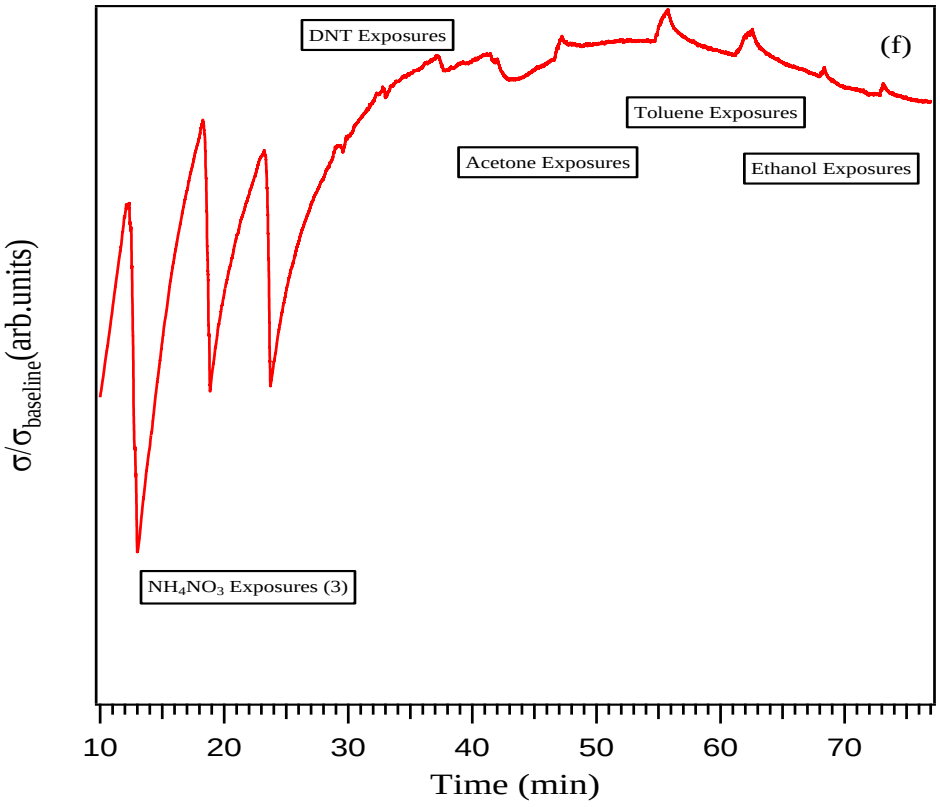
DNT Exposures
(f)
Toluene Exposures
Acetone Exposures
Ethanol Exposures
NH4NO3 Exposures (3)
σ/σbaseline(arb.units)
10
20
30
40
50
60
70
Time (min)

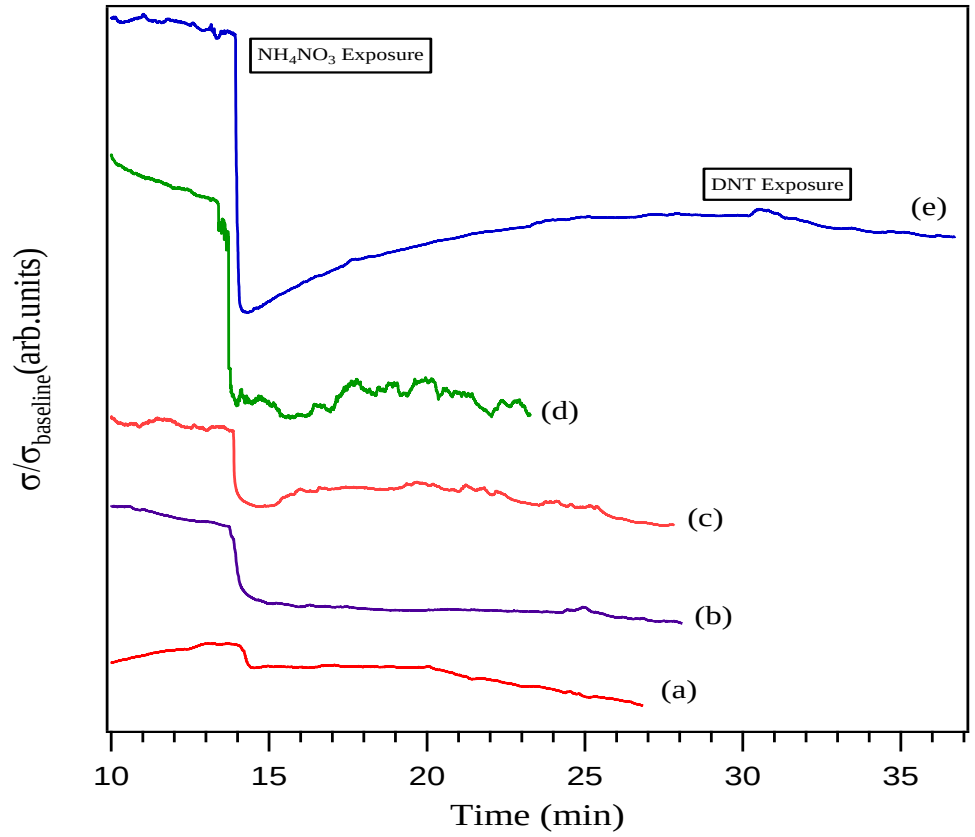
NH4NO3 Exposure
DNT Exposure
(e)
(d)
(c)
(b)
(a)
σ/σbaseline(arb.units)
10
15
20
25
30
35
Time (min)

Figure 4.10 The relative change in conductance of (a) untreated Au/ZnO nanospring-mat and samples treated with (b) 11-(1-pyrenyl)-1-undecathiol, (c) DL-thioctic acid, and (d) L-cysteine upon exposure to ammonium nitrate, (e) 4-mercaptobenzoic acid, and (f) 6-mercaptohexanol upon exposure to ammonium nitrate, DNT, acetone, toluene, and ethanol.

It has been reported that upon heating to temperatures over 70 °C, monolayers of alkanethiols on gold begin desorbing, but the rate of desorption is dependent on the temperature, ambient medium, and chain length of the adsorbate.[4] Desorption is most rapid in a hydrocarbon solvent, slower in ethanol and in still air. Long-chain thiols form monolayers that are more stable than those of short-chain thiols. The thermal stability of the adsorbate molecule is an issue for ZnO nanospring chemiresistors, which operate optimally at 400 °C. XPS was performed to verify the stability of the thiols on ZnO nanosprings at the above-mentioned operational temperatures. The results of these tests are presented in Appendix A. These results and the data in Fig. 4.10 demonstrate that the linker molecules were much more thermally stable than those adsorbed on gold, where we hypothesize that this is due to the attachment of the molecules not only to gold but also to ZnO. All the functionalized samples showed higher response to ammonium nitrate (NH_4NO_3), relative to the untreated sample, where the conductance of all the samples decreased irreversibly upon exposure to NH_4NO_3. The exception was 6-mercaptohexanol, which recovered and responded to multiple exposures. It also responded to additional compounds, including 2,4-dinitrotoluene (DNT), toluene, acetone, and ethanol. 4-mercaptobenzoic acid and 6-mercaptohexanol responses show that the analytes that are liquid (solid) at room temperature have positive (negative) change in conductance. A decrease in the conductance of the sample upon exposure to vapors of solid analytes indicates binding of vapors to the functional groups. For the liquid analytes,

diffusion of the vapor molecules into the pores of the film increases the average permittivity, which in turn increases the conductance because the activation energy and height of the potential well barriers to carrier transport are expected to decrease.[6] For 6-mercaptohexanol, changes in the conductance clearly reflect the adsorption of vapors of analytes followed by desorption. The response to NH_4NO_3 is plotted in Fig. 4.11 as function of the position of the VBM.

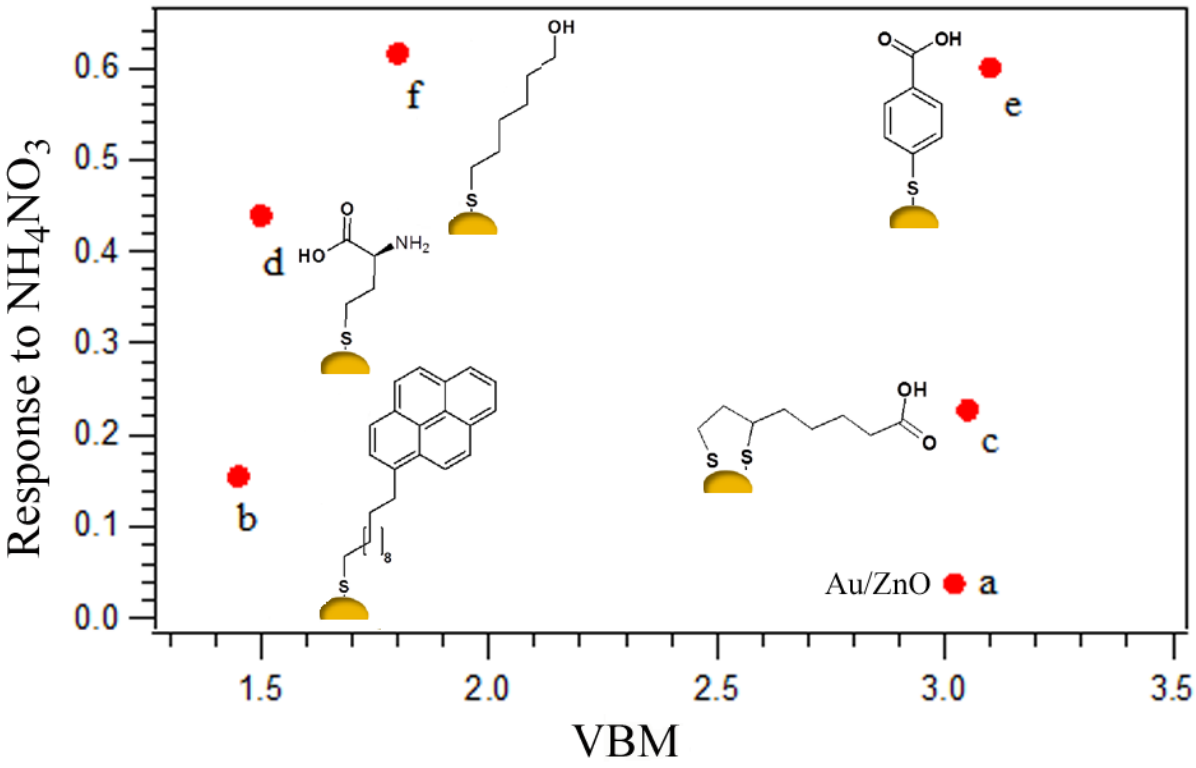

Figure 4.11 Samples response to ammonium nitrate exposure as a function of the position of the VBM. (a) Untreated Au/ZnO nanospring-mat and samples treated with (b) 11-(1-pyrenyl)-1-undecathiol, (c) DL-thioctic acid, (d) L-cysteine, (e) 4-mercaptobenzoic acid, and (f) 6-mercaptohexanol.

4-mercaptobenzoic acid and 6-mercaptohexanol exhibited the strongest responses by a factor of 4 and 5 relative to 11-(1-pyrenyl)-1-undecathiol, the least responsive thiol. One would

expect that the closer the VBM to the Fermi level, the better the sensor, but Fig. 4.11 suggests that the position of the VBM has little, to no, influence in the response to vapors of ammonium nitrate. On the contrary, the responses reflect the packing density and/or ordering of thiols, as determined in the XPS section. Moreover, given the dissimilarity of the five thiols, chemical interactions are also likely to play an important role in sensing.

Chemical interaction between receptors and Au/ZnO surface:

All of the receptors, with the exception of 4-mercaptobenzoic acid, are expected to have high electron density on the sulfur atom. In the case of 4-mercaptobenzoic acid, the lone pair electrons on the sulfur are delocalized within the aromatic benzene ring, which may result in different interactions with Au/ZnO relative to the other thiols.

Chemical interactions between functional groups of receptors and explosive vapors:

Heated solid ammonium nitrate (NH_4NO_3) produces ammonia (NH_3) and oxidizing nitric acid (HNO_3) as the two main gaseous species, along with gaseous degradation products (N_2, H_2O, O_2, OH, HNO and NO_3) and ammonium nitrate.[43] Receptors with carboxylic acid groups (L-cysteine, 4-mercaptobenzoic acid, DL-thioctic acid) may interact with ammonium (NH_4^+) through electrostatic interactions and with NH_3 via hydrogen bonding. On the other hand, receptors with alcohol or amino groups (6-mercaptohexanol, L-cysteine) will only interact via hydrogen bonds. The polarized nitro group ($R\text{-}NO_2$), found in many commonly used military explosives is known to interact strongly with polar groups, such as -COOH and –OH via ionic and hydrogen bond interactions. Thus, all of the receptors, except for 11-(1-pyrenyl)-1-undecathiol, may interact strongly with nitrate ions (NO_3^-). The sensor data (Fig. 12), with the exception of DL-thioctic acid, are in good agreement with the above description of chemical interactions between functional groups of receptors and vapors of ammonium

nitrate. In fact, 4-mercaptobenzoic acid, 6-mercaptohexanol and L-cysteine respond better, while the response is low for 11-(1-pyrenyl)-1-undecathiol. The former have polar linker headgroups of the form -COOH, -OH, and -NH_2 that interact with components from ammonium nitrate, while the latter does not. However, DL-thioctic acid, which has the polar linker -COOH headgroup, exhibits a relatively lower response. The characterization data already showed that the surface energy barrier is relatively high for DL-thioctic acid treated samples. From a chemical standpoint, the low response is attributable to poor long range order of the DL-thioctic acid films, where it has been reported that well-ordered films are obtained if one uses ethanol-acetic acid as solvent.[44]

4.4 Conclusions

In this chapter, we have investigated the chemisorption of alkyl thiols on Au/ZnO nanosprings by XPS and UPS and correlated the data with the response of sensors constructed with these materials to ammonium nitrate, a signature of explosives. The thiols used in the study are L-cysteine, 6-mercaptohexanol, 11-(1-pyrenyl)-1-undecathiol, 4-mercaptobenzoic acid, and DL-thioctic acid. Our results show that the thiol bond involves not only S-Au bonds, but also S-Zn bonds. XPS analysis reveals that the thiols' headgroups are located at the monolayer-air interface and are resistant to oxidation. The weakness of the sulfur signals of 4-mercaptobenzoic acid and 11-(1-pyrenyl)-1-undecathiol treated samples suggests that steric screening effects play an important role in the scattering of the photoelectrons. The C/S ratios are in good agreement with the stoichiometry of the respective thiols, confirming the quality of the monolayers. The analysis of the UPS valence band spectra of the thiolated samples exhibited contributions from the molecular orbitals of the thiols, S-Au and S-Zn bonding, the Au/ZnO nanospring substrate, and attenuation of some

substrate bands due to thiol induced scattering. The attenuation of the Au d bands, as demonstrated by UPS difference curves, reflects the conformation of each linker molecule and their orientation with respect to the surface normal. UPS difference spectra also revealed bands associated with carbon 2p and nitrogen 2p states, and more importantly, with S-Au bonding and antibonding orbitals of both π- and σ-type. The formation of hybrid orbitals of both antibonding and bonding type, above and below the metal d-bands, is characteristic of molecular chemisorption on metal surfaces.

Vapor-sensing tests show that the thiols are more thermally stable on Au/ZnO nanosprings than on Au thin films. It is hypothesized that chemisorption to the ZnO surface is responsible for this enhanced stability. Regardless, the Au nanoparticles are necessary to create that depletion layer critical to sensing. The samples are highly responsive to vaporized ammonium nitrate. Au/ZnO nanosprings with SAMs of 6-mercaptohexanol or 4-mercaptobenzoic acid exhibited the strongest responses. The packing density and ordering of the SAMs layers appear to be critical for obtaining a strong response to analytes. Therefore, protocols should be developed that maximize long range order. Only then will it be possible to effectively compare thiol functionalization to one another. In order to optimize the response of these thiols, future experiments will focus on increasing the testing temperature to find the desorption point as well as monitoring the vapor dose.

References

(1) Scott, A. & Janes, D. B. Characterization of electrochemically grafted molecular layers on silicon for electronic device applications. *J. Appl. Phys.* **105,** 073512 (2009).

(2) Kronik, L. & Koch, N. Electronic Properties of Organic-Based Interfaces. *MRS Bull.* **35,** 417–419 (2010).

(3) Alloway, D. M. *et al.* Interface Dipoles Arising from Self-Assembled Monolayers on Gold: UV-Photoemission Studies of Alkanethiols and Partially Fluorinated Alkanethiols. *J. Phys. Chem. B* **107,** 11690–11699 (2003).

(4) Bain, C. D. *et al.* Formation of monolayer films by the spontaneous assembly of organic thiols from solution onto gold. *J. Am. Chem. Soc.* **111,** 321–335 (1989).

(5) Porter, M. D., Bright, T. B., Allara, D. L. & Chidsey, C. E. D. Spontaneously organized molecular assemblies. 4. Structural characterization of n-alkyl thiol monolayers on gold by optical ellipsometry, infrared spectroscopy, and electrochemistry. *J. Am. Chem. Soc.* **109,** 3559–3568 (1987).

(6) Joseph, Y. *et al.* Self-Assembled Gold Nanoparticle/Alkanedithiol Films: Preparation, Electron Microscopy, XPS-Analysis, Charge Transport, and Vapor-Sensing Properties †. *J. Phys. Chem. B* **107,** 7406–7413 (2003).

(7) Duwez, A.-S., Pfister-Guillouzo, G., Delhalle, J. & Riga, J. Probing Organization and Structural Characteristics of Alkanethiols Adsorbed on Gold and of Model Alkane Compounds through Their Valence Electronic Structure: An Ultraviolet Photoelectron Spectroscopy Study. *J. Phys. Chem. B* **104,** 9029–9037 (2000).

(8) Dobrokhotov, V. *et al.* ZnO coated nanospring-based chemiresistors. *J. Appl. Phys.* **111,** 044311 (2012).

(9) Singh, S. Sensors—An effective approach for the detection of explosives. *J. Hazard. Mater.* **144,** 15–28 (2007).

(10) Wang, L. *et al.* High yield synthesis and lithography of silica-based nanospring mats. *Nanotechnology* **17,** S298–S303 (2006).

(11) Dasary, S. S. R., Singh, A. K., Senapati, D., Yu, H. & Ray, P. C. Gold Nanoparticle Based Label-Free SERS Probe for Ultrasensitive and Selective Detection of Trinitrotoluene. *J. Am. Chem. Soc.* **131,** 13806–13812 (2009).

(12) Goodpaster, J. V. & McGuffin, V. L. Fluorescence Quenching as an Indirect Detection Method for Nitrated Explosives. *Anal. Chem.* **73,** 2004–2011 (2001).

(13) Castner, D. G., Hinds, K. & Grainger, D. W. X-ray Photoelectron Spectroscopy Sulfur 2p Study of Organic Thiol and Disulfide Binding Interactions with Gold Surfaces. *Langmuir* **12,** 5083–5086 (1996).

(14) Watts, J. F. *An introduction to surface analysis by XPS and AES*. (J. Wiley, 2003).

(15) Libertino, S. *et al.* Layer uniformity in glucose oxidase immobilization on SiO2 surfaces. *Appl. Surf. Sci.* **253,** 9116–9123 (2007).

(16) Abdureyim, A. *et al.* Characterization of 4-mercaptohydrocynnamic acid self-assembled film on Au(111) by means of X-ray photoelectron spectroscopy. *J. Electron Spectrosc. Relat. Phenom.* **114-116,** 371–374 (2001).

(17) Moulder, J. F., Stickle, W. F., Sobol, P. E. & Bomben, K. D. *Handbook of X-ray Photoelectron Spectroscopy*. (Perkin-Elmer Corporation, Physical Electronics Division, 1995).

(18) Sadik, P. W., Pearton, S. J., Norton, D. P., Lambers, E. & Ren, F. Functionalizing Zn- and O-terminated ZnO with thiols. *J. Appl. Phys.* **101,** 104514 (2007).

(19) Kuo, F.-L., Li, Y., Solomon, M., Du, J. & Shepherd, N. D. Workfunction tuning of zinc oxide films by argon sputtering and oxygen plasma: an experimental and computational study. *J. Phys. Appl. Phys.* **45,** 065301 (2012).

(20) Heinhold, R., Williams, G. T., Cooil, S. P., Evans, D. A. & Allen, M. W. Influence of polarity and hydroxyl termination on the band bending at ZnO surfaces. *Phys. Rev. B* **88,** (2013).

(21) Islam, M. N., Ghosh, T. B., Chopra, K. L. & Acharya, H. N. XPS and X-ray diffraction studies of aluminum-doped zinc oxide transparent conducting films. *Thin Solid Films* **280,** 20–25 (1996).

(22) Powel, C. J. & Jablonski, A. *NIST Electron Inelastic-Mean -Free-Path Datbase, Version 1.2, SRD71*. (National Institute of Standards and Tectnology, 2010).

(23) Yeh, J. J. & Lindau, I. Atomic subshell photoionization cross sections and asymmetry parameters: $1 \leqslant Z \leqslant 103$. *At. Data Nucl. Data Tables* **32,** 1–155 (1985).

(24) Guglieri, C. & Chaboy, J. Characterization of the ZnO−ZnS Interface in THIOL-Capped ZnO Nanoparticles Exhibiting Anomalous Magnetic Properties. *J. Phys. Chem. C* **114,** 19629–19634 (2010).

(25) Guglieri, C. *et al.* XMCD Proof of Ferromagnetic Behavior in ZnO Nanoparticles. *J. Phys. Chem. C* **116,** 6608–6614 (2012).

(26) Guglieri, C. *et al.* Relationship between the Magnetic Properties and the Formation of a ZnS/ZnO Interface in S-Capped ZnO Nanoparticles and ZnS–ZnO Thin Films. *J. Phys. Chem. C* **117,** 12199–12209 (2013).

(27) Volkert, A. A., Subramaniam, V., Ivanov, M. R., Goodman, A. M. & Haes, A. J. Salt-Mediated Self-Assembly of Thioctic Acid on Gold Nanoparticles. *ACS Nano* **5,** 4570–4580 (2011).

(28) Schlenoff, J. B., Li, M. & Ly, H. Stability and Self-Exchange in Alkanethiol Monolayers. *J. Am. Chem. Soc.* **117,** 12528–12536 (1995).

(29) Barriet, D., Yam, C. M., Shmakova, O. E., Jamison, A. C. & Lee, T. R. 4-Mercaptophenylboronic Acid SAMs on Gold: Comparison with SAMs Derived from Thiophenol, 4-Mercaptophenol, and 4-Mercaptobenzoic Acid. *Langmuir* **23,** 8866–8875 (2007).

(30) Wells, M. *et al.* Interactions between Organized, Surface-Confined Monolayers and Vapor-Phase Probe Molecules. 9. Structure/Reactivity Relationship between Three Surface-Confined Isomers of Mercaptobenzoic Acid and Vapor-Phase Decylamine. *Langmuir* **12,** 1989–1996 (1996).

(31) Sharma, M. K. *et al.* A novel piezoelectric immunosensor for the detection of malarial Plasmodium falciparum histidine rich protein-2 antigen. *Talanta* **85,** 1812–1817 (2011).

(32) Li, Z., Niu, T., Zhang, Z., Feng, G. & Bi, S. Studies on the effect of solvents on self-assembly of thioctic acid and Mercaptohexanol on gold. *Thin Solid Films* **519,** 4225–4233 (2011).

(33) Bensebaa, F., Ellis, T. H., Badia, A. & Lennox, R. B. Thermal Treatment of *n* -Alkanethiolate Monolayers on Gold, As Observed by Infrared Spectroscopy. *Langmuir* **14,** 2361–2367 (1998).

(34) Zhang, J. *et al.* Two-Dimensional Cysteine and Cystine Cluster Networks on Au(111) Disclosed by Voltammetry and in Situ Scanning Tunneling Microscopy. *Langmuir* **16,** 7229–7237 (2000).

(35) Scudiero, L., Hipps, K. W. & Barlow, D. E. A Self-Organized Two-Dimensional Bimolecular Structure. *J. Phys. Chem. B* **107,** 2903–2909 (2003).

(36) Henrich, V. E. & Cox, P. A. *The surface science of metal oxides*. (Cambridge University Press, 1994).

(37) Göpel, W., Bauer, R. S. & Hansson, G. Ultraviolet photoemission studies of chemisorption and point defect formation on ZnO nonpolar surfaces. *Surf. Sci.* **99,** 138–156 (1980).

(38) Von Wrochem, F. Electron Structure and Charge Transport Properties of Thiols and Dithiocarbamates in Self-Assembled Monolayers. Ph.D. Thesis, University of Basel, Stuttgart, Germany, (2007).

(39) North Atlantic Treaty Organization & NATO Advanced Study Institute on Chemisorption and Reactivity on Supported Clusters and Thin Films: Towards an Understanding of Microscopic Processes in Catalysis. *Chemisorption and reactivity on supported clusters and thin films: towards an understanding of microscopic processes in catalysis*. (Kluwer Academic Publishers, 1997).

(40) Di Felice, R., Selloni, A. & Molinari, E. DFT Study of Cysteine Adsorption on Au(111). *J. Phys. Chem. B* **107,** 1151–1156 (2003).

(41) Rubloff, G. W., Lüth, H. & Grobman, W. D. Orbital energy shifts associated with chemical bonding of organic molecules on ZnO nonpolar surfaces. *Chem. Phys. Lett.* **39,** 493–496 (1976).

(42) Dobrokhotov, V. *et al.* Thermal and Optical Activation Mechanisms of Nanospring-Based Chemiresistors. *Sensors* **12,** 5608–5622 (2012).

(43) Cagnina, S., Rotureau, P., Fayet, G. & Adamo, C. The ammonium nitrate and its mechanism of decomposition in the gas phase: a theoretical study and a DFT benchmark. *Phys. Chem. Chem. Phys.* **15,** 10849 (2013).

(44) Willey, T. M. *et al.* Surface Structure and Chemical Switching of Thioctic Acid Adsorbed on Au(111) As Observed Using Near-Edge X-ray Absorption Fine Structure. *Langmuir* **20,** 4939–4944 (2004).

CHAPTER 5

Study of Cobalt Supported on Silica Nanosprings: A Fischer-Tropsch Catalyst

5.1 Introduction

The vast majority of the modern world largely relies on fossil fuels for energy.[1] However, the finite distribution of fossil energy reserves, the greenhouse gas emissions, and the global climate change are incentives for alternatives to petroleum products.[2] Fischer-Tropsch synthesis (FTS) provides a direct route with which to convert synthesis gas (syngas, i.e CO/H_2) into liquid clean fuels and other valuable chemicals. By using syngas derived from the abundant renewable biomass, transportation fuels can be produced from feedstocks instead of crude oil. The FTS process is currently commercially operated by many companies including Sasol (South Africa), PetroSA (South Africa), Shell (Malaysia, Qatar), UPM (Finland), Rentech (USA),[3] and continues to receive a renewed attention worldwide (China, Philippines, Germany, Netherlands, India, Indonesia, Australia, Mongolia, Pakistan, Canada, Spain, USA).[2] FTS is a heterogeneous catalytic process which has long been recognized as a polymerization reaction with the basic steps of (1) reactant (CO) adsorption on the surface of the catalyst, (2) chain initiation by CO dissociation followed by hydrogenation, (3) chain growth by insertion of additional CO molecules followed by hydrogenation, (4) chain termination, and (5) product desorption from the catalyst surface.[4]

Several transition metals such as Ru, Fe, Ni, Co, Rh, Pd and Pt can catalyze the FTS process, but Co and Fe are the most suitable for commercial interests. Cobalt-based catalysts are the best choice for low temperature FT processes, because of their high selectivity to high molecular weight linear paraffins, their low water-gas-shift (WGS) activity and stability toward deactivation by water.[5,6,7]

However Co is 230 times more expensive than Fe,[4] hence the use of a support in the catalyst preparation. The support plays a role of dispersion, stabilization and maintaining the strength of the active phase, and more importantly, cost reduction.[4] An ideal support should be chemically inert, mechanically and thermally stable with high fluid-accessible specific surface area, and a balanced metal-support interaction.[8] The most investigated supports for cobalt are silica, alumina, titania, and to a lesser extent, magnesia and the ordered mesoporous materials such as MCM-41 and SBA-15. The nature and the structure of the support can significantly influence the extent of reduction, morphology, adsorption, activity and selectivity properties of the active phase.[9] It was also found that the FTS catalytic behavior of cobalt-based catalysts depends on metal loading, metal dispersion, and cobalt particle size.[6,7] Using different supports and composition showed that the diameter of Co_3O_4 particles increased with the pore diameter, favoring their reducibility and leading to an enhancement in C_{5+} selectivity.[2] Silica nanosprings can meet and exceed the above stringent catalyst support criteria.

In this study, the physicochemical properties of cobalt supported on silica nanosprings (Co/NS) were characterized and the FTS catalytic performance evaluated in a micro-reactor. The results were compared to those of a conventional silica gel supported cobalt (Co/SiO_2-gel) catalyst. For optimization, the reduction states of Co/NS catalysts during activation were described.

5.2 Reforming of Syngas into Higher Alkanes using Cobalt Supported on Silica Nanosprings

5.2.1 Field Emission Scanning and Transmission Electron Microscopies (FESEM and TEM)

Figure 5.1 shows the FESEM (top panels) and TEM (lower panels) micrographs of the catalysts. The two catalysts have different morphologies. The silica gels appear rocky (Fig.5.1a) while randomly oriented nanosprings are formed from nanowires that coherently coiled (Fig.5.1b). It is the spiral structure of nanosprings that is responsible for their > 98% fluids accessibility. The cobalt particles are not well resolved on the FESEM images, particularly on nanosprings. On the contrary, the two supports and the particles can be seen on the TEM micrographs. The cobalt crystallites tend to agglomerate to form larger clusters on the silica gel support. On nanosprings, they are smaller in size and uniformly distributed on the surface. In order to measure the particle size and determine the particle size distribution, micrographs from multiple areas of each sample were taken and analyzed. The results are presented in Table 5.1.

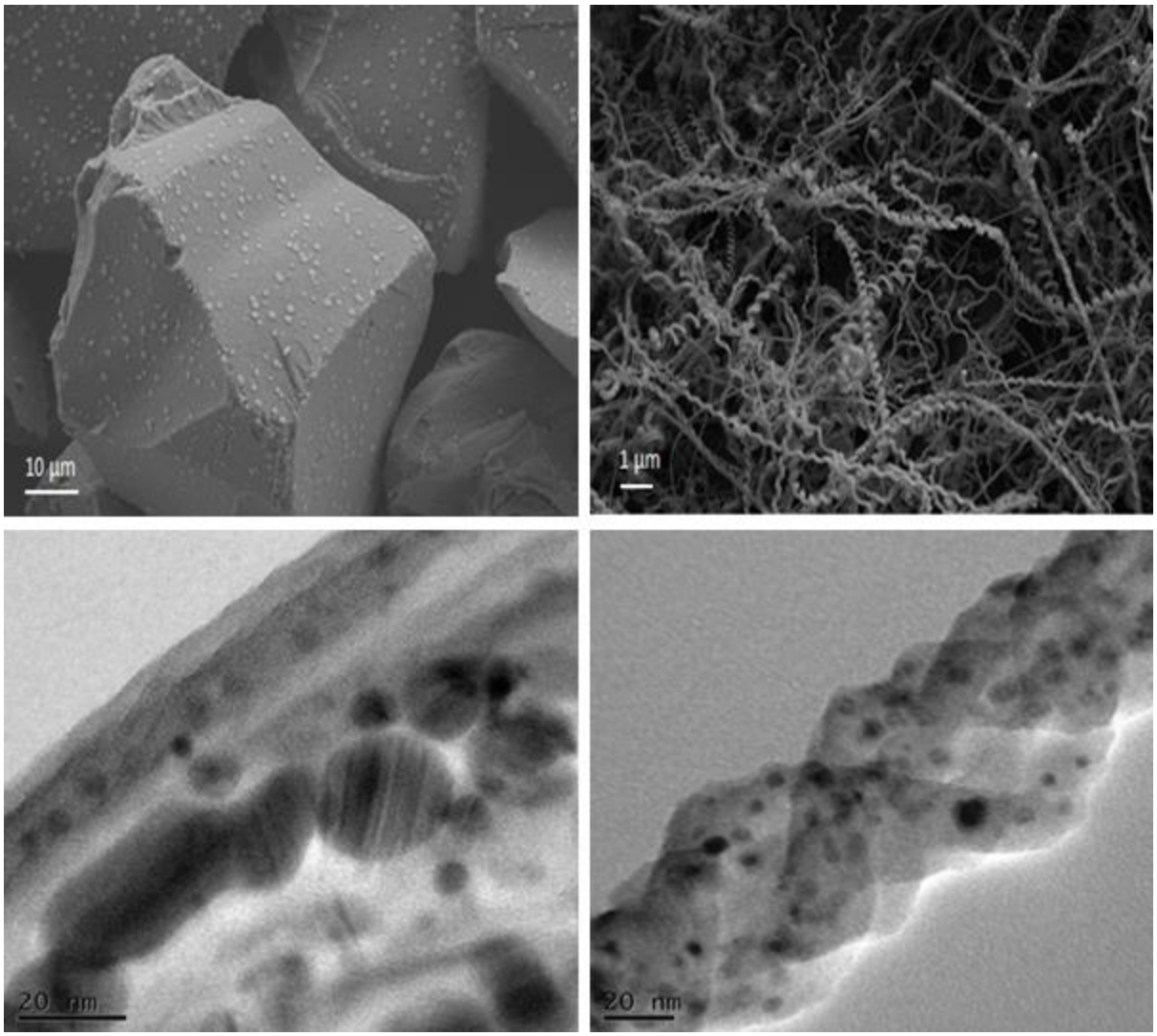

Figure 5.1 FESEM (top panels) and TEM (lower panels) of Co/SiO_2-gel (left) and Co/NS (right).

5.2.2 X-ray Powder Diffraction (XRD)

XRD patterns of the catalysts are displayed in Figure 5.2. Diffraction peaks are observed at 19.1 º, 31.3 º, 36.8 º, 44.9 º, 59.6 º, and 65.2 º for Co/SiO_2-gel and for Co/NS at 18.7 º, 38.2 º, 44.4 º, and 64.7 º. These peaks can be assigned to the Co_3O_4 spinel phase of cobalt.[5-10] The diffraction peak (440) was selected to evaluate the Co_3O_4 particle size according to the Scherrer's equation.[11] The Co_3O_4 particle sizes were 13.1 nm and 12.7 nm, respectively, for

Co/SiO_2-gel and Co/NS.

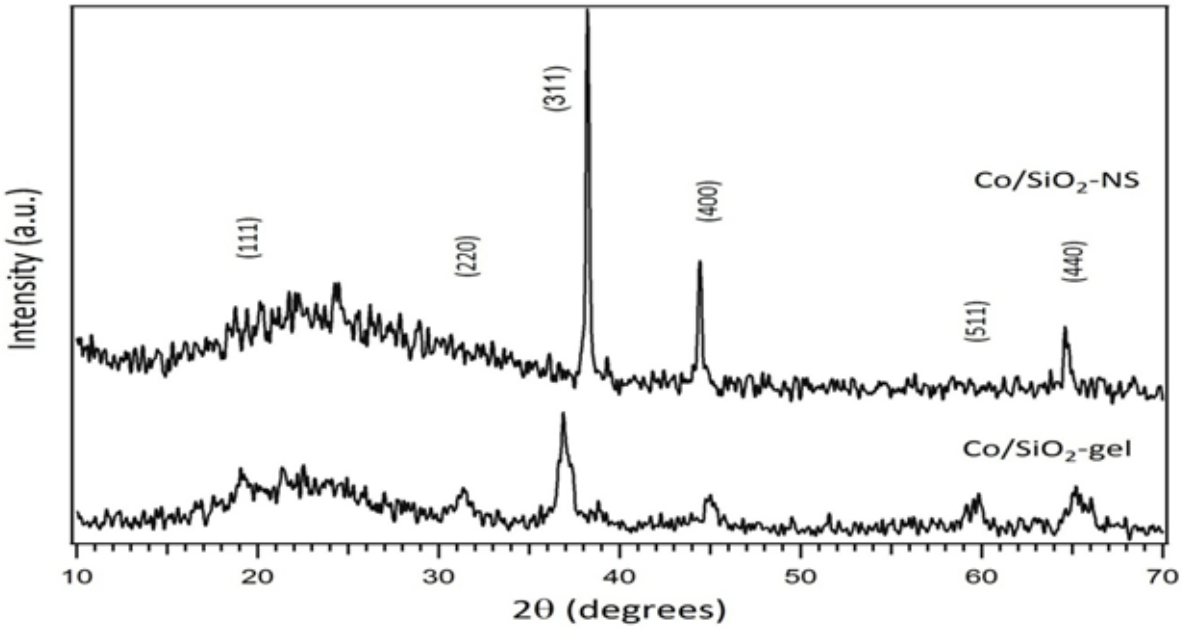

Figure 5.2 XRD patterns of Co/NS (top) and Co/SiO_2-gel (bottom).

5.2.3 Nitrogen Physisorption Measurements

The BET (Brunauer-Emmett-Teller) surface area and the pore volume data are listed in Table 5.1. The silica-gel catalyst has larger surface area and pore volume than the nanospring-based catalyst. The cobalt loading on the two catalysts supports leads to a significant decrease both in the BET surface area and the total pore volume. The decrease in the surface area and pore volume is likely to be mainly due to the blocking of the pores by cobalt species.[11] The plugging makes the pores inaccessible for nitrogen adsorption. In the case of Co/NS, it may also be the consequence of the loss of material as observed during cobalt deposition when the impregnated nanospring support is heated under hydrogen atmosphere. Table 5.1 summarizes the results for the morphological characterization. The particle sizes obtained from TEM and XRD concur very well.

Table 5.1 BET surface area, porosity, and Co_3O_4 crystallite size

Support /Catalyst	BET Surface area (m^2/g)	Pore volume (m^3)	TEM Cobalt oxide particle size (nm)	XRD Cobalt oxide particle size (nm)
Silica gel	478	0.82	-------	-------
Nanospring	329	0.62	-------	------
Co/SiO_2-gel	370	0.42	14.7	13.1
Co/NS	208	0.29	9.4	12.7

5.2.4 X-ray Photoelectron Spectroscopy (XPS)

The Co 2p core level states spectra of the two catalysts is presented in Figure 5.4. At first glance, judging by the shapes and the photoelectron binding energy positions, the two fresh catalysts are chemically different.

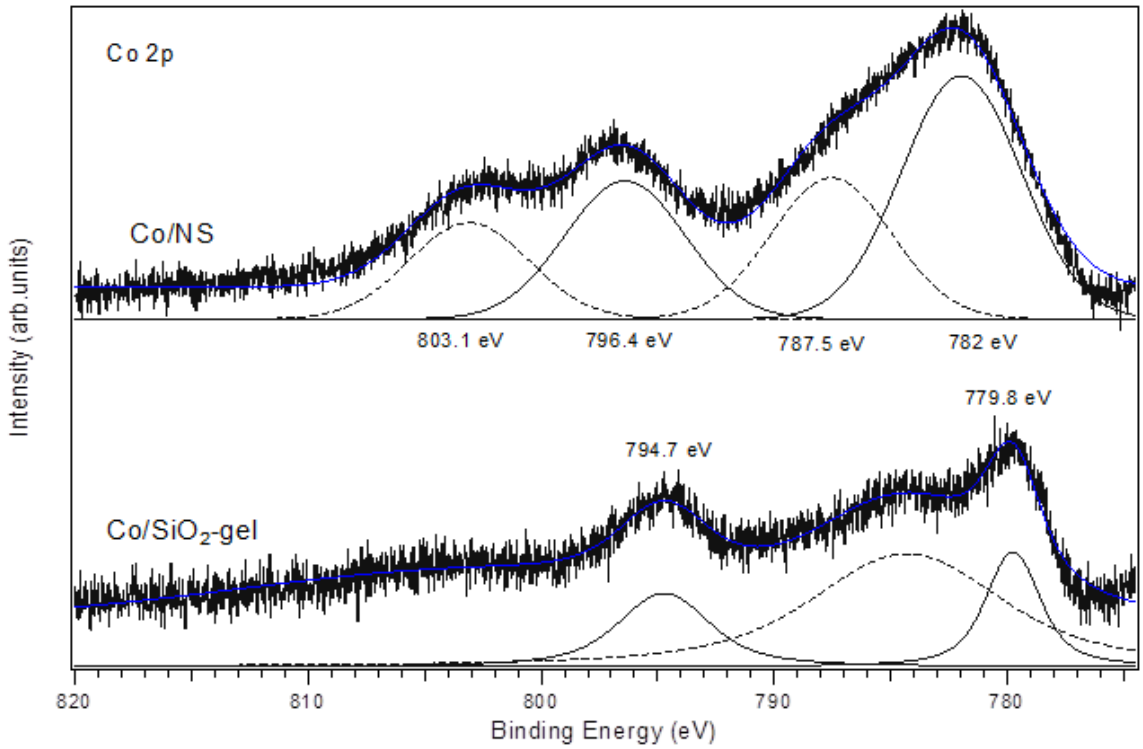

.

Figure 5.3 Co 2p core level states of Co/NS and Co/SiO_2-gel as obtained from XPS.

For Co/SiO_2-gel, the binding energy of the Co $2p_{3/2}$ core level state is 779.8 eV and a low shake-up satellite feature is observed on the higher binding energy side. Co_3O_4 is likely to be the dominant phase present at the outer surface of the grain of Co/SiO_2-gel.[11] For Co/NS, a relatively more intense shake-up satellite is observed and the position of the Co $2p_{3/2}$ peak is shifted to higher binding energy value (782 eV). These observations indicate a relatively lower cobalt loading and also that in addition of the predominant Co_3O_4 spinel phase, some concentration of Co^{2+} species could be present.[12]

XRD and XPS analyses show that as prepared both catalysts are cobalt oxides, but they will need to be metallic cobalt for Fisher-Tropsch synthesis.

5.2.5 Fisher-Tropsch Synthesis (FTS)

The GC-MS results plotted in Figure 5.4 shows that both catalysts have similar select C_{5+} selectivity favoring lighter components, even though Co/NS had 75 times less gravimetric cobalt content than Co/SiO_2-gel.

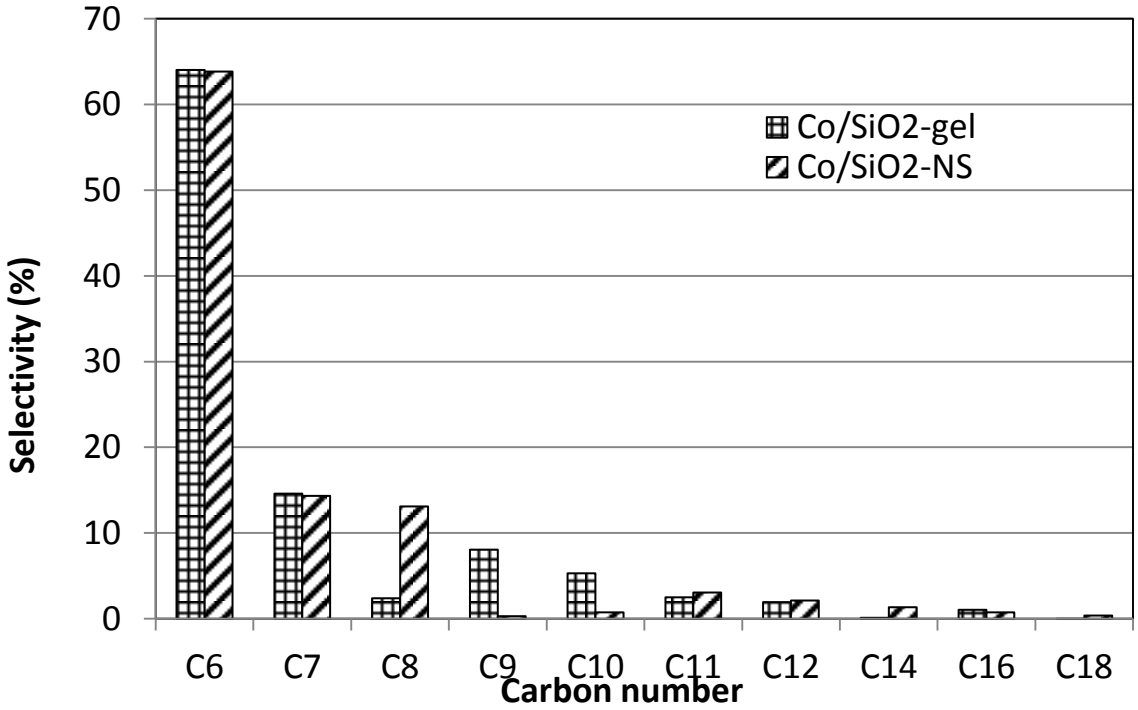

Figure 5.4 Distribution of n-alkanes (C_6-C_{18}) for Co/SiO_2 and Co/NS catalysts.

The higher selectivity of Co/NS, when normalized to the cobalt content, may be due to the higher dispersion of cobalt nanoparticles as revealed by TEM and the gas-accessible specific surface area.

Table 5.2 CO conversion and product selectivity of Co/SiO_2-gel and Co/SiO_2-NS catalysts

Time period (h)	CO Conversion (%)		FTS Activity (g CO/g Cat./h)		WGS Activity (g CO_2/g Cat./h)		Selectivity CH_4/n-alkanes (C_6-C_{18})	
	Gel-	NS-	Gel-	NS-	Gel-	NS-	Gel-	NS-
50-60	45.60	58.54	3.13	16.09	----	0.01	0.01	0.09
60-70	50.16	66.41	3.45	18.25	----	0.02	0.01	0.09
70-80	84.62	31.24	5.81	8.58	0.01	0.03	0.02	0.14
80-90	50.83	24.69	3.49	6.79	0.01	0.02	0.01	0.15
90-100	35.73	26.83	2.45	7.37	0.01	0.01	0.01	0.15
100-110	43.91	24.47	3.02	6.73	0.01	0.02	0.01	0.13
110-120	24.31	20.64	2.37	5.62	----	0.02	0.01	0.14

Table 5.2 shows that for both catalysts exhibited an initial increase in the CO conversion (%) to a maximum (66.41 % for Co/NS and 84.62 % for Co/SiO_2-gel), followed by a decrease. Co/NS started with a higher CO conversion, which dropped after 70 h and became lower than that of Co/SiO_2-gel, though it also dropped after 80 h. FTS activity was reported as CO conversion rate (g CO/g Cat./h) and had the same trend as the CO conversion. There are many reasons that could cause the drop the activity of a catalyst: (1) sintering of cobalt nanoparticles, (2) formation of cobalt silicates that are not active for FTS, and (3) the filling

of the support pores with hydrocarbons (carburization) which prevents further CO hydrogenation by blocking the active cobalt sites.[8] The highest FTS activities were 18.25 and 8.58, for Co/NS and Co/SiO_2-gel, respectively. The cobalt catalyst activity for FTS strongly depends on the cobalt particle size and the catalyst reducibility.[5] It was suspected that the Co/NS catalyst was not completely reduced prior to the FT reaction (see section 5.26). The good FTS performance of Co/NS catalyst despite its incomplete reduction may be a result of the accessible surface area that contributed to its activity. However, the nanospring support also had a relatively higher WGS activity (Table 5.3), albeit only slightly relative to Co/SiO_2-gel. This may be a result of a relatively higher water partial pressure for Co/NS, due to its higher selectivity.[13] Additionally, a higher ratio of CH_4 to C_6-C_{18} n-alkanes was observed for Co/NS, which is attributable to its smaller cobalt particle size. The larger cobalt particles can facilitate the dissociative adsorption of CO, which leads to the $–CH_2-$ fragment formation for chain growth; thus, the larger particles are more selective to heavier molecular weight hydrocarbons, whilst the smaller particles are selective to methane.[5,13,14]

5.2.6 Hydrogen-Temperature Programmed Reduction (H_2-TPR)

To better understand the drop in the FTS activity, hydrogen-temperature programmed reduction was performed to access the reducibility of the metal on the supports.[15] Figure 5.5 shows the H_2-TPR profiles for the catalysts. The reduction peaks are observed at 271 ºC and 325 ºC for Co/SiO_2-gel, and 391 ºC and 603 ºC for Co/NS.

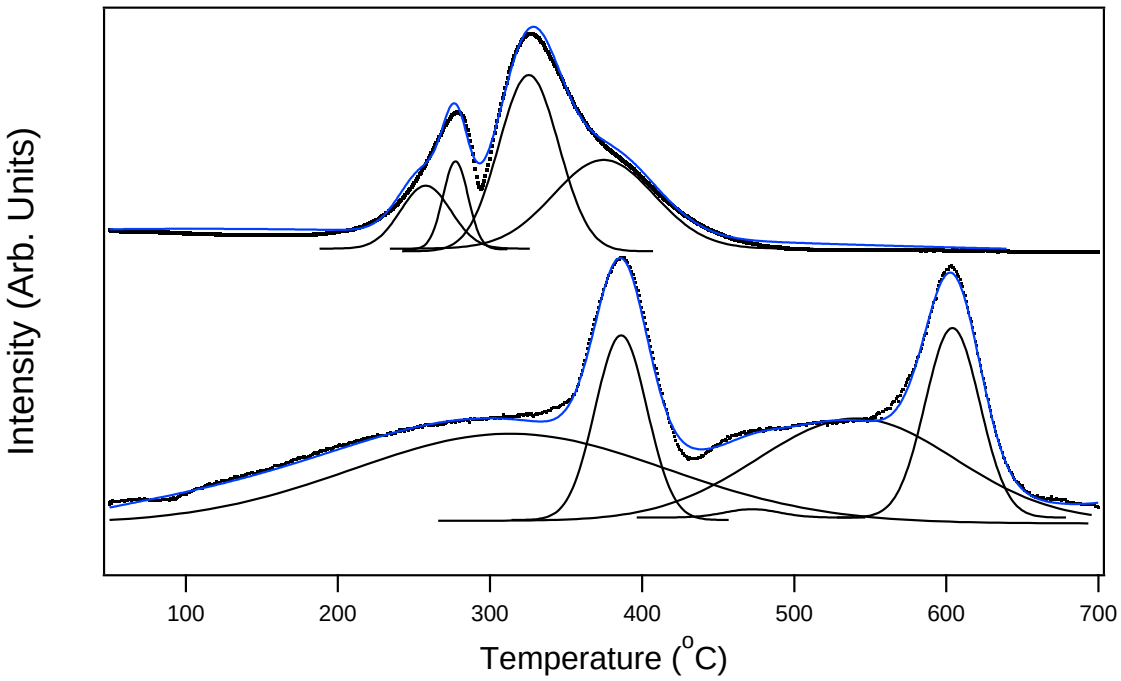

Figure 5.5 H_2-TPR profiles for Co/SiO_2-gel (top) and Co/NS (bottom).

The occurrence of two reduction peaks is indicative of the presence of two reducible cobalt species in the catalysts. The first peaks are generally ascribed to the first reduction step from Co_3O_4 to CoO and the second peaks to the reduction of CoO to Co. If this assignment holds for Co/SiO_2-gel, for Co/NS, the large separation between the two maxima (more than 100 ºC) suggests that they are rather a consequence of the reduction of cobalt oxides which have different interaction strengths with the nanospring.[16] This interaction would depend on the size of the metal oxide. Larger particles which interact less with the support would be reduced first at the low-temperature stage. The second reduction stage at higher temperature is associated with the presence of small cobalt oxide particles deposited in low diameter pores which are harder to reduce because of the difficulty to eliminate the reduction water.[5,16] The size heterogeneity as demonstrated by the TEM analysis and the low pore volume of 0.29 cm^3/g as determined from nitrogen physisorption (BET measurements)[8] support this point. The reduction of Co/NS will be further discussed in the next section. The lower

reduction temperatures for Co/SiO_2-gel may be indicative of the presence of larger cobalt oxide crystallite after calcination on the silica gel supports with larger average pore size, as shown by the TEM and the nitrogen physisorption. Moreover, for Co/NS, both reduction peaks have lower intensity, which is likely due to the small amount of Co in the nanospring samples. Note, a temperature of 400 ºC was used for activation of both catalysts prior to the FTS evaluation and is insufficient to fully reduce the Co/NS, which likely explain the quicker drop in its activity.

5.2.7 Chemical Characterization of Co/NS FT Catalyst

XPS was performed on the spent Co/NS catalyst. Figure 5.6 shows the Co 2p core level states.

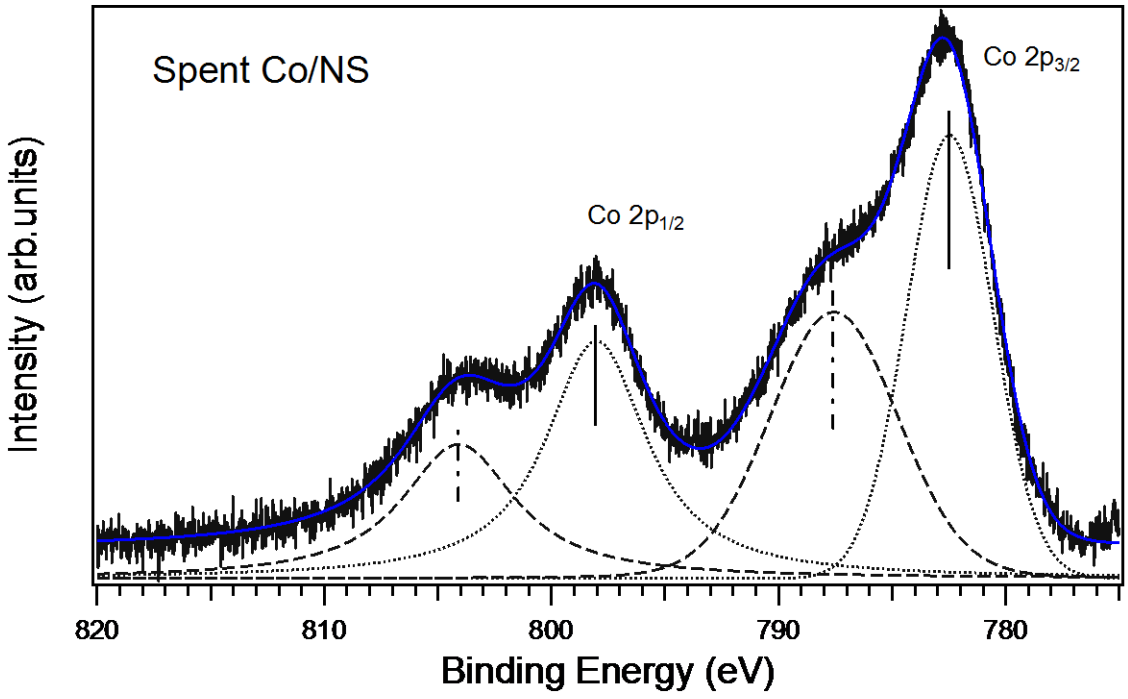

Figure 5.6 Co 2p core level states of a spent Co/NS catalyst as obtained from XPS.

Even though the experiment was not carried out *in situ*, with the possibility of cobalt re-oxidation when exposed to air, the intense shake-up satellite relative to the unreduced sample (Fig.5.3) is an indication of the abundance of cobalt II oxide (CoO) in the spent catalyst. This observation confirms that Co/NS was not fully reduced to metallic cobalt after thermal activation at 400 ºC, which is consistent with the H_2-TPR results. These findings were the real motivation to further study the reduction state of Co/NS, using *in situ* XPS.

5.3 XPS Study of Cobalt Supported on Silica Nanosprings during Reduction

5.3.1 Characterization of the Co/NS Starting Catalyst

The average Co_3O_4 particle size, as measured on TEM micrographs is 9.4±2 nm (Fig.5.1, Table 5.1). Figure 5.7 shows the particle size distribution, where it can be seen that the some particles can be as large as 15 nm.

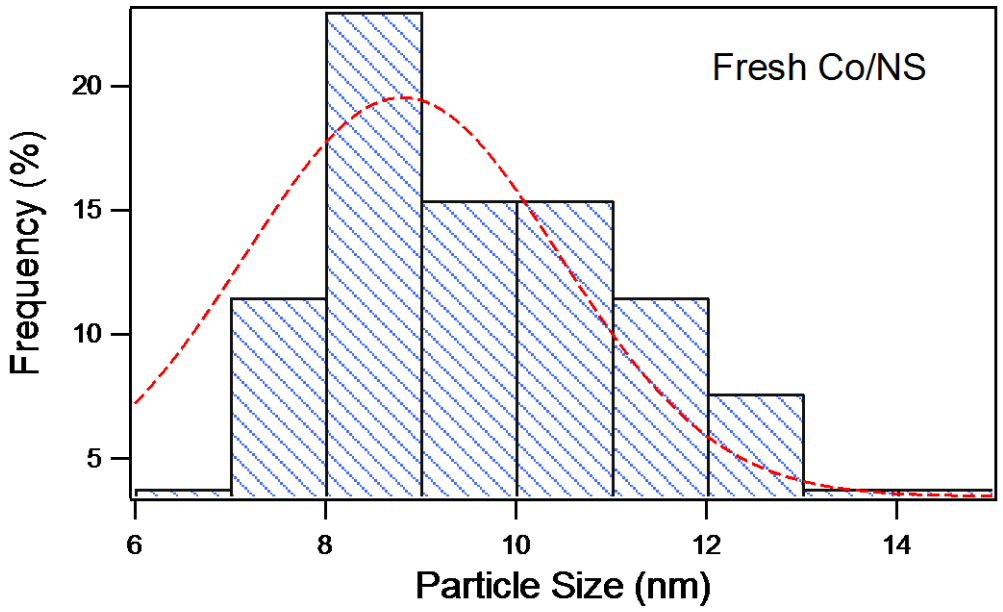

Figure 5.7 Fresh Co/NS catalyst particle size distribution.

Figure 5.8 shows the Co 2p core level of the unreduced catalyst as obtained from XPS. The deconvolution yielded 70 % Co^{3+} (octahedral) and 30 % Co^{2+} (tetrahedral) at binding energies of 779.9 eV and 782 eV, respectively. Within experimental errors this composition is consistent with the Co_3O_4 spinel phase.

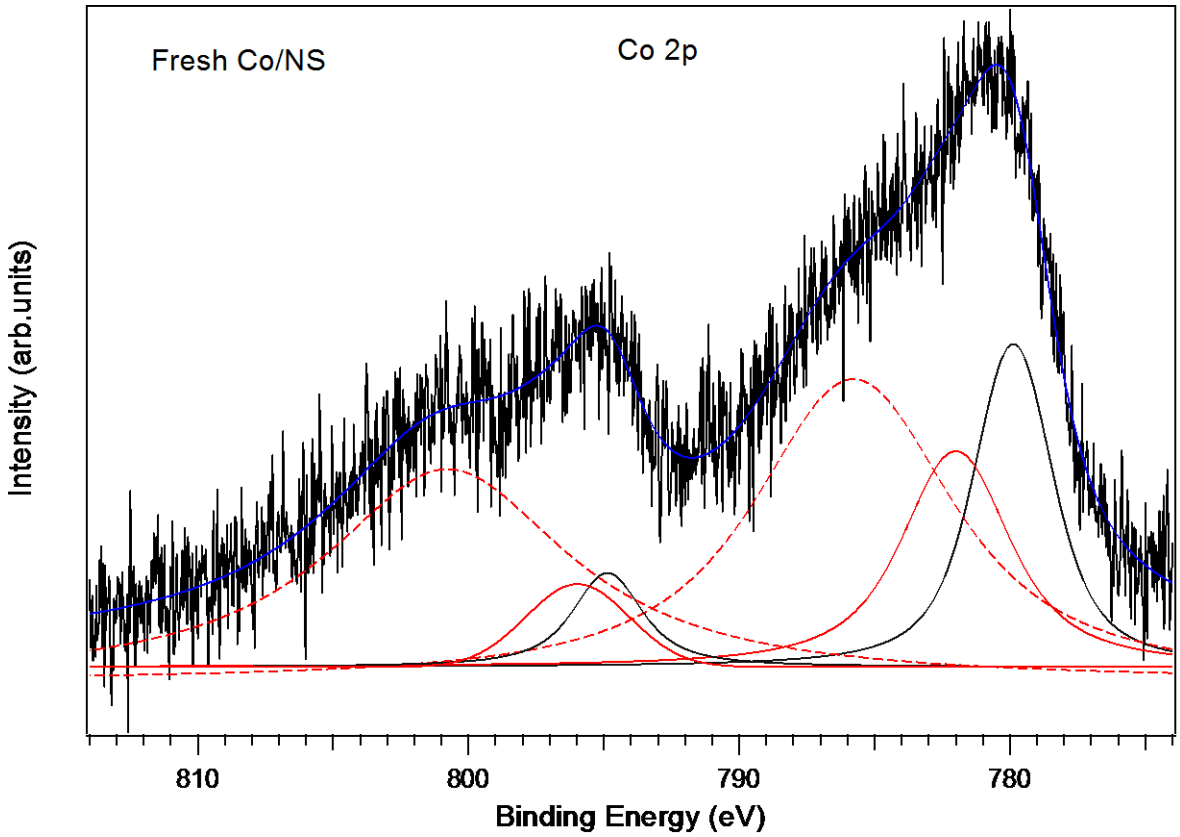

Figure 5.8 Co 2p core level states from the starting Co/NS catalyst.

The strong and broad features at higher binding energies correspond to the shake-up satellites of the Co^{2+}. XPS was also used to attain information about the dispersion of Co_3O_4 spinel. For this purpose, XPS core levels states integrated and corrected with atomic sensitivity factors obtained from the literature [17-18] allowed us to estimate the Co/Si ratio of 0.07. This value implies a high dispersion of small Co_3O_4 particles over the surface of the silica nanospring support, in good agreement with the TEM micrograph.

5.3.2 XPS Study of in situ reduction of Co/NS

Reduction consisted of timed exposures of the sample to $1.0x10^{-6}$ Torr of H_2 at 385°C, and each time allowing the sample to cool to room temperature. For the reduction at 680°C and 10Torr of hydrogen, a separate chamber was built where the sample was reduced and then taken while still under vacuum to the UHV chamber for XPS analysis. The spectra were acquired after each exposure. Shown in Fig.5.9 are the Co 2p core level states for the first set of experiments carried out at 385 ºC and $1.0x10^{-6}$ Torr of H_2.

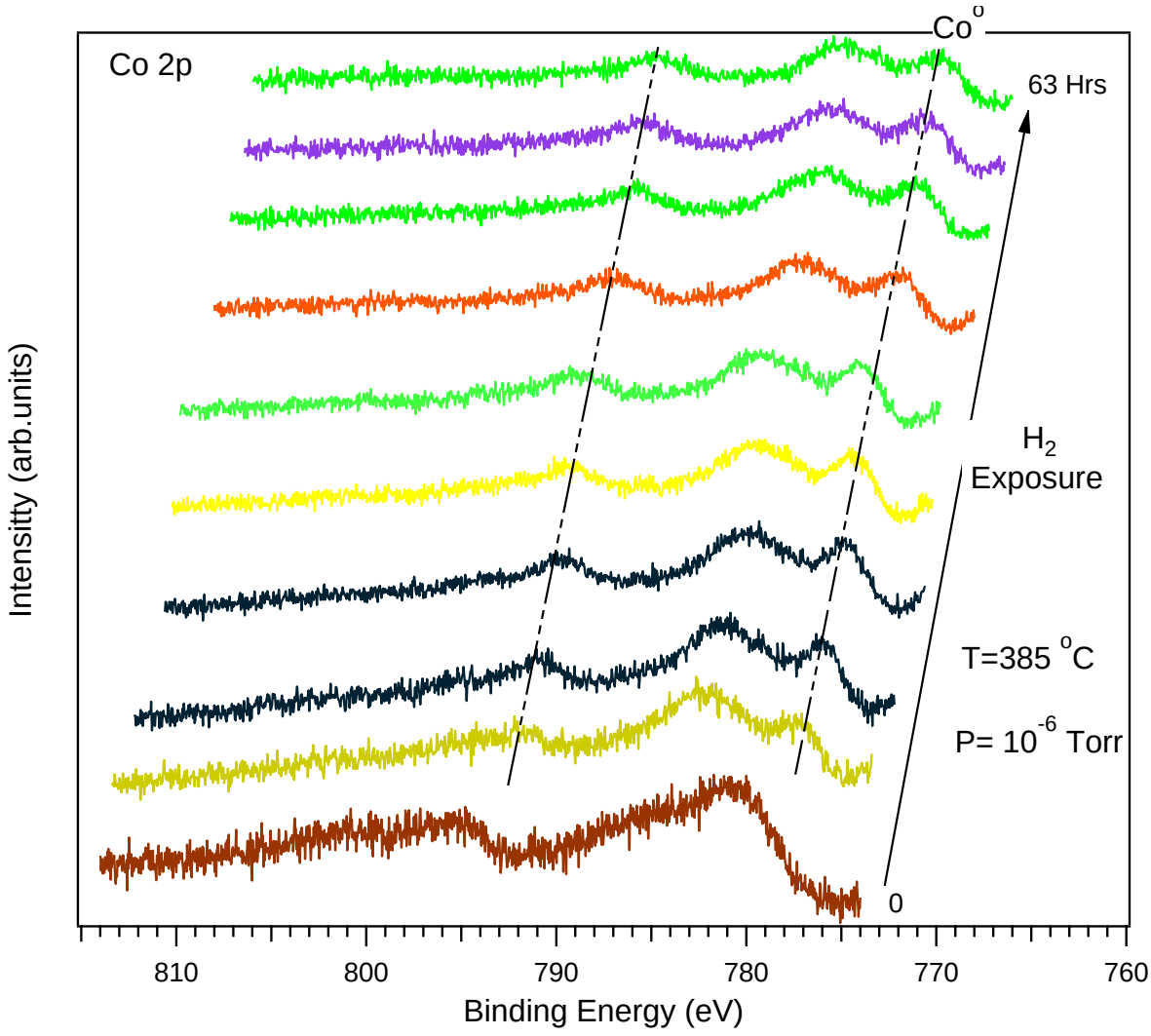

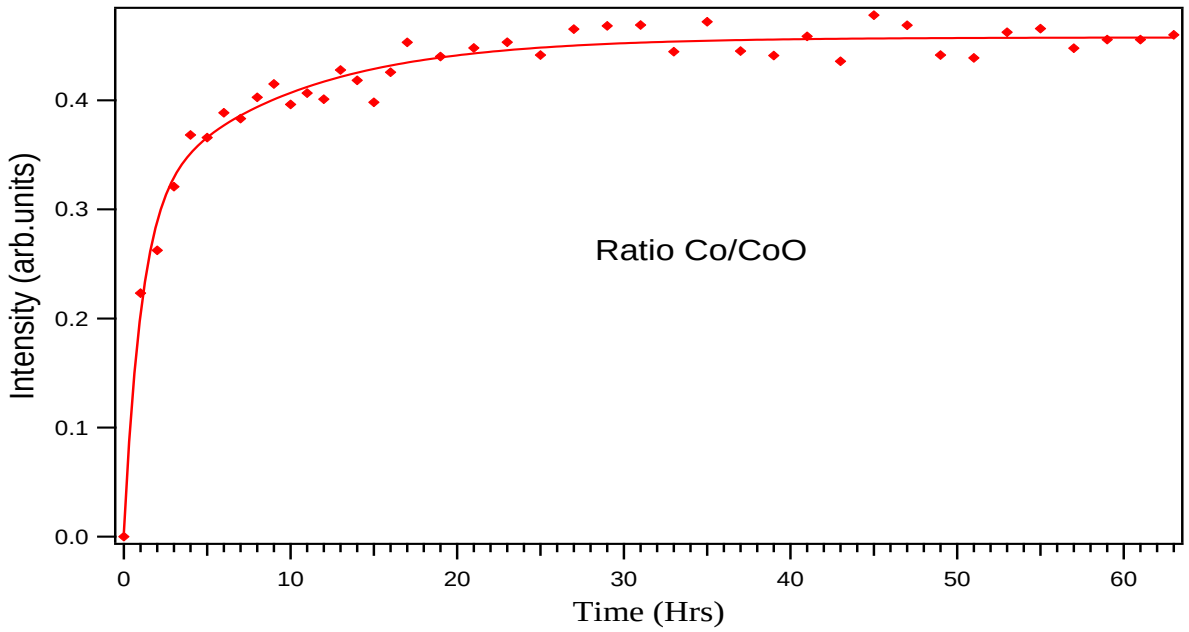

Figure 5.9 XPS Co 2p core level states of Co/NS (top) and Co/CoO ratio (bottom) during reduction, the solid line is a guide to the eye.

Starting from Co_3O_4, CoO and Co^0 are gradually formed as the reduction time increases. Co^0 corresponds to the shoulder at ~778 eV while the broad feature at ~782.2 eV is associated with CoO. The Co/CoO ratio shows that the amount of Co increases while that of CoO decreases. This is evidence of the reduction pathway Co_3O_4 →CoO →Co on the surface of the catalyst. The reduction saturates after ~20 hours at the value of 41.4 %. Table 5.4 summarizes the composition of the catalyst as well as the binding energies before and after repeated hydrogen thermal cycles, for a total exposure time of 63 hours.

Table 5.3 Analysis of the Co 2p core level states of Co/NS before and after reduction.

Reduction	Co^{3+}(octahedral)	Co^{2+}(tetrahedral)	Co^{2+} (octahedral)	Co (metal)
Unreduced	70 % (779.9 eV)	30 % (782 eV)	---------	----------
T_R = 385 ^oC (63 Hrs)	16.5 % (780.8 eV)	----------	42.1 % (783.2 eV)	41.4 % (777.8 eV)

The presence of contributions from the three phases of cobalt attests that the two reduction steps (Co_3O_4 → CoO and CoO →Co) are concurrent. The reduction proceeds through the following scheme:

$Co_3O_4 + H_2 \rightarrow 3CoO + H_2O$ (5.1)

$3CoO + 3H_2 \rightarrow 3Co + 3H_2O$ (5.2)

It can be noticed that the second step (CoO →Co) is more difficult as it requires hydrogen to diffuse through metallic Co surface layer, and produces more water, the elimination of which is necessary to see a bigger increase in the reduction rate.

The presence of metallic cobalt was also monitored by the XPS valence band, where metallic Co would induce a sharp Fermi edge due to its unfilled d band. The sharper the Fermi edge the more metallic the sample. The XPS valence bands spectra recorded before and during reduction are displayed in Fig.5.10.

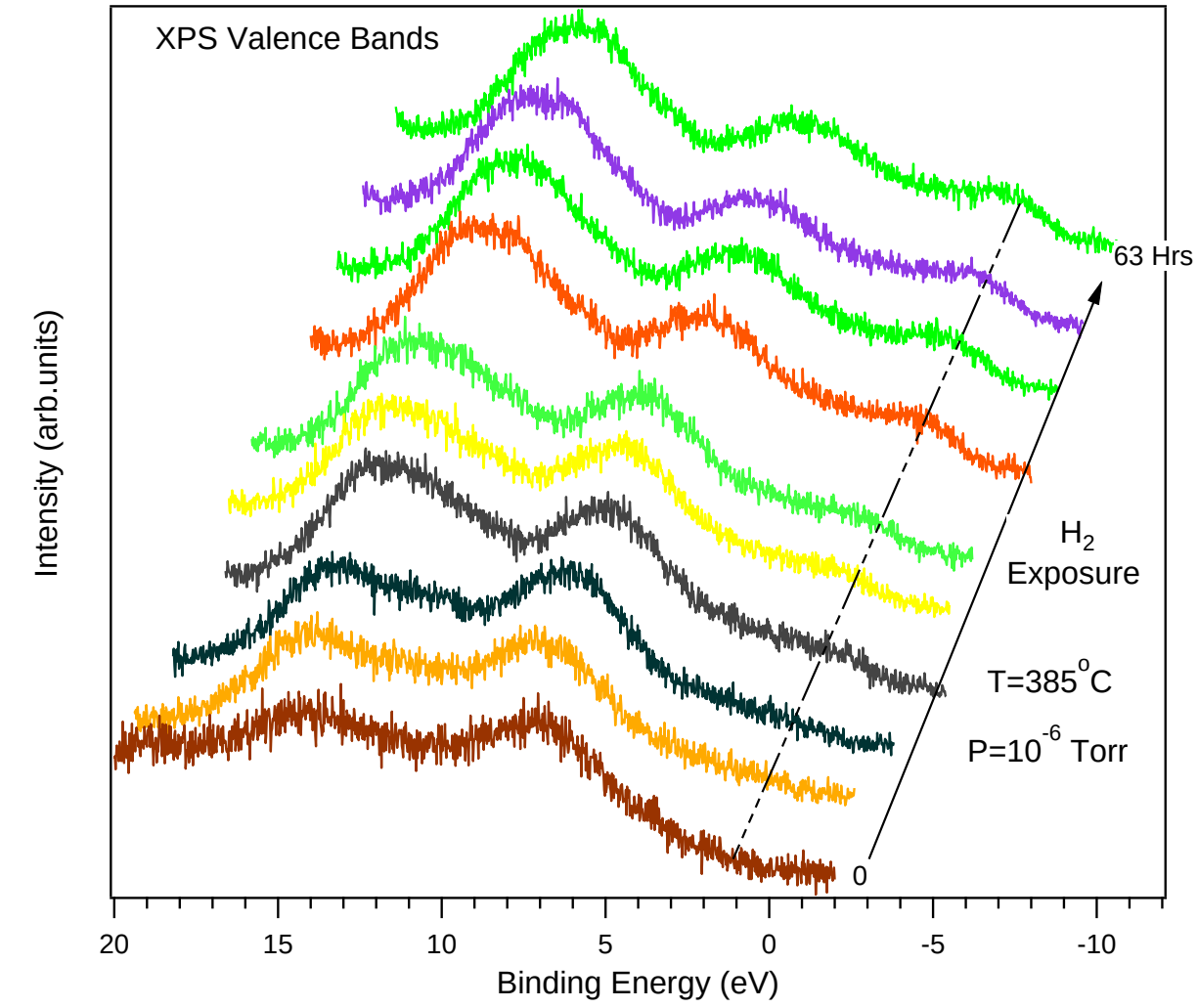
XPS Valence Bands
Intensity (arb.units)
63 Hrs
0
H2
Exposure
T=385°C
P=10-6 Torr
20
15
10
5
0
-5
-10
Binding Energy (eV)

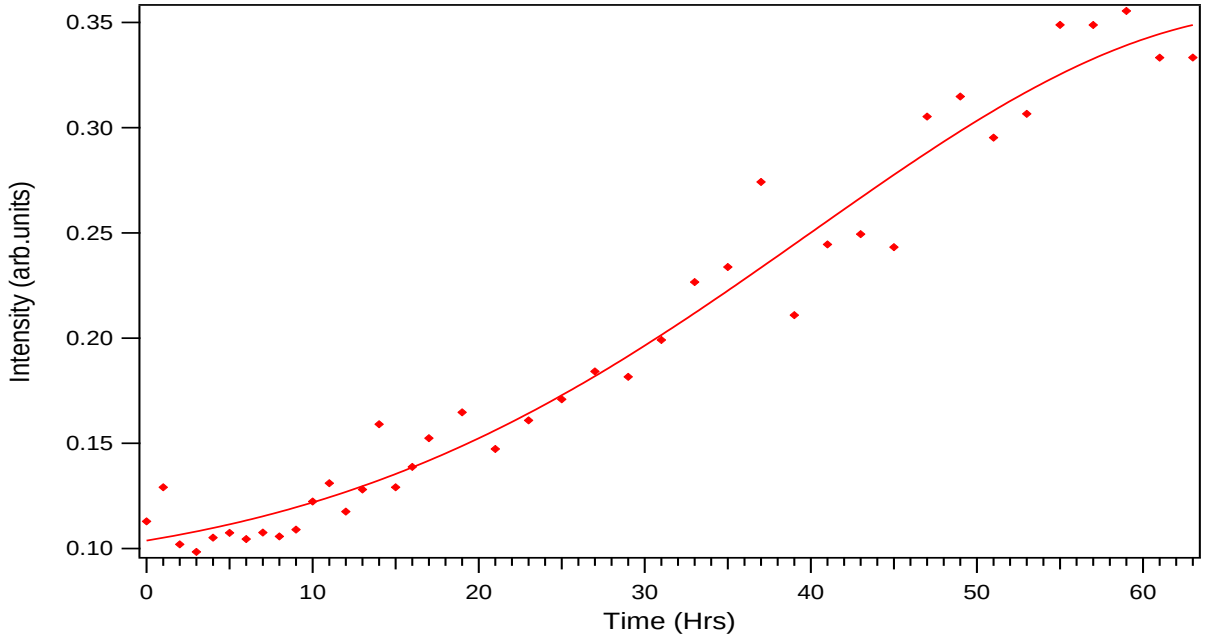
Intensity (arb.units)
0.35
0.30
0.25
0.20
0.15
0.10
0
10
20
30
40
50
60
Time (Hrs)

Figure 5.10 Valence bands spectra of Co/NS during reduction as obtained from XPS (top) and XPS integrals near the Fermi level.

Unlike the Co 2p core level where the metallic cobalt appeared with just the first hydrogen thermal cycle, it takes more H_2 exposures to increase the density of states at the Fermi level, which can then appear in the XPS valence band spectrum. The two features in the upper valence band associated with the oxides are still intact, which is yet additional proof of an incomplete reduction. The XPS findings agree well with the H_2-TPR analysis that higher activation temperature is needed to fully reduced Co/NS catalysts. We hypothesized that there is heat loss through convection and radiation modes along the nanospring. The following calculation was performed to test this hypothesis:

Consider a silica nanowire that is heated from its base. Heat is dissipated from the nanowire surface by convective and radiative modes of transfer. It is assumed that the system is in steady-state conditions, and therefore time will not be an independent variable, and a one-dimensional conduction through the wire. A thermal energy balance on a segment Δz of the wire can be written as:

$$-\Delta(q_{cond}) = q_{conv} + q_{rad} \tag{5.3}$$

q_{cond} is expressed by Fourier's law of heat conduction as $q_{cond} = -kAdT/dz$, where k is the thermal conductivity of the material, A the area normal to the direction of heat transfer, and dT/dz the temperature gradient. The rate of convection heat transfer q_{conv} is expressed by Newton's law of cooling as $q_{conv} = hA_s(T_s - T_\infty)$, where h is the convection heat transfer coefficient, A_s is the surface area through which convection heat transfer takes place, T_s is the surface temperature and T_∞ is the temperature of the fluid (surrounding gas) sufficiently far from the surface.[19] When there is radiation exchange between a small surface of

emissivity ε and surface area A_s at a temperature T_s and a much larger surface at temperature T_{surf} that surrounds the smaller one, and if the surface is one of which the absorptivity and the emissivity are equal, then the net rate of radiation heat transfer q_{rad} is given by $q_{rad} = \varepsilon\sigma A_s (T_s^4 - T_{surf}^4)$, where σ is the Stefan – Boltzmann constant.[20] Equation (5.3) can thus be rewritten, and upon dividing by RΔz and taking the limit as Δz approaches zero yields the following relationship:

$$\frac{d}{dz}\left(k\frac{dT}{dz}\right) = \frac{2h}{R}(T - T_a) + \frac{2\varepsilon\sigma}{R}(T^4 - T_a^4) \tag{5.4}$$

,where R is the radius of the wire. $T_\infty \approx T_{surf} = T_a$, h, k and ε correspond to average values as they are in general temperature dependent. Equation (5.4) can be transformed to:

$$\frac{d^2T}{dz^2} = \frac{2h}{Rk}(T - T_a) + \frac{2\varepsilon\sigma}{Rk}(T^4 - T_a^4) \tag{5.5}$$

This is a second order differential equation with the boundary conditions at the two ends of the wire: $T = T_h$ at $z = 0$ and $dT/dz = 0$ at $z = L$, where T_h is the temperature of the heater and L is the length of the wire. And in order to make the variables dimensionless, define $\theta = T/T_h$, $\theta_a = T_a/T_h$, and $\rho = z/L$. Then equation (5.5) becomes:

$$\left(\frac{R}{L}\right)^2 \frac{d^2\theta}{d\rho^2} = \frac{2Rh}{k}(\theta - \theta_a) + \frac{2R\varepsilon\sigma T_h^3}{k}(\theta^4 - \theta_a^4) \tag{5.6}$$

The following parameters of practical importance can be defined:[21]

α = R/L = (0.5x cross-sectional area) / (external surface area)

$\beta = Rh/k$ = averaged Biot number = (heat transfer by convection) / (heat transfer by conduction)

$\Phi = h/(\varepsilon\sigma T_h^3)$ = Stanton number / Thring number = (heat transfer by convection) / (heat transfer by radiation)

$\gamma = \beta/\Phi$ = (heat transfer by radiation) / (heat transfer by conduction)

Equation (5.6) is simplified to:

$$\alpha^2 \frac{d^2\theta}{d\rho^2} = 2\beta(\theta - \theta_a) + 2\gamma(\theta^4 - \theta_a^4) \tag{5.7}$$

, with boundary conditions:

$\theta = 1$ at $\rho = 0$ (5.8)

$d\theta/d\rho = 0$ at $\rho = 1$ (5.9)

This nonlinear second order differential equation can only be solved by numerical methods. The solution for a nanowire can be extended to a nanospring by changing L to L_{spring} which is given by:

$$L_{spring} = \frac{L_{free}}{S}\sqrt{S^2 + (\pi D)^2} + 2\pi D \tag{5.10}$$

, where L_{spring} is the total length of wire needed to make a spring, L_{free} is the spring free length; S is the coil pitch, and D the diameter of the coil.

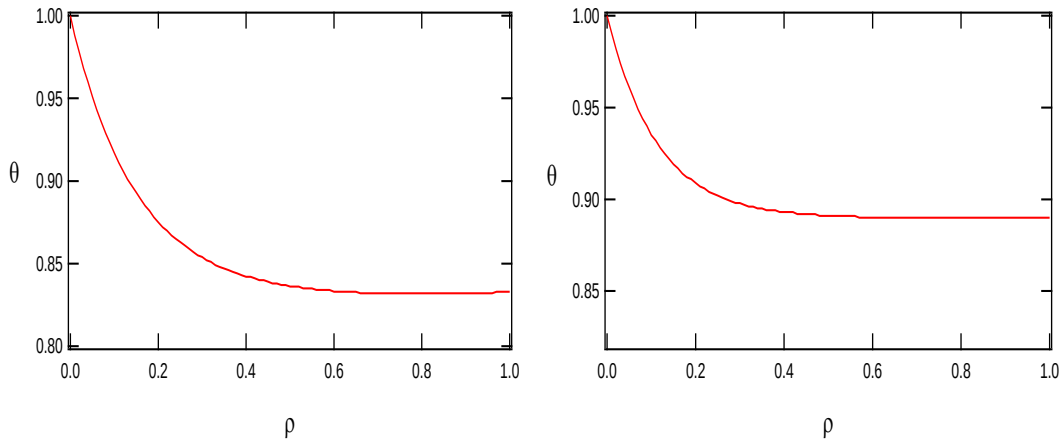

Figure 5.11 Temperature profiles as determined from numerical analysis along two nanosprings both of 60 μm free length; the wire diameter, the coil pitch and the coil diameter are 28, 268, 230 nm (left panel), and 114, 278, 435 nm (right panel).

The differential equation was first separated in two simultaneous first order differential equations, and then the resulting system was solved using the Runge-Kutta fourth order (RK4) method programmed in Mathcad. The heat transfer coefficients used are $\varepsilon = 0.7$, $h = 30$ W/m^2.K, and $k = 1.3$ W/m.K which were all taken from literature.[22] The structural parameters of nanosprings were measured directly on TEM images. The temperature profiles in Fig.5.11 show that the nanospring temperature decreases at a distance farther away from the heat source. For instance, if the heater is at 500℃, along the nanospring the temperature can drop by ~100 ℃ from the base to the surface. This may be one of the reasons why nanospring-supported metal catalysts require higher activation temperatures to be reduced in comparison to their conventional counterparts. With these findings, in order to reduce Co/NS catalysts at higher temperature and pressure, there was a need to build a separate reduction chamber. The UHV chamber had the limitations of the heating device and the hydrogen pressure which can be damaging for the pumping systems if too high. The new reactor that was built was equipped with a heat shield made of a thin stainless foil to reflect

the heat back to the sample. The retractable and movable sample holder was equipped with a gate valve that allows us to transfer the reduced sample under vacuum from the reactor to the UHV chamber for XPS analysis.

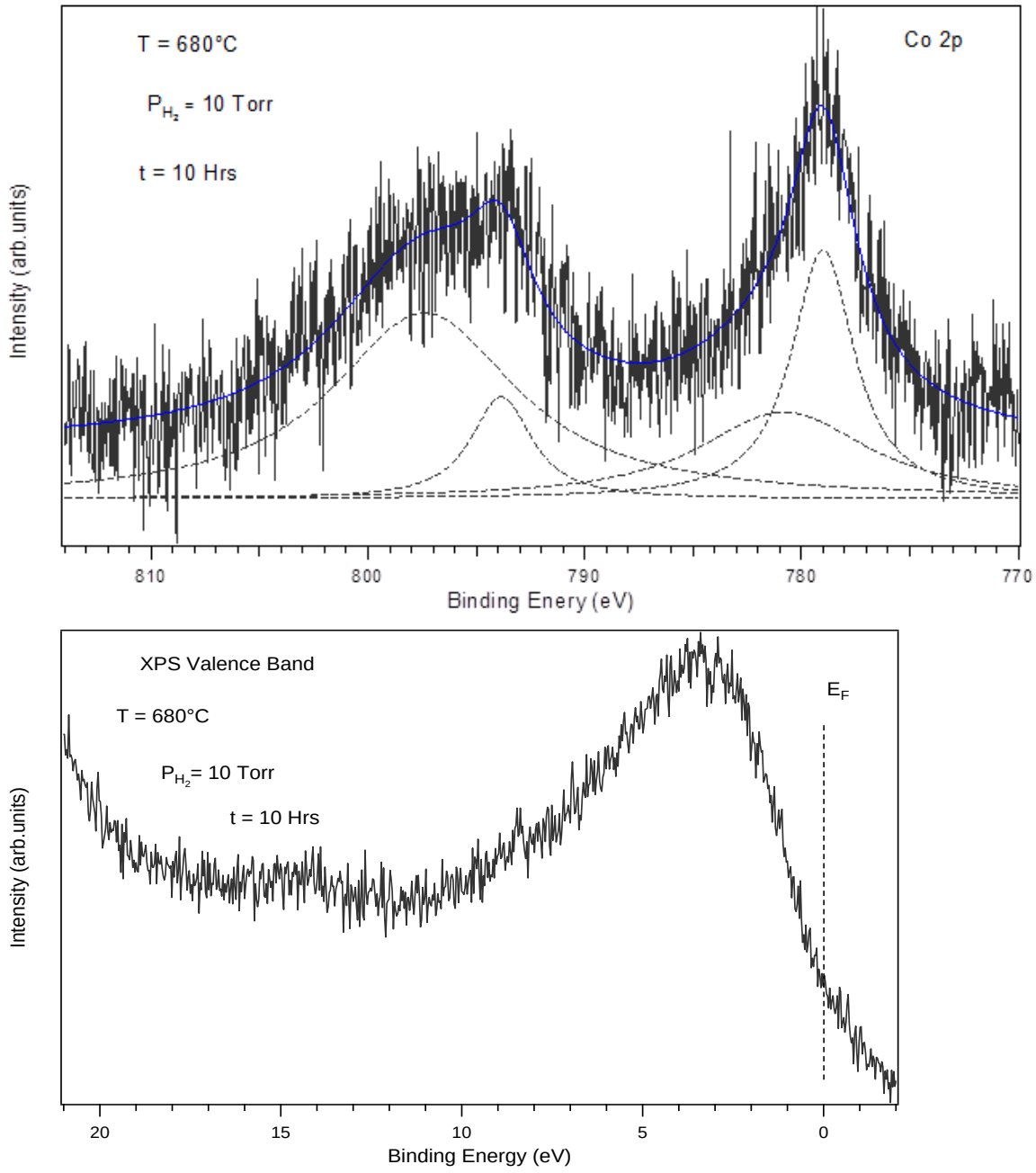

Figure 5.12 Co 2p core level states (top) and valence band (bottom) spectra as obtained from XPS for Co/NS reduced for 10 hours at 10 Torr of hydrogen at 680 ºC.

We chose 680 ºC to factor in the heat loss discussed above. The Co $2p_{3/2}$ core level state, though noisy (lower Co loading), is characteristic of metallic cobalt. The more convincing evidence of the full reduction is the valence band spectrum Fig.5.12 (bottom), where the partially filled d-band of Co is prominent and intersects the Fermi level. Moreover, the absence of the two peaks at higher binding energies (Fig. 5.10) associated with oxides supports this conclusion. The complete reduction implies the absence of cobalt silicates on the surface. Cobalt silicates overlap with cobalt (II) oxides in the Co 2p core level states, which makes the distinction between the two difficult.[22-23] In order to look for some changes in the morphology of the particles, even though metallic cobalt is very sensitive to air, right after XPS experiments TEM was performed on the sample (Fig.5.13). The average particle size was found to be 3.4± 0.2 nm. Compared to the initial particle size, there was a decrease by more than a half. This indicates that there is no coalescence (sintering) of particles during the reduction.

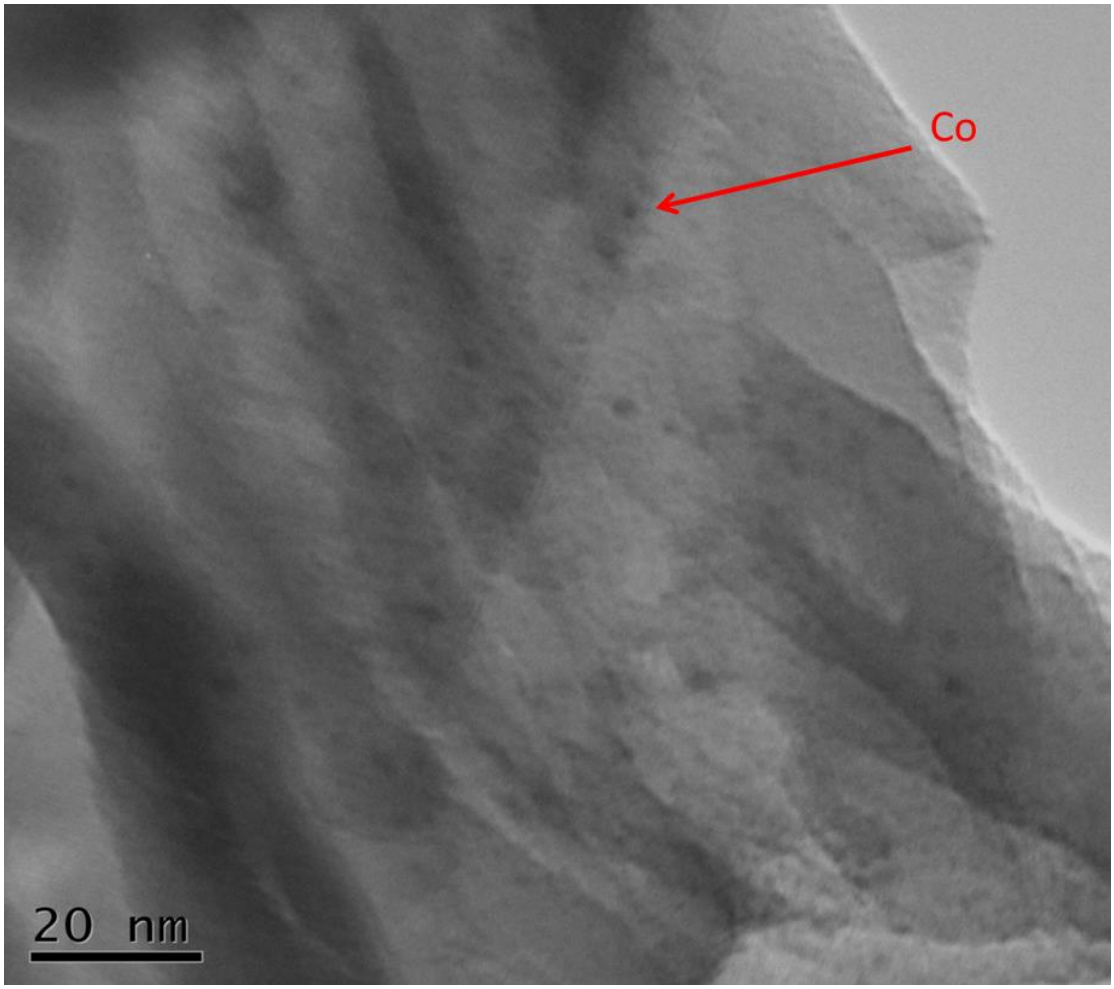

Figure 5.13 TEM micrograph of a selected area of Co/NS catalyst after reduction.

Depicted in Fig.5.14 is the proposed reduction mechanism for Co/NS catalysts. Cobalt oxide nanoparticles, regardless of their size, are reduced from top down. The outermost layers are reduced through reaction with hydrogen, forming first CoO and then Co. Additional hydrogen diffusing into the structure reduces the subsurface Co_3O_4 to CoO, and then CoO to Co. The reduction rate of the innermost layers is relatively slower due to various factors such as hydrogen diffusion rate, water elimination, and the size of the nanoparticles. As the

reduction time increases, with sufficient activation conditions the remaining CoO can ultimately be reduced to Co.

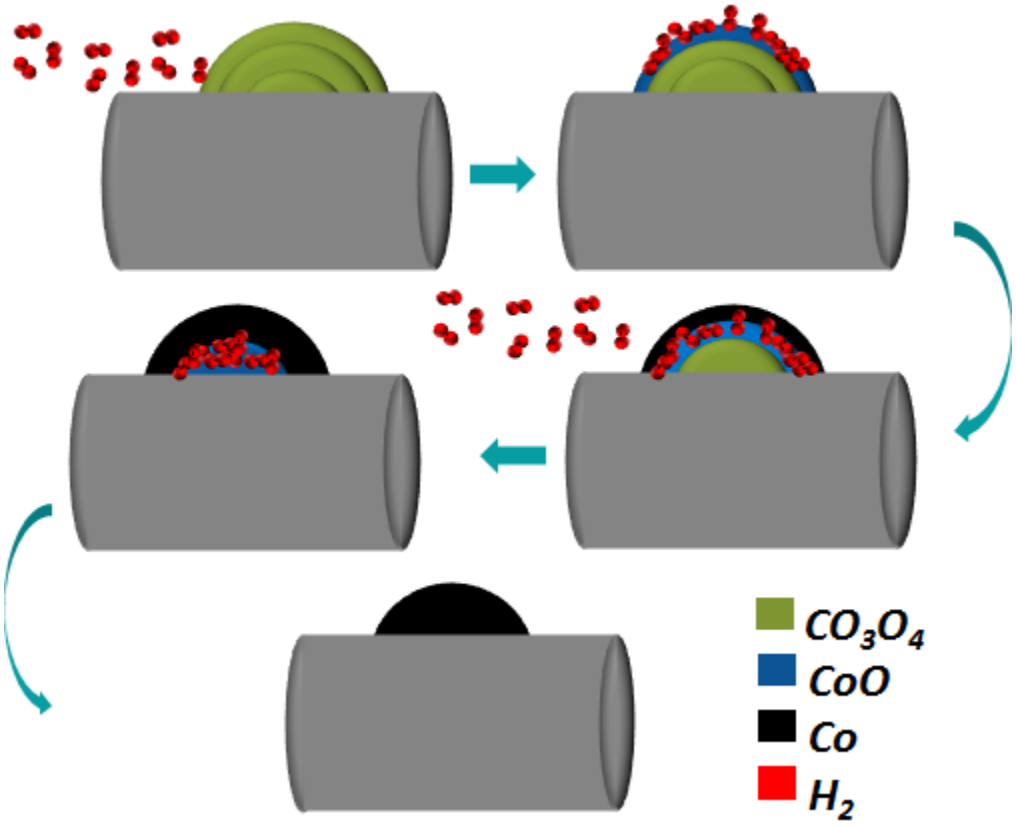

Figure 5.14 Schematic illustration of reduction mechanism for Co/NS catalysts.

5.4 Conclusions

A silica NS supported cobalt FT catalyst was successfully prepared. Its physico-chemical properties were investigated and the catalytic performance evaluated in comparison with a conventional silica sol-gel supported cobalt catalyst. Co/NS had good FT activity and selectivity to C_{5+} hydrocarbons without being fully reduced during the activation period. The results are attributed to greater gases accessibility to the entire surface of the catalyst. Its reduction behavior from cobalt oxide to metallic Co was described using *in situ* XPS, where it was verified that at 385 ºC and 10^{-6} Torr of H_2, the reduction saturates at the rate of 41.4 %

after ~20 hours. The two reduction steps from Co_3O_4 to CoO and to metallic Co are concurrent judging by the coexistence of the three cobalt species during reduction. The heat loss by convection and radiation along the NS, coupled with the small pore volume makes the reduction of small cobalt oxide nanoparticles harder, due to the difficulty of water molecules to diffuse out. Co/NS was completely reduced at 680 ºC and 10 Torr of H_2 after 10 hours as demonstrated by the Co 2p core level and the d-band of Co in the XPS valence band. Continued research will focus on catalyst preparation and reduction to improve the catalytic performance.

References

(1) BP. *BP Statistical Review of World Energy June 2013 bp.com/statisticalreview*. 48 (2013). at <bp.com/statisticalreview>

(2) De la Osa, A. R. *et al*. Performing the best composition of supported Co/SiC catalyst for selective FTS diesel production. *Fuel* **95,** 587–598 (2012).

(3) wikipedia.org/wiki/Fisher-Tropsch_process. Fischer–Tropsch process. *Wikipedia* (2014). at <wikipedia.org/wiki/Fisher-Tropsch_process>

(4) *Thermochemical processing of biomass: conversion into fuels, chemicals and power*. (John Wiley & Sons, 2011).

(5) Tang, H., Liew, K. & Li, J. Cobalt catalysts supported on silica nanotubes for Fischer-Tropsch synthesis. *Sci. China Chem.* **55,** 145–150 (2012).

(6) Wang, Z., Yan, Z., Liu, C. & Goodman, D. W. Surface Science Studies on Cobalt Fischer-Tropsch Catalysts. *ChemCatChem* **3,** 551–559 (2011).

(7) De la Osa, A. R., De Lucas, A., Romero, A., Valverde, J. L. & Sánchez, P. Influence of the catalytic support on the industrial Fischer–Tropsch synthetic diesel production. *Catal. Today* **176,** 298–302 (2011).

(8) Luo, G., Fouetio Kengne, B.-A., McIlroy, D. N. & McDonald, A. G. A novel nano fischer-tropsch catalyst for the production of hydrocarbons. *Environ. Prog. Sustain. Energy* n/a–n/a (2013). doi:10.1002/ep.11916

(9) Reuel, R. Effects of support and dispersion on the CO hydrogenation activity/selectivity properties of cobalt. *J. Catal.* **85,** 78–88 (1984).

(10) Pan, L., Xu, M. & Zhang, Z. D. Synthesis and Electrocatalytic Properties of Co3O4 Nanocrystallites with Various Morphologies. *J. Clust. Sci.* **21,** 655–667 (2010).

(11) Khodakov, A. Y., Bechara, R. & Griboval-Constant, A. Fischer–Tropsch synthesis over silica supported cobalt catalysts: mesoporous structure versus cobalt surface density. *Appl. Catal. Gen.* **254,** 273–288 (2003).

(12) Ho, S. W., Houalla, M. & Hercules, D. M. Effect of particle size on carbon monoxide hydrogenation activity of silica supported cobalt catalysts. *J. Phys. Chem.* **94,** 6396–6399 (1990).

(13) Tavasoli, A. *et al.* Cobalt supported on carbon nanotubes — A promising novel Fischer–Tropsch synthesis catalyst. *Fuel Process. Technol.* **89,** 491–498 (2008).

(14) Lapszewicz, J. A., Loeh, H. J. & Chipperfield, J. R. The effect of catalyst porosity on methane selectivity in the Fischer?Tropsch reaction. *J. Chem. Soc. Chem. Commun.* 913 (1993). doi:10.1039/c39930000913

(15) Tavasoli, A., Abbaslou, R. M. M., Trepanier, M. & Dalai, A. K. Fischer–Tropsch synthesis over cobalt catalyst supported on carbon nanotubes in a slurry reactor. *Appl. Catal. Gen.* **345,** 134–142 (2008).

(16) Ernst, B., Bensaddik, A., Hilaire, L., Chaumette, P. & Kiennemann, A. Study on a cobalt silica catalyst during reduction and Fischer–Tropsch reaction: In situ EXAFS compared to XPS and XRD. *Catal. Today* **39,** 329–341 (1998).

(17) Yeh, J. J. & Lindau, I. Atomic subshell photoionization cross sections and asymmetry parameters: $1 \leqslant Z \leqslant 103$. *At. Data Nucl. Data Tables* **32,** 1–155 (1985).

(18) Powel, C. J. & Jablonski, A. *NIST Electron Inelastic-Mean -Free-Path Datbase, Version 1.2, SRD71*. (National Institute of Standards and Tectnology, 2010).

(19) Çengel, Y. A. *Introduction to thermodynamics and heat transfer*. (McGraw-Hill, 2008).

(20) *Fundamentals of heat and mass transfer*. (John Wiley, 2007).

(21) McWilliams, M. L. & Nichols, D. G. Heat Transfer in a Rod with Convective and Radiadive Losses. *W. Va. Acad. Sci.* 128–134 (1974).

(22) Girardon, J. *et al.* Effect of cobalt precursor and pretreatment conditions on the structure and catalytic performance of cobalt silica-supported Fischer?Tropsch catalysts. *J. Catal.* **230,** 339–352 (2005).

(23) Ling, C. K., Mohd. Zabi, N. A. & Mohan, C. Synthesis and Characterization of Silica-Supported Cobalt Nanocatalysts Using Strong Electrostatic Adsorption. *J. Appl. Sci.* **11,** 1436–1440 (2011).

CHAPTER 6
Summary

6.1 Conclusions

The work reported herein consists of the synthesis, the surface analysis of hybrid type nanostructures and their application in the detection of explosives material and the production of fuels. Silica nanosprings which are insulating in nature, have been grown and their surface chemistry has been modified for each application. For gaseous analyte sensing, nanosprings were post-coated with ZnO and subsequently decorated with metals nanoparticles. The response of ZnO nanospring-based chemiresistors to vapors of toluene, a degradation product of the powerful explosive trinitrotoluene (TNT), was ZnO grain size dependent. The response was poor below 3 nm and above 20 nm grain size, and optimal for 15 nm grain size with a change in the conductance by a factor of 1000. In order to improve the sensitivity, ZnO nanosprings were decorated with differing metal nanoparticles: Au, Ag, Ni, Pt, and Pd. The highest response was achieved with Pd nanoparticles decoration, changing the conductance by a factor of 1500, which is a 50 % enhancement. For selective sensing, Au decorated ZnO nanosprings have been functionalized with thiols of L-cysteine, 4-mercaptohexanol, 4-mercaptobenzoic acid, DL-thioctic acid, and 11-(1-pyrenyl)-1-undecathiol, chosen for their propensity to interact with vaporized explosives. XPS and UPS have been used to characterize the adsorption and the thermal stability of the thiols onto Au/ZnO nanosprings. The thiols are more thermally stable on Au/ZnO nanosprings than on Au thin films. This enhanced stability is attributed to the attachment of thiols not only to Au nanoparticles, but also to ZnO. The headgroups which are the receptors for explosive analytes are located at the top of the surface of the monolayers. The thiols modified sensors

were highly selective to vapor of ammonium nitrate, a signature of explosives. The sensor functionalized with 4-mercaptohexanol showed the strongest response. The packing density and/or ordering of the thiols appeared to play a pivotal role in their responsiveness to gaseous analytes.

For catalytic applications, cobalt nanoparticles supported on silica nanosprings have been prepared. Their physico-chemical properties and their catalytic performances in Fisher-Tropsch synthesis have been investigated and the results compared with those of a conventional silica sol-gel supported cobalt. Even though Co/NS was not fully reduced during the activation period and had 75 times less gravimetric cobalt content than the conventional catalyst, it still showed higher FTS activity and selectivity to C_{5+} hydrocarbons. To further understand the reduction behavior of Co/NS, its reduction state has been investigated using *in situ* XPS. At the surface, the reduction pathway from Co_3O_4 to CoO and from CoO to Co was verified, which concurs with H_2-TPR analyses. The complete reduction of Co/NS at 680 ºC and 10 Torr of H_2 proved the absence of cobalt silicates that result from strong metal-support interaction. The shrinking of the cobalt nanoparticles size during reduction was also an indication of the absence of sintering of nanoparticles. The good FTS catalytic performance of Co/NS is attributed to higher accessibility of the gases to the Co on nanosprings resulting from their unique helical structure. The higher activation temperature relative to the sol-gel catalyst was ascribed to convective and radiative heat losses along the nanosprings. The nature and the structure of a catalyst support can therefore significantly influence the extent of reduction. For an efficient FT catalyst, precise control over the properties including morphology of the support, pores size, surface area, and metal nanoparticles size must be considered.

Overall, surface chemistry is crucial to understand how functionalized nanosprings impact analyte detection and catalytic hydrocarbons production. XPS and UPS have been demonstrated as powerful tools to identify the most critical variables in relation to nanospring-based sensor response and catalyst behavior.

6.2 Future Directions

The analysis and interpretation of the results of these studies showcase nanosprings as suitable building-blocks for sensors and catalyst supports. The methods and the results can be applied to future works towards facilitating the integration of nanospring-based sensors in electronic noses for detection of explosives, but a process should be developed to apply a specific coating or functionalization to a specific sensor in an array of integrated sensors. For the production of drop-in fuels via FTS, lowering the activation temperature of Co/NS can be investigated by studying the effect of the particle size, since there is no much control over the pore size. Catalytic performances of core-shell Fe-Co supported on nanosprings could also be evaluated.

Appendix A

Electron Flood Gun Parameters during Irradiation and Thermal Stability of Thiols on Au/ZnO Nanosprings

Electron Flood Gun Parameters during Irradiation of the Samples

All the samples were exposed to an electron flood gun to avoid spurious charging during XPS measurements. The energy of the electron beam and the focus were 153 eV and 83 V, respectively. The following table summarizes the spot size, the beam current density, and the total fluence during irradiation.

Table 1: Electron gun current density and fluence

Sample treated with	Emission Current (μA)	Target Current (μA)	Spot Diameter (mm)	Beam Current Density (μA/mm^2)	Fluence (eV/ mm^2)
Untreated	30	14.55	11.07	0.151	1.59
4-mercaptobenzoic acid	20	9.70	10.35	0.115	1.82
DL-thioctic acid	20	9.70	10.35	0.115	1.82
6-mercaptohexanol	100	52.47	16.02	0.256	0.759
11-(1-pyrenyl)-1-undecathiol	120	65.34	17.67	0.266	0.624
L-cysteine	140	76.23	18.95	0.270	0.543

For each treated sample the S 2p core level states were recorded after the survey scan, C 1s, Zn 3p – Au 4f, and Zn 2p for a total duration of 103 minutes. With this extended exposure of the samples to the flood gun, S 2p core levels would have exhibited prominent spectral features on the side of higher binding energy, had dissociation or damage occurred.

Thermal Stability of Thiols on Au/ZnO Nanosprings

XPS spectra (indexed 25ºC in the figures) of the as-prepared samples were recorded prior to the thermal stability evaluation. For each thermal treatment the samples were transferred from the ultra-high vacuum (UHV) chamber to the load-lock where they were heated to the desired temperature and maintained for 10 min. They were allowed to cool to room temperature, and then moved back in the UHV for XPS. Temperatures used ranged from 50 to 200ºC with 50ºC increments. Figures 1(a), (b), and (c) show the C 1s, S 2p, and N 1s of the L-cysteine treated sample, respectively.

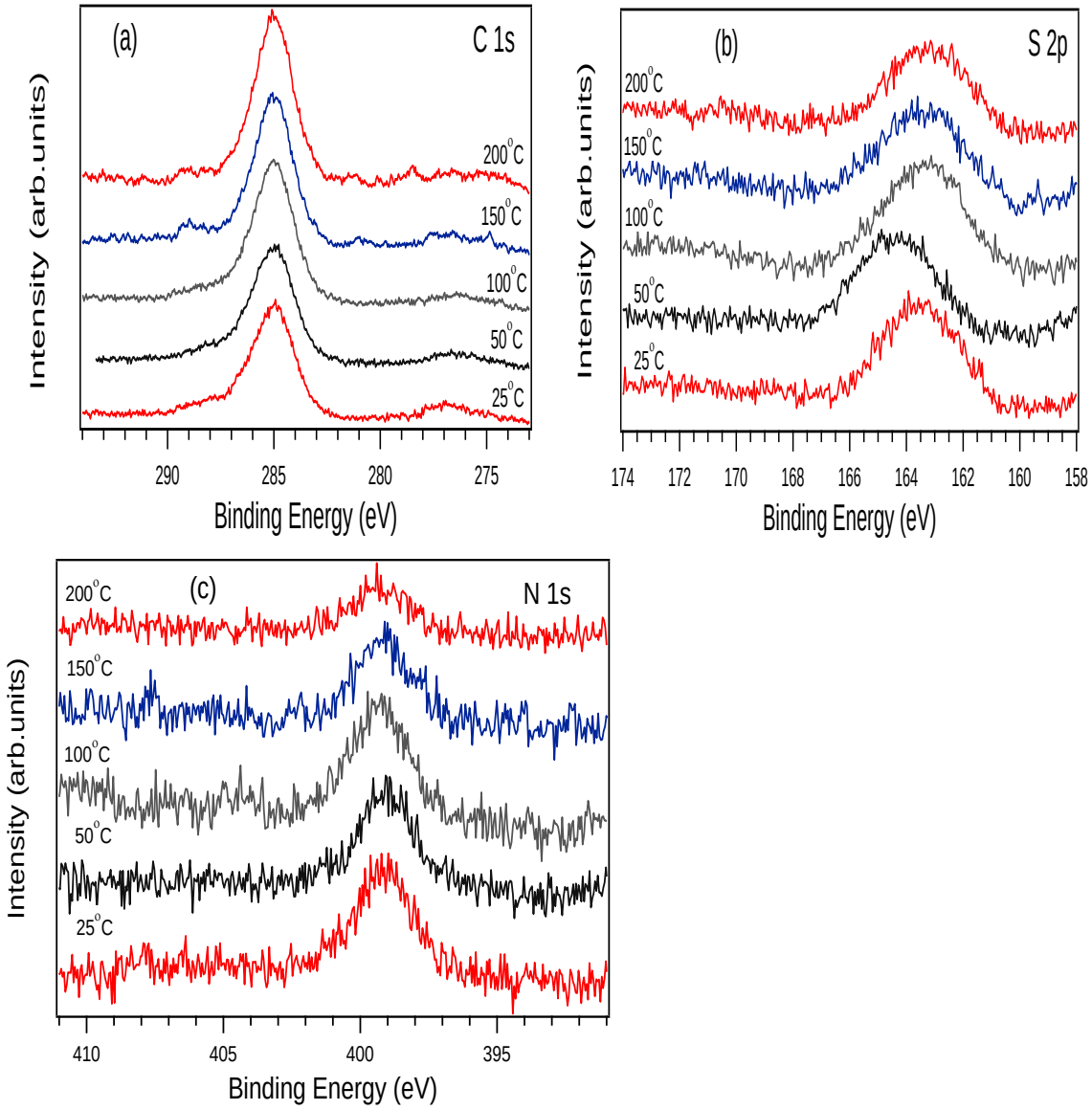

Figure 1 (a) C 1s, (b) S 2p, and (c) N 1s core level states of L-cysteine treated Au/ZnO nanosprings at room temperature and after annealing.

The C 1s core level of the carboxylic group –COOH remains intact up to 200ºC. The S 2p shifts to higher binding energy when the sample is first heated to 50ºC, but shifts back to the original position with the subsequent treatments, which is attributed to thermal induced ordering. The peaks intensities are fairly constant, except for the N 1s core level where a

decrease of the peak intensity is observed. This suggests a gradual desorption of the amine group. Overall, the results indicate the high degree of thermal stability of the sulfur-substrate bonding within the temperature range under consideration. Consequently, 150ºC operational temperature for L-cysteine treated sensor was still below the desorption point.

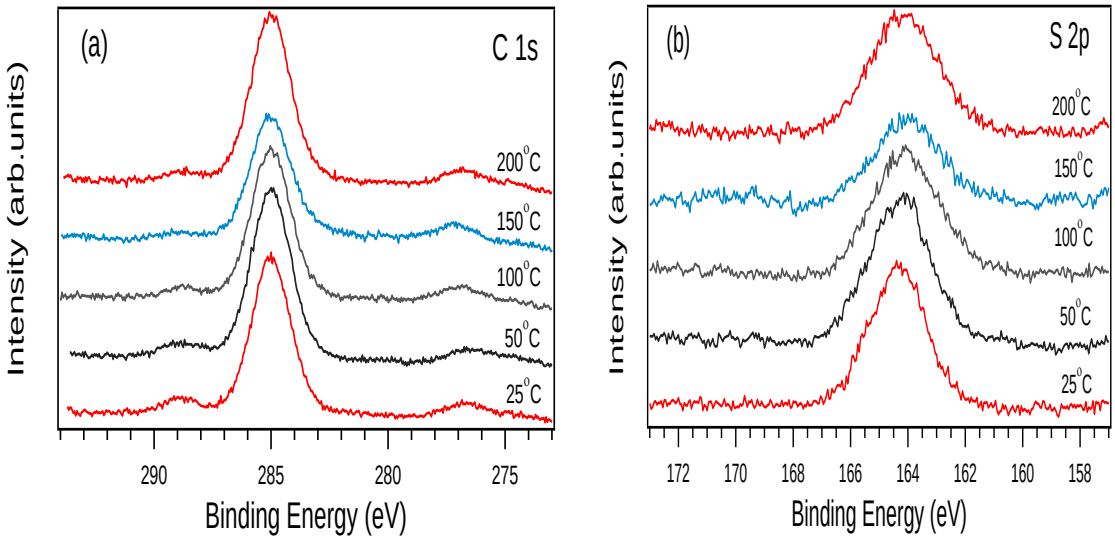

Figure 2 (a) C 1s and (b) S 2p core level states of DL-thioctic acid treated Au/ZnO nanosprings at room temperature and after annealing.

As expected DL-thioctic acid is more thermally stable because of the two sulfurs bonded to the au nanoparticles and/or the ZnO surface. A slight loss of intensity is observed at 150ºC. The DL-thioctic acid treated sensor was operated at 100ºC, far below the degradation temperature of the molecules based on this analysis.

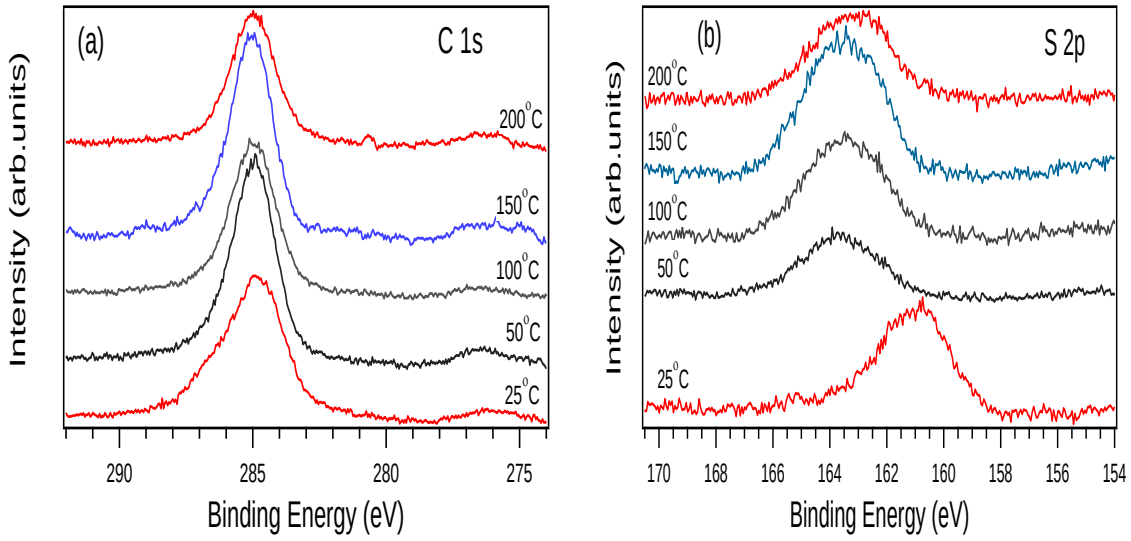

Figure 3 (a) C 1s and (b) S 2p core level states of 6-mercaptohexanol treated Au/ZnO nanosprings heat treated at different temperatures.

For the 6-mercaptohexanol treated sample (Fig.3), the S 2p peak shifted to higher binding energy and lined up the value of the two other samples when heated to 50ºC. This is probably due to desorption of oxygen species and reordering of the film because the shift is initially accompanied by a loss of intensity, and after the peak intensity increases for the subsequent two thermal cycles. The degradation is likely triggered at 200ºC, resulting in the observed decrease. The sensor was tested at the temperature of 150ºC, which is the optimal stable temperature for this molecule.

These findings reveal an enhanced thermal stability of thiols on Au/ZnO relative to thiols adsorbed on Au alone. Chandekar et al.[1] demonstrated, using XPS, progressive loss of sulfur in an octadecanethiol monolayer on gold between 110-145ºC, and a stable 16-mercaptohexadecanoic acid to ca. 145ºC. Using thermal desorption, Noh et al.[2] also found

desorption peaks at about 227ºC for benzenethiol and 127ºC for benzenemethanethiol monolayers on gold.

References

(1) Chandekar A, Sengupta SK, Whitten JE. Thermal stability of thiol and silane monolayers: A comparative study. Appl Surf Sci. 2010 Feb;256(9):2742–9.

(2) Noh J, Ito E, Hara M. Self-assembled monolayers of benzenethiol and benzenemethanethiol on Au(111): Influence of an alkyl spacer on the structure and thermal desorption behavior. J Colloid Interface Sci. 2010 Feb;342(2):513–7.

Appendix B

Synthesis of 11-(1-pyrenyl)-1-undecathiol Scheme and Corresponding NMR Spectra

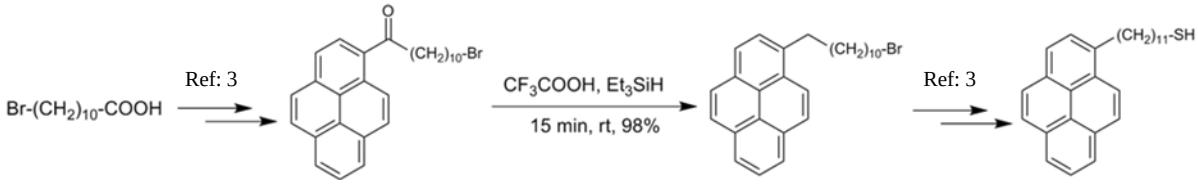

[1] **[2]** **[3]** **[4]**

Scheme S1: Synthesis of 11-(1-pyrenyl)-1-undecathiol [**4**, **PD**].

11-(1-pyrenyl)-1-undecathiol [**4**] was obtained as previously described[3] except for a modification in the conversion of intermediate [**2**] into [**3**] (Scheme **S1**). We found that replacing carbontetrachloride as the solvent with neat trifluoroacetic acid shortened the reaction time from 5 days to 15 min with a slight improvement in yield (from 91% to 98%).

Preparation compound [**3**]: Triethylsilane (0.31 mL, 1.9 mmol) was added drop-wise over 15 min to a room-temperature solution of intermediate [**2**] (295 mg, 0.64 mmol) in neat trifluoroacetic acid (0.47 mL, 6.40 mmol). The reaction mixture was diluted with ether (50 mL) and sequentially washed with saturated aqueous sodium bicarbonate (2 x 25 mL) and water (2 x 25 mL). The organic phase was evaporated to dryness, and the resulting crude was purified via silica gel column chromatography (particle size 0.040-0.063 mm, 100% petroleum ether, distillation range 60-80 °C) to obtain [**3**] [280 mg, 98% yield] as a white crystalline solid. R_f: 0.7 (1% EtOAc in petroleum ether, v/v); ^{1}H NMR (500 MHz, $CDCl_3$) δ 8.26-8.28 (d, 1H, J = 9.0 Hz, Py), 8.12-8.16 (m, 2H, Py), 8.07-8.10 (m, 2H, Py), 7.95-8.03 (m, 3H, Py), 7.84-7.87 (d, 1H, J = 7.7 Hz, Py), 3.37 (m, 2H, CH_2Br), 3.30-3.34 (m, 2H, CH_2Py), 1.79-1.88 (m, 4H, CH_2CH_2Br, CH_2CH_2Py), 1.43-1.50 (m, 2H, CH_2), 1.33-1.41 (m, 4H, 2 x CH_2), 1.25-1.30 (br s, 8H, 4 x CH_2); ^{13}C NMR ($CDCl_3$) δ 137.6, 131.7, 131.2, 129.9, 128.9, 127.8 (Py), 127.5 (Py), 127.3 (Py), 126.7 (Py), 126.0 (Py), 125.35, 125.33, 125.0 (Py),

124.8 (2 x Py), 123.8 (Py), 34.2 (CH_2Br), 33.8 (CH_2Py), 33.1 (*CH_2*CH_2Br/*CH_2*CH_2Py), 32.1 (*CH_2*CH_2Br/*CH_2*CH_2Py), 30.0 (CH_2), 29.78 (CH_2), 29.77 (CH_2), 29.7 (CH_2), 29.6 (CH_2), 29.0 (CH_2), 28.4 (CH_2).

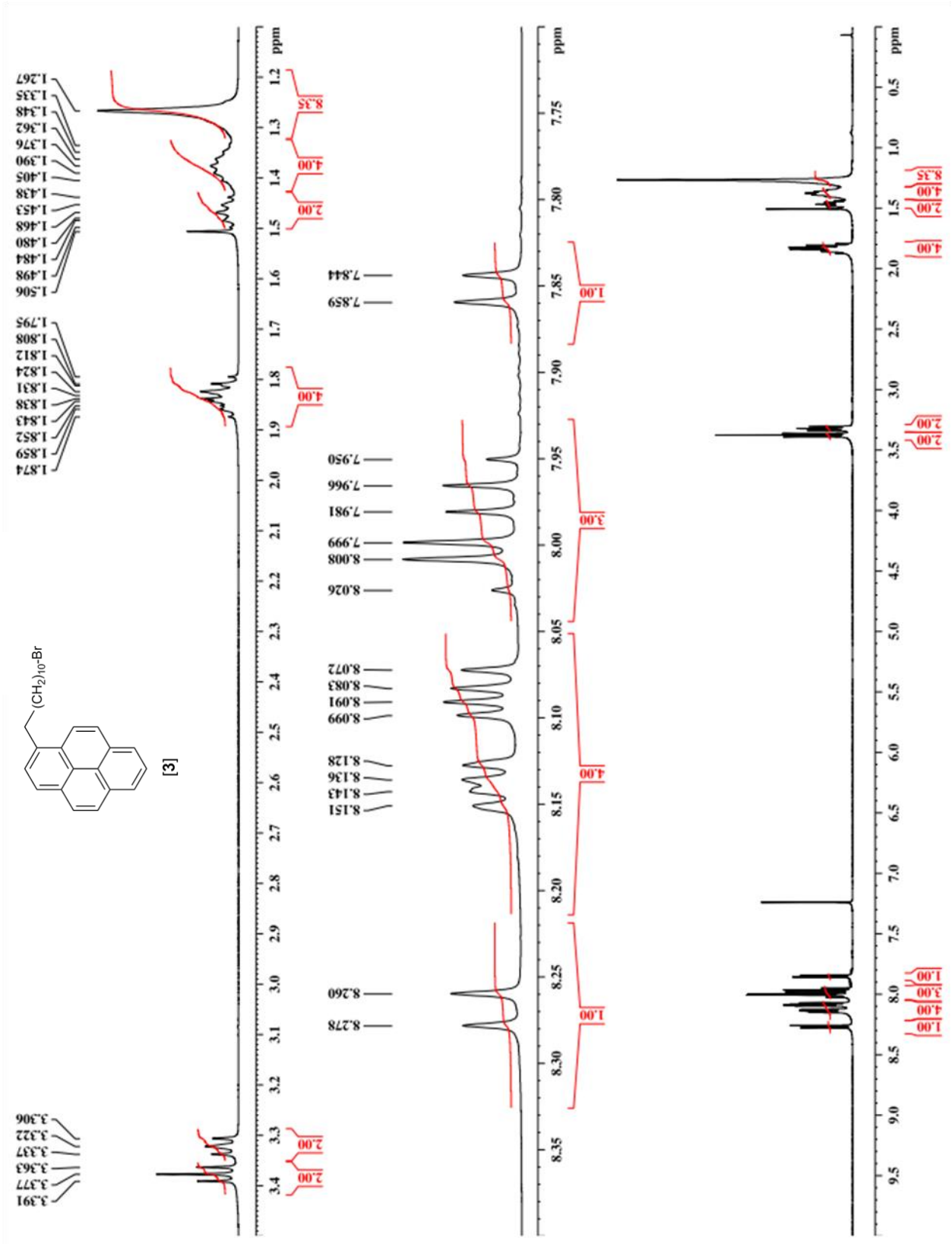
(CH2)10-Br
[3]

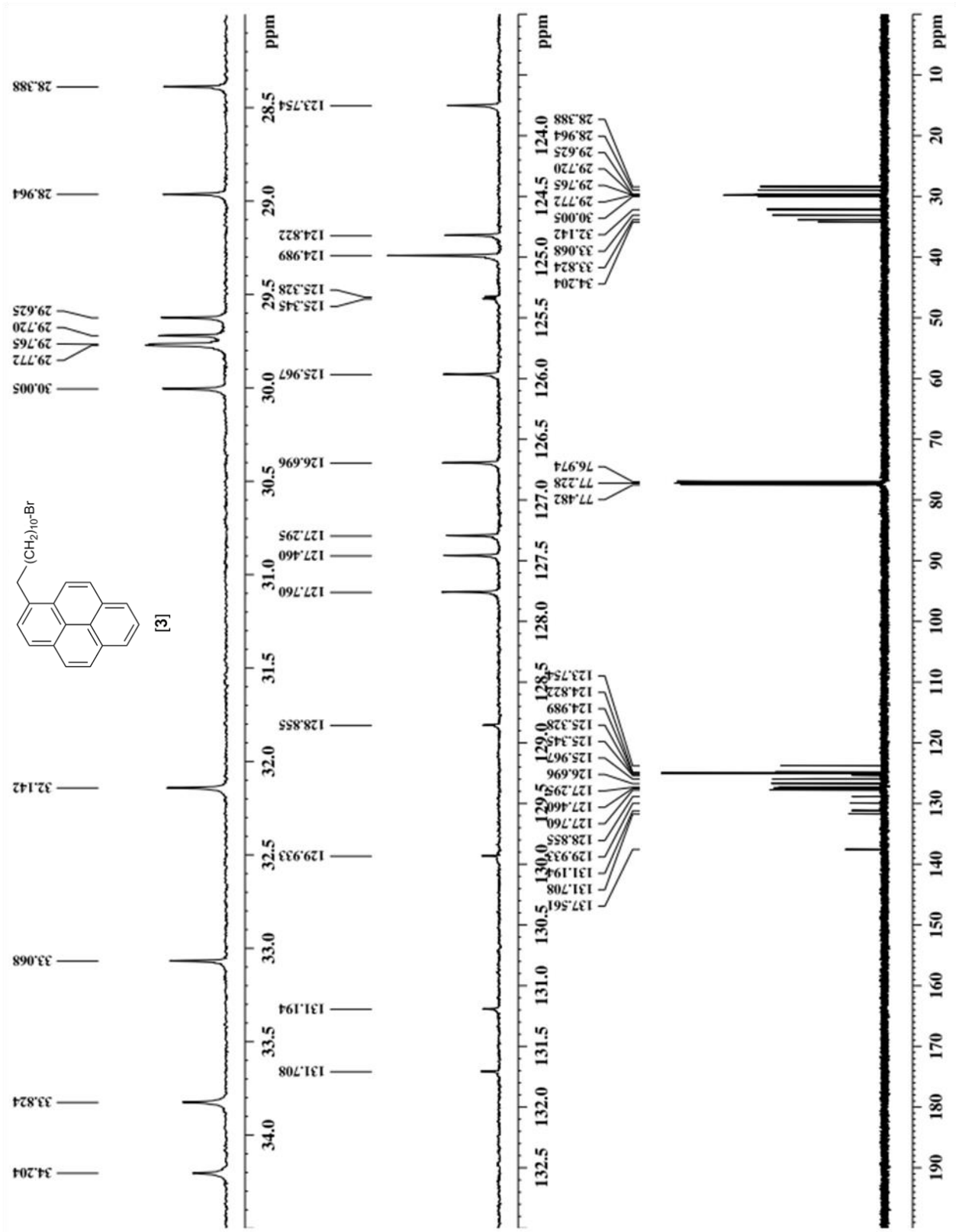
[3]
(CH2)10Br
ppm

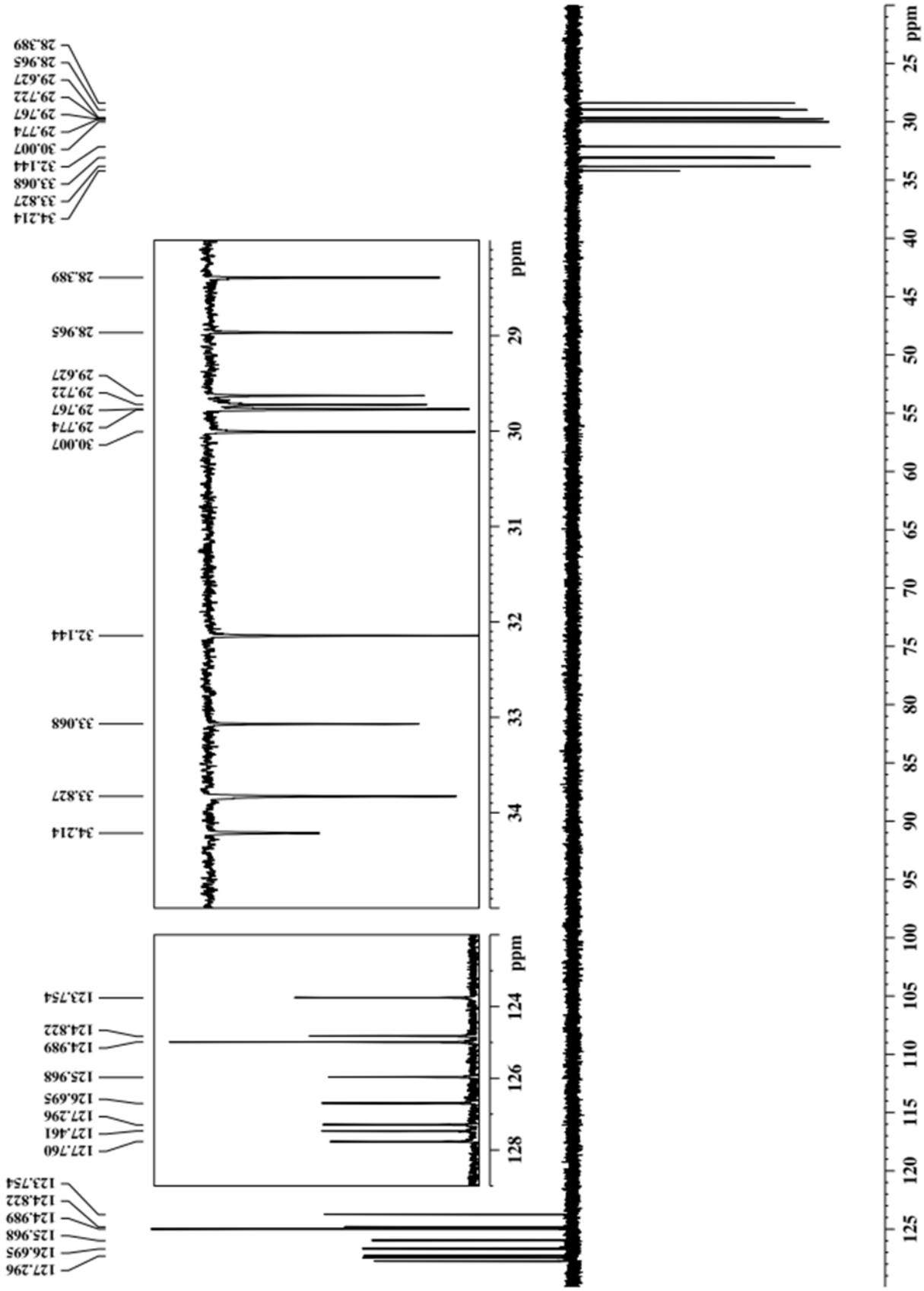
127.296
126.695
125.968
124.989
124.822
123.754
127.760
127.461
127.296
126.695
125.968
124.989
124.822
123.754
34.214
33.827
33.068
32.144
30.007
29.774
29.767
29.722
29.627
28.965
28.389
34.214
33.827
33.068
32.144
30.007
29.774
29.767
29.722
29.627
28.965
28.389
ppm
ppm
ppm

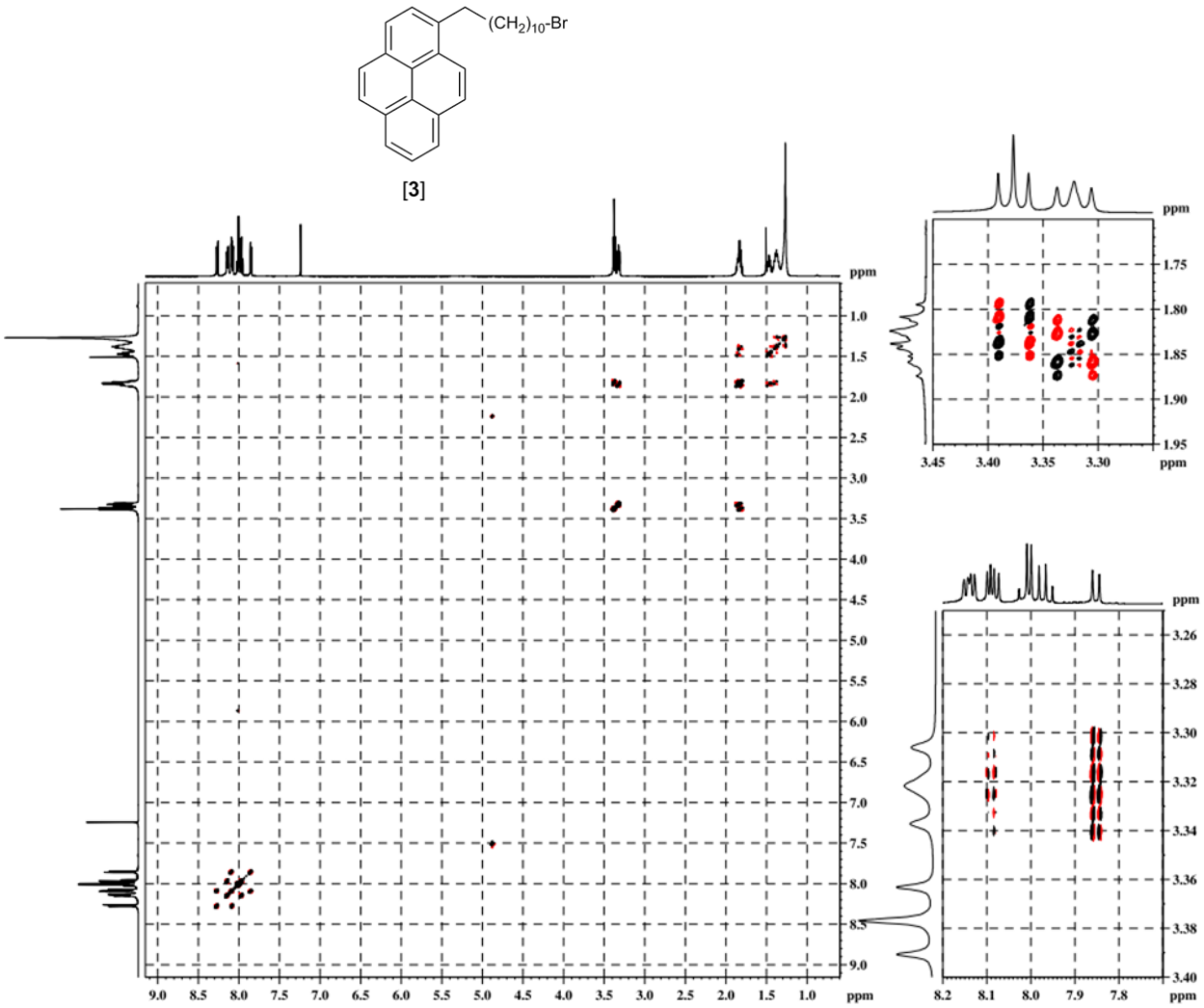
(CH2)10-Br
[3]
ppm
9.0 8.5 8.0 7.5 7.0 6.5 6.0 5.5 5.0 4.5 4.0 3.5 3.0 2.5 2.0 1.5 1.0
1.0 1.5 2.0 2.5 3.0 3.5 4.0 4.5 5.0 5.5 6.0 6.5 7.0 7.5 8.0 8.5 9.0
3.45 3.40 3.35 3.30
1.75 1.80 1.85 1.90 1.95
8.2 8.1 8.0 7.9 7.8
3.26 3.28 3.30 3.32 3.34 3.36 3.38 3.40

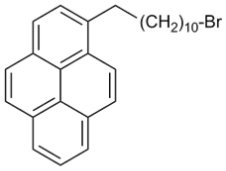
(CH2)10-Br

[3]

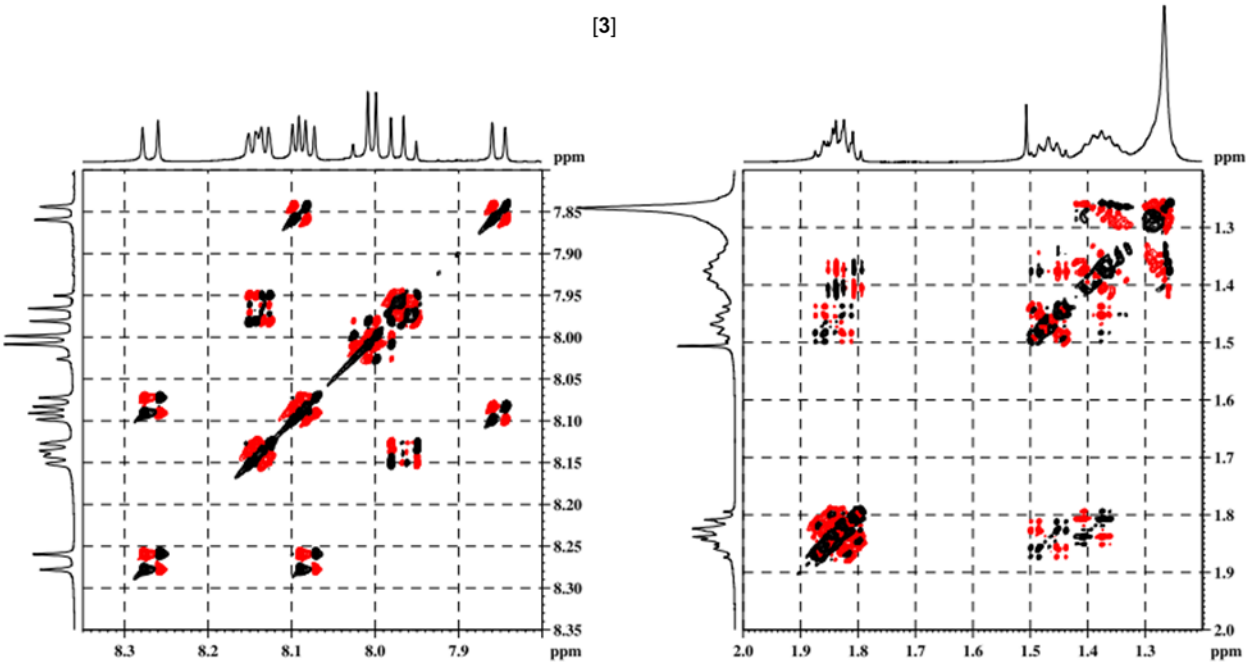
ppm
7.85
7.90
7.95
8.00
8.05
8.10
8.15
8.20
8.25
8.30
8.35
8.3
8.2
8.1
8.0
7.9
ppm
ppm
1.3
1.4
1.5
1.6
1.7
1.8
1.9
2.0
2.0
1.9
1.8
1.7
1.6
1.5
1.4
1.3
ppm

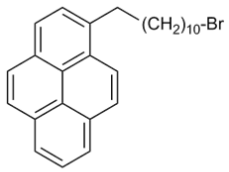
(CH2)10-Br

[**3**]

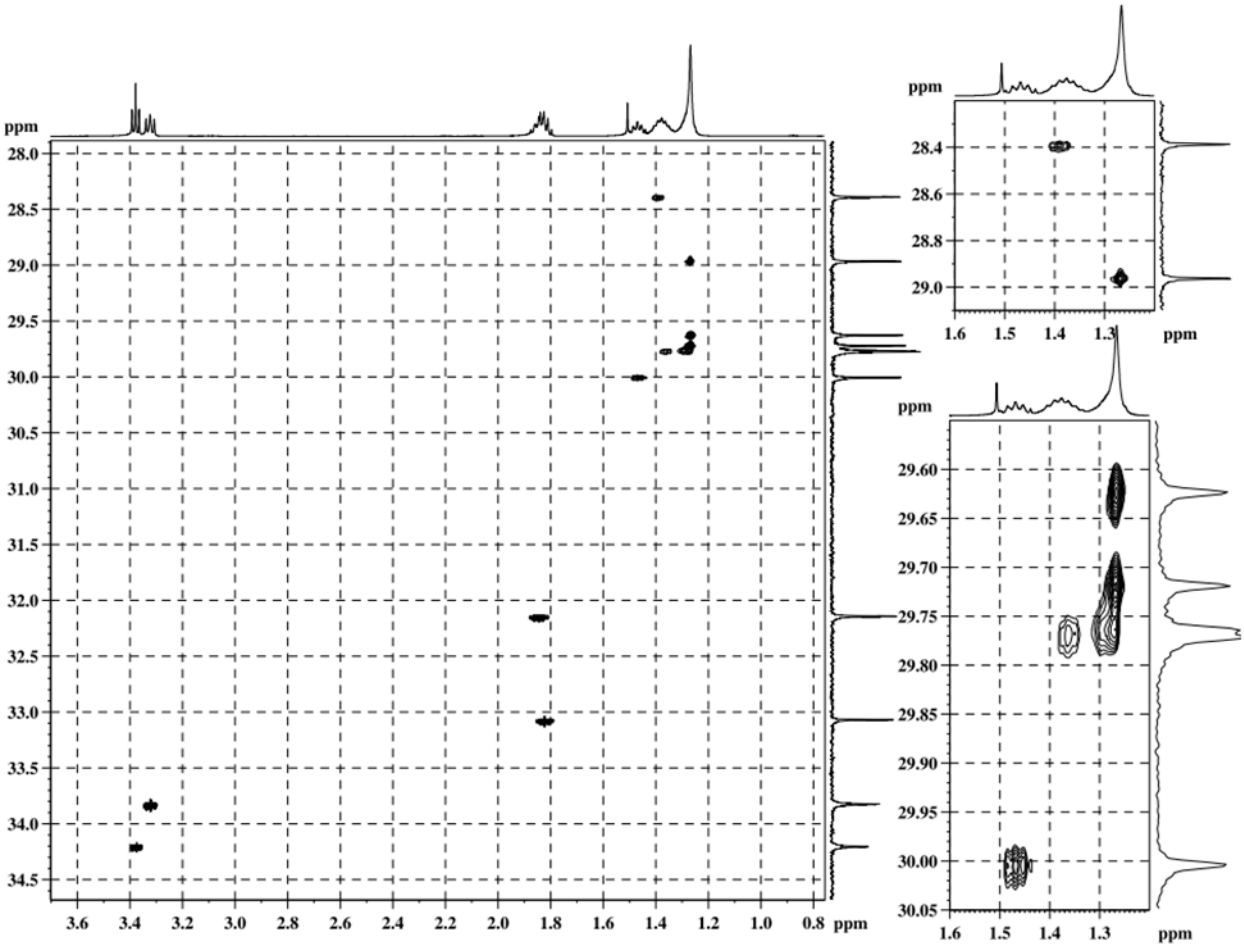
ppm
28.0
28.5
29.0
29.5
30.0
30.5
31.0
31.5
32.0
32.5
33.0
33.5
34.0
34.5
3.6
3.4
3.2
3.0
2.8
2.6
2.4
2.2
2.0
1.8
1.6
1.4
1.2
1.0
0.8
ppm
ppm
28.4
28.6
28.8
29.0
1.6
1.5
1.4
1.3
ppm
ppm
29.60
29.65
29.70
29.75
29.80
29.85
29.90
29.95
30.00
30.05
1.6
1.5
1.4
1.3
ppm

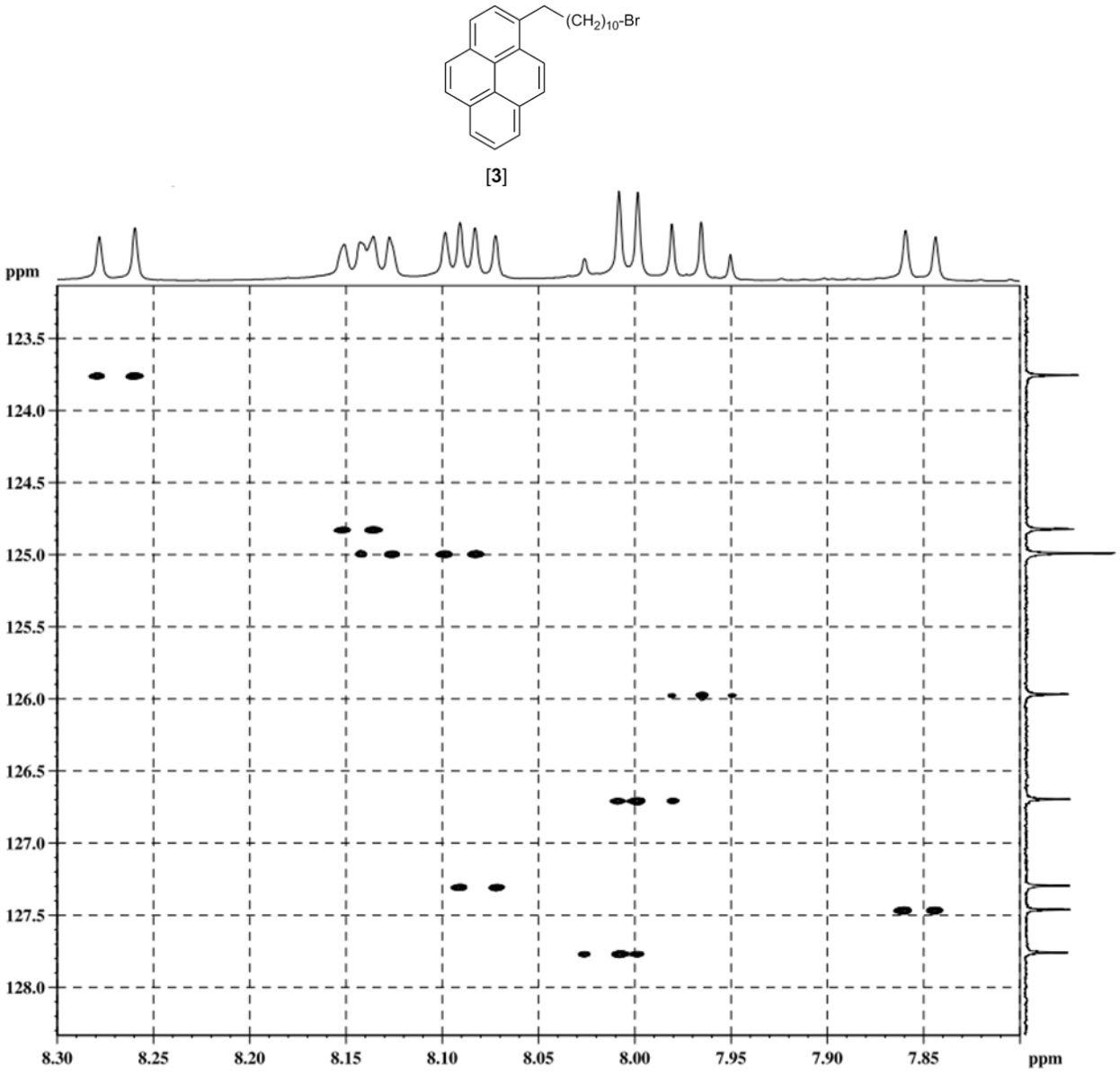

Reference

(1) Nakamura F, Hara M. Hybridization of Polynucleotides Using Self-Assembled Monolayer Containing Pyrenyl Groups. Mol Cryst Liq Cryst Sci Technol Sect Mol Cryst Liq Cryst. 2002;377(1):57–60.